

Magneto-Seebeck tunneling across a vacuum barrier

Dissertation
zur Erlangung des Doktorgrades
an der Fakultät für Mathematik, Informatik und Naturwissenschaften
Fachbereich Physik
der Universität Hamburg

vorgelegt von
M. Sc. Cody Friesen

Hamburg
2019

Gutachter/innen der Dissertation:	Prof. Dr. Roland Wiesendanger Prof. Dr. Michael Thorwart
Zusammensetzung der Prüfungskommission:	Prof. Dr. Wolfgang Hansen Prof. Dr. Alexander Lichtenstein Prof. Dr. Roland Wiesendanger Prof. Dr. Michael Thorwart Dr. Robert Frömter
Vorsitzende/r der Prüfungskommission:	Prof. Dr. Wolfgang Hansen
Datum der Disputation:	June 22nd, 2020
Vorsitzender Fach-Promotionsausschusses PHYSIK:	Prof. Dr. Michael Potthoff
Leiter des Fachbereichs PHYSIK:	Prof. Dr. Wolfgang Hansen
Dekan der Fakultät MIN:	Prof. Dr. Heinrich Graener

Abstract

In this thesis spin-polarized scanning tunneling microscopy, combined with scanning tunneling potentiometry, was used to study magneto-Seebeck tunneling at an atomic scale. For our experiments, we used a homebuilt scanning tunneling microscope, mounted on an eddy-current damping stage inside of an ultra-high vacuum chamber system. Both the tip and the sample were simultaneously cooled using a helium flow cryostat, allowing for equilibrium measurements. A temperature gradient between the tip and sample was then created using an external diode laser with variable power. Numerical modeling was used to determine the temperature gradient from the linear thermal tip expansion. A lock-in amplifier was used to measure the differential conductance, which was used as a feedback signal to maintain the tip-sample separation, and a separate DC bias feedback loop compensated for any DC tunneling current, thus measuring the potential across the tunneling junction.

This potentiometry measurement was used to predict the values of the Seebeck coefficient S . The predictions were supported by means of $I(V)$ spectroscopy. If the probe tip is heated with the laser, the resulting thermal voltage can be measured directly. The corresponding (magneto-)Seebeck coefficients were thus determined on different magnetic surfaces with spin-averaged and spin-resolving tips.

The measured S values exhibited a dependence on the relative magnetization of the measurement tip and the sample. With a periodicity of 1 nm, this effect was also measured in a nanoskymion lattice of a Fe single layer on Ir (111) to emphasize the achievable resolution of the experimental method.

Zusammenfassung

In dieser Arbeit wurde spinpolarisierte Rastertunnelmikroskopie in Kombination mit Rastertunnelpotentiometrie verwendet, um den Magneto-Seebeck-Tunneleffekt auf atomarer Skala zu untersuchen. Die Experimente wurden mit einem Rastertunnelmikroskop durchgeführt, welches sich auf einem wirbelstrombasierten Dämpfungstisch in einem Ultra-Hochvakuum-System befindet. Die Kühlung von Sondenspitze und Probe erfolgte mithilfe eines Helium-Durchfluss-Kryostats, was Messungen im thermischen Gleichgewicht ermöglichte. Für die Erzeugung eines Temperaturunterschieds zwischen Sondenspitze und Probe wurde ein externer Diodenlaser mit variabler Leistung verwendet. Der generierte Temperaturgradient wurde mithilfe numerischer Berechnungen der linearen thermischen Ausdehnung der Messspitze ermittelt. Durch einen Lock-in-Verstärker wurde der differentielle Leitwert bestimmt, welcher als Feedback-Signal für den Abstand zwischen Messspitze und Probe diente. Ein Gleichspannungs-Regelkreis kompensierte Gleichstromanteile im Tunnelstrom und zeichnete so den Spannungsabfall am Tunnelkontakt auf.

Diese Potentiometriemessung wurde verwendet, um die Werte des Seebeck-Koeffizienten S vorherzusagen. Die Vorhersagen wurden durch mittels $I(V)$ -Spektroskopie unterstützt. Wird die Sondenspitze mit dem Laser erwärmt, kann die entstehende Thermospannung direkt gemessen werden. Die entsprechenden (magneto-)Seebeck-Koeffizienten wurden so auf verschiedenen magnetischen Oberflächen mit spin-gemittelten und spin-auflösenden Spitzen bestimmt.

Der gemessene S -Wert zeigte eine Abhängigkeit von der relativen Magnetisierung von Sondenspitze und Probe. Mit einer Periodizität von 1 nm wurde dieser Effekt auch in einem Nanoskymionen-Gitter einer Fe-Einzelschicht auf Ir(111) gemessen, um die hohe Ortsauflösung der experimentellen Methode zu unterstreichen.

Contents

1	Introduction	1
2	Origin of magneto-Seebeck tunneling	7
2.1	Definition of tunnel junctions	7
2.2	Thermally induced (Seebeck) tunneling	10
2.3	Magnetic tunnel junctions	14
2.4	Magneto-Seebeck tunneling	16
2.5	Spin-polarized scanning tunneling microscopy	17
3	Experimental implementation	21
3.1	Creating a magnetic tunnel junction	21
3.1.1	A variable-temperature scanning tunneling microscope	22
3.1.2	Tunneling tips	29
3.1.3	Sample systems	32
3.2	Thermal system of the STM	44
3.2.1	Description of thermal elements	44
3.2.2	Equilibrium tip temperature modeling	46
3.2.3	Implementation of tip heating via laser	53
3.2.4	Measurement of temperature difference	56
3.3	Tip-sample potential measurement	63
3.3.1	Constant-conductance STM	64
3.3.2	Bias compensation	66
3.4	AC rectification	67
3.5	Bias spectroscopy	71
3.6	Measurement technique for Seebeck tunneling	71
3.7	Summary	72
4	Spin-averaged Seebeck tunneling	75
4.1	Topographic comparison	76
4.2	Compensated current imaging	77
4.2.1	Measurement of average tip-sample potential	80

4.3	Sources of contrast in potential	80
4.4	Bias spectroscopy	82
4.4.1	Effective AC signal and DC offset	82
4.4.2	AC rectification	84
4.5	Predicting Seebeck values	86
4.6	Tip-heating data	86
4.7	Summary	89
5	Spin-dependent Seebeck tunneling	91
5.1	Method comparison	91
5.2	Tip-heating results	93
5.3	Seebeck analysis of magnetic domain walls	94
5.4	Fe layers on Ir(111)	96
5.5	Seebeck sensor for spintronics	98
5.6	Summary	100
6	Conclusion and outlook	101
	Bibliography	105
A	Equilibrium temperature modeling	117
A.1	Heat shield	117
A.1.1	Heat shield - UHV chamber	117
A.1.2	Heat shield - Heat exchanger	118
A.1.3	Heat shield - STM body	118
A.1.4	Heat shield - Tip	119
A.2	Tip	119
A.2.1	Tip - STM body	119
B	Uncompensated tunneling current	121
C	Dependence of compensated bias on tip-sample separation	125
	Publications	127
	Conferences	128
	Acknowledgements	130

Chapter 1

Introduction

In the field of condensed matter physics, a great deal of effort has been spent on discovering the connection between applied potentials, such as thermal gradients or electric potentials, and the resulting transport of energy through the system. Here system can refer to bulk solid-state materials, liquids, layered structures, tunneling junctions, etc. This broad definition encompasses effects such as electrical resistance (transport of electrons and holes as a result of an applied electric potential), thermal resistance (transport of heat via particle and quasi-particle carriers), and magnetic transport (e.g. spin waves).

Within this general topic of transport within materials, thermoelectricity, which is the relationship between heat and electric charge transport in a material, has been studied since the early 1800s. This began with the independent discoveries of the well-known Seebeck and Peltier effects, discovered by Thomas Seebeck in 1823 [1], and Jean Peltier in 1834 [2], respectively, along with the related Thomson effect, attributed to Lord Kelvin in 1854 [3]. These effects are essentially manifestations of the same underlying physics, and as such can be directly related to one another via the Thomson relations [4].

Although these effects are present in the interior of materials, they are in general not directly measurable in the bulk. The application of measurement probes, e.g. voltage probes from a multimeter, will in fact create an interface between the sample material and the probe material, which will determine the magnitude of the measured effect. In fact the study of interfaces between dissimilar materials is of central importance to the understanding of thermoelectricity.

As an example, we take the case of the well-known Seebeck effect, defined as

$$\nabla V_{\text{therm}} = -S(T) \nabla T, \quad (1.1)$$

where the temperature gradient ∇T in a material with Seebeck coefficient S will generate a (anti-)parallel electric voltage gradient, ∇V_{therm} . But to measure this effect, voltage probes would need to be placed at either end of the material. If two materials with differing S are joined at both ends, and the junctions are held at different temperatures, an electromotive force is generated which is dependent on the difference between the average temperature of the junctions and on the difference between the Seebeck coefficients of the materials [5].

Although this effect is quite small in absolute terms, on the scale of mV K^{-1} at room temperature [6], it can nevertheless be used as an indirect measurement of the absolute temperature, when one junction is held at a known reference temperature. This device is known as a thermocouple, and as this is a metallic junction, the operational temperature range of this device can be very broad [7], leading to extensive use in industry and research, in addition to consumer devices.

More recently, an additional degree of freedom, in the form of the magnetization of the material, or for a junction device one or both of the electrodes, has been applied to the study of these systems. This follows the general trend towards quantifying interactions between increasing amounts of potentials. Although the simultaneous interaction of thermal gradients, electrical potentials, and magnetic potentials had been explored theoretically [8], the field gained renewed interest with the discovery of the spin-Seebeck effect, by Uchida and coworkers [9]. This has led to the field of spin-caloritronics, so named in reference to the larger field of spintronics, which is concerned with the use of spin transport in materials, primarily for research and computing applications [10, 11].

Part of this success can be attributed to the increasingly uniform and precise interfaces that can be created. The advent of increasingly detailed techniques for nano-scale fabrication [12], measurement [13], and manipulation, in particular for magnetic thin-films [14], have led to an improved understanding of spin-caloritronic effects, and their potential uses in engineering sensors and devices at all size scales, e.g. waste-heat recycling and switchable thermal conductance at the nanoscale [11, 15, 10]. For example, insulating layers of MgO with thicknesses of only a few nanometers can be routinely created [16].

This is still a broad topic, encompassing such effects as the spin-dependent generalizations of the classic non-magnetic thermoelectric effects, heat transport via collective motion of single spins, and relativistic considerations in

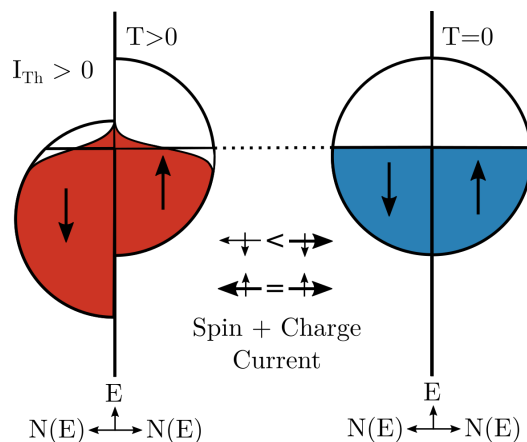


Figure 1.1: Schematic depiction of magneto-Seebeck tunneling between two metallic electrodes, with the density of states $N(E)$ shown partially filled according to a Fermi distribution. For clarity, the right electrode is assumed to be at 0 K, while the left is at a finite positive temperature. In the illustrated case, for the minority spins the symmetry of the occupied and unoccupied states around the Fermi level will lead to no net current, while the asymmetry in the majority spins will yield both a net charge and spin current.

the form of the anomalous and spin Hall effects. Much work is underway to explore these effects, and central to these efforts is the search for robust systems that afford precise control of the relevant potentials, with which to quantify and manipulate these relationships.

In this work, we will focus on the measurement of a single spin-caloritronic effect: The tunneling magneto-Seebeck (TMS) effect. This is a spin-dependent generalization of the tunneling Seebeck effect, which occurs when a thin insulating barrier is placed between conductive electrodes and a temperature gradient is applied across the junction. This effect has been previously measured in a layered device structure, both with non-magnetic and magnetic electrodes [17, 18, 19, 20, 21, 22]. The basis of this effect is illustrated in Figure 1.1.

The tunneling Seebeck effect occurs when a temperature gradient is present across a tunneling junction. In the case of a symmetric density of states (DOS), with respect to the Fermi energy E_f , each thermally occupied state above E_f will be compensated by an unoccupied state below E_f , leading to zero net tunneling current. However, if there exists an asymmetry in the density of states (DOS) at the Fermi level in at least one of the electrodes, the uncompensated thermally-dependent occupation of these states will lead to a temperature dependent charge carrier tunneling. For small temperature

differences this effect is relatively linear, leading to the standard linear form of the Seebeck effect from Equation (1.1).

In the case of a magnetic tunnel junction (MTJ), similar to tunneling magneto-resistance, we can consider a two-channel model, where the differing asymmetry in the parallel and anti-parallel junction states results in a Seebeck coefficient that is dependent on the relative magnetization of the electrodes [23]. In this case both spin-averaged and spin-dependent components of the total S will be present, and the strength of the spin-dependent Seebeck tunneling again depends on the magnitude of the asymmetry of the density of states of the electrode surfaces at E_f . Thus it is crucially dependent on the electrode surface structure and nature of the tunneling barrier. This provides a window into the Fermi-level physics of surfaces, which is of basic physical interest.

It has been found that the magnitude of the switching effect can be comparable to that of the spin-averaged case. This can be characterized by the magneto-Seebeck ratio TMS, defined in the literature as [22]

$$\text{TMS} = \frac{S_P - S_{AP}}{\min(S_P, S_{AP})}, \quad (1.2)$$

where $S_{P/AP}$ are the Seebeck coefficients for parallel and anti-parallel alignments of the magnetization. Experimental values of a few hundred percent have been reported [24], which makes it interesting for technological applications. The addition of magnetic switching means that the flow of this thermoelectricity could be controlled with an external magnetic field, leading to the possibility of reliable, efficient, and controllable heat valves at nanometer scales [25].

Thus, from an applied perspective, magneto-Seebeck tunneling could be used to manage heat dissipation in electronic or spintronic devices, or to directly use heat flow as a computing element [26]. Temperature gradients of even a few degrees Kelvin, for example between transistor elements in a computer processor and the bulk substrate [27], can lead to thermovoltages on the microvolt or millivolt scale. This potential could be used to drive a thermoelectric current to power other computing elements, especially energy-efficient spintronic devices, or aid with cooling [28]. Magnetic sensor elements could also be powered by this thermovoltage.

A measurement of magneto-Seebeck tunneling requires simultaneous knowledge of the junction magnetization, electrical potential, and the absolute temperature of both electrodes. The magnetization and equilibrium bulk temperature of each electrode can be fixed externally, and the electric potential can, with proper shielding, be directly measured. However, estimating the temperature gradient in nano-scale tunneling junctions has proven to be

more difficult [29, 17]. Although an insulating barrier will in general have a correspondingly low thermal conductance, any heat conduction will decrease the actual temperature gradient achieved, leading to lowered values for S .

To date, experimental studies of the TMS effect have been performed using insulating tunneling barriers, formed by oxide layers between metal electrodes [17, 30, 22]. These purely solid-state devices have the advantage of reliable operation at room-temperatures and above, critical for industrial environments, and have also been used to study controlled switching of the junction [17]. However, these studies have relied on temperature estimates from numerical modeling, assuming known heat inputs and material properties. Direct measurement of the temperature gradient has been difficult to achieve without influencing the MTJ. Without a reference measurement then, despite an accurate voltage measurement, the uncertainty in the measured tunneling Seebeck value for these devices remains high. In addition, while the overall chemical composition of the electrode materials can be controlled, there is still variation in the quality of the fabricated MTJs, and since the measurements are necessarily an averaged value over the face of the junction, this prevents experimental attribution of thermoelectric properties to specific surface features.

To address these issues of barrier reproducibility and thermal isolation, we have measured the magneto-Seebeck effect using scanning tunneling microscopy (STM). The basic approach of STM has been adapted to study a wide variety of effects, including spin-averaged thermopower [31, 32, 33, 34, 19]. However, an application of this thermopower technique to magnetic tunnel junctions has so far been lacking.

For measuring magneto-Seebeck tunneling, the basic approach of measuring the electric potential between two electrodes (here the STM tip and sample with a vacuum tunneling barrier) while varying the temperature differential applies. Therefore for our measurements we combined the techniques of spin-polarized STM [35] and scanning tunneling potentiometry [36], enabling laterally resolved imaging of the magnetization-dependent tip-sample potential. This approach is depicted schematically in Figure 1.2.

The measurements were performed by applying an actively controlled compensating voltage, V_{comp} , across the tip-sample tunneling junction, such that no constant current across the junction is measured. The requisite temperature gradient was obtained via external laser heating of the STM tip, and the required bias to compensate for the generated thermovoltage becomes a direct measurement of the Seebeck tunneling ($V_{\text{th}} = -V_{\text{comp}}$). This definition of the thermopower as the required compensating voltage is standard in layered device measurements [29, 22]. This also has the benefit of preventing any resistive heating or current-induced magnetic effects, which

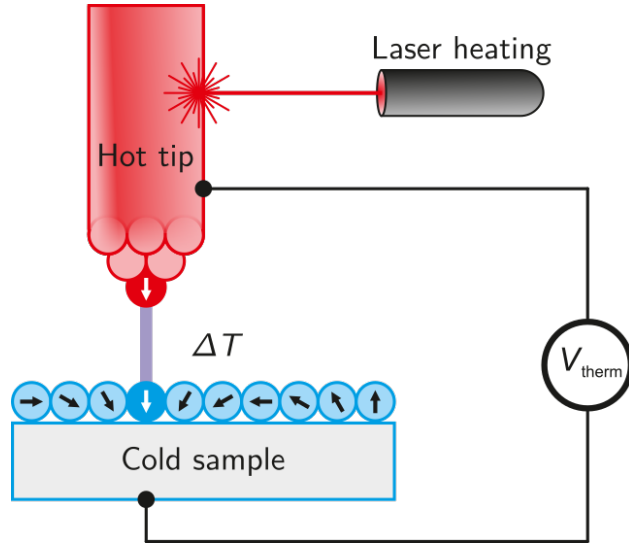


Figure 1.2: Illustration of experimental approach. The magnetic STM tip is heated via laser, creating a temperature difference $\Delta T = T_{\text{tip}} - T_{\text{sample}}$ between tip and sample and the generated thermovoltage V_{therm} is measured. Magneto-Seebeck tunneling will be detectable as a modulation of V_{therm} as a function of the relative magnetization of tip and sample.

can become significant in nanoscale structures [37].

Outline of thesis

In this thesis, we will present our work in measuring (magneto-) Seebeck tunneling using STM, in UHV and cryogenic conditions. In Chapter 2, the theoretical underpinnings of tunneling junctions, and their expected behaviour in response to static and time dependent electric potentials, as well as thermal gradients, will be discussed, and the relationship between generic tunneling junctions and STM will be outlined. Following this, Chapter 3 will detail the experimental setup used to measure the effect, and the procedures followed to collect the data. This will include a description of the sample systems and STM tips used in the experiments, and details of determining the temperature of the tunneling junction. Having established our approach, Chapter 4 and Chapter 5 will present our findings for Seebeck tunneling in non-magnetic and spin-polarized tunnel junctions respectively. Finally, a summary of the work and an outlook for future experiments will be found in Chapter 6.

Chapter 2

Origin of magneto-Seebeck tunneling

In this Chapter, the theoretical basis necessary to formulate an experimental and analytical approach to measuring magneto-Seebeck tunneling will be presented. First, the general behaviour of tunnel junctions will be discussed in terms of the Bardeen model of tunneling junctions. This will be used as a basis to discuss non-magnetic tunneling due to thermal gradients (Seebeck tunneling). The concept of tunnel junctions will then be extended to magnetized electrodes and their response to thermal gradients, giving a basis for discussion of magneto-Seebeck tunneling. Finally, the connection between the previous tunneling behaviour, valid for any tunneling junction, and the specific case of spin-polarized scanning tunneling microscopy (SP-STM) will be clarified.

2.1 Definition of tunnel junctions

We define a tunnel junction, for the following discussion, to consist of two electrically conductive reservoirs of charge carriers in equilibrium (electrodes), separated by an electrically insulating barrier that is sufficiently thin to allow for quantum mechanical tunneling. We will consider only elastic tunneling of electrons in this explanation, neglecting inelastic effects unless required. Here elastic refers only to the tunneling process itself, as after tunneling a particle will be thermalized via inelastic interactions. Experimentally, this situation is well approximated by tunneling between two metal electrodes across a vacuum barrier.

Under these constraints, the Bardeen theory of tunneling is sufficient to explain the required features [38]. This approach relies on time-dependent

perturbation theory, considering each electrode to have its own Hamiltonian, with accompanying energy-dependent wavefunctions. The wavefunctions from either side decay exponentially into the barrier, as is commonly established by solving the one-dimensional Schrödinger equation for a rectangular potential. If there is a significant overlap between the basis wavefunctions inside the barrier, over time the amplitude of an electron wavefunction can transfer between the electrodes, giving a finite probability for the electron to tunnel into the other electrode.

This process is described quantitatively by the matrix tunneling element M , which is a function of the overlapping wavefunctions from the reservoirs. This element, for the tunneling of state ψ_μ into state χ_ν , has the general form [38, 39]

$$M_{\mu\nu} = \frac{\hbar^2}{2m_e} \int_{z=z_0} \left[\psi_\mu \frac{\partial \chi_\nu^*}{\partial z} - \chi_\nu^* \frac{\partial \psi_\mu}{\partial z} \right] dx dy . \quad (2.1)$$

Here \hat{z} is perpendicular to the tunneling barrier. The additional assumption of exponential decay of the states into the vacuum region then gives

$$M_{\mu\nu} = \left[\frac{\hbar^2}{2m_e} \int_{z=z_0} 2\kappa_\mu \psi_\mu(0) \chi_\nu(s) dx dy \right] e^{-\kappa_\mu s} . \quad (2.2)$$

Here m_e is the mass of the electron, z_0 is the position of an arbitrary surface separating the electrodes over which the integral is performed, and s is the width of the barrier. The condition of elastic tunneling imposes the condition that

$$E_\mu = E_\nu . \quad (2.3)$$

The decay constant of ψ_μ and χ_ν in the barrier region, κ , which by Equation (2.3) is equal for ψ_μ and χ_ν , has in the simplest approximation the form

$$\kappa = \frac{\sqrt{2m_e(\bar{\phi} - E)}}{\hbar} , \quad (2.4)$$

where $\bar{\phi}$ is the average work function of the tunnel junction.

Once the tunneling rate between states has been defined, the total tunneling current can be found by summing over all pairs of states that are available for elastic tunneling, modulated by M . This requires an occupied state on one side of the barrier, and an equal energy unoccupied state on the other.

First, the number of states must be defined. In this work, we will be dealing with metal electrodes, which can be described by a band of conductive states. In this case, a summation over states can be replaced by an integration over an appropriately defined density of states (DOS). Thus, we introduce $\rho_{A/B}$ as the DOS of sides A and B.

Next, the actual occupation ratios of these states are required. As electrons are fermions, they will occupy the states according to a Fermi distribution, defined as

$$f(E, \mu, T) = \left(e^{\frac{E-\mu}{k_B T}} + 1 \right)^{-1}, \quad (2.5)$$

where E is the energy of the state, μ is the chemical potential, T is the temperature of the system in Kelvin, and k_B is the Boltzmann constant. For the temperatures and samples used in this work, μ can be considered approximately equal to the Fermi energy E_f .

The tunneling current that arises from A to B can now be understood in a more precise form as the product of the number of electrons available to tunnel ($\rho_A f(T_A)$), multiplied by the available states in the other electrode ($\rho_B (1 - f(T_B))$), multiplied by the tunneling rate M . The difference in the tunneling current from A to B and B to A is found, and the result is integrated over all energies. This is summarized by

$$I \propto (\rho_A f_A) ((1 - f_B) \rho_B) - (\rho_B f_B) ((1 - f_A) \rho_A), \quad (2.6)$$

where $f_{A/B}$ are Equation (2.5) evaluated for $T_{A/B}$, and we have accounted for current flow in both directions. Simplifying this expression, the total tunneling current between the electrodes can be stated as [38, 39]

$$I = \frac{4\pi e}{\hbar} \int_{-\infty}^{\infty} \rho_A(E_f - eV + \epsilon) \rho_B(E_f + \epsilon) |M_{AB}(\epsilon)|^2 [f(E_f - eV + \epsilon, T_A) - f(E_f + \epsilon, T_B)] d\epsilon, \quad (2.7)$$

where V is an electric potential applied to the junction. Equation (2.7) describes in general the dependence of the tunneling current on the density of states, temperatures, and surface wavefunctions of the electrodes, and the separation between them.

As seen in these relations, the observed current as a function of V , for a particular energy, will be proportional to the product of the tip DOS and the sample DOS. The choice of tip material is thus meaningful even on the tunneling scale. For energy dependent data, an ideal tip would have a constant DOS on the energy scale in question, meaning any change in measurement

signals would arise only from the sample DOS. In practice this is not achievable, so all results are instead a convolution of the tip and sample DOS, and must be interpreted with this in mind. Results then must be stated as being for a particular combination of tip and sample, not just the sample surface, which includes measurements of Seebeck tunneling.

The additional tunneling effects we require can be investigated by considering the terms of Equation (2.7) in specific cases.

2.2 Thermally induced (Seebeck) tunneling

The central phenomenon studied in this thesis is the thermoelectric current or potential, also referred to as tunneling thermopower, induced by a temperature gradient across a tunnel junction. This is referred to as the tunneling Seebeck effect. The Seebeck effect in a continuous medium, for an open circuit condition and in the limit of small temperature gradients, has the form

$$V_{\text{therm}} = -S\Delta T, \quad (2.8)$$

where S is the Seebeck coefficient, and the temperature gradient ∇T changes to a difference $\Delta T = T_A - T_B$ for the case of an abrupt change in temperature, such as across a tunnel junction. According to semi-classical theory of electron transport in a bulk metal, S follows the Mott formula [5]:

$$S = -\frac{\pi^2 k_B^2}{3e^2} T \frac{\sigma'}{\sigma}. \quad (2.9)$$

Here σ is the electrical conductance, with the differentiation being relative to the applied potential V .

We require an equivalent expression for S in the case of a tunneling junction, starting from the tunneling current in Equation (2.7). The effect of temperature on the tunneling current is contained in the Fermi distribution term $f_A - f_B$. To understand this dependence, we can first define

$$\alpha = f(E_f - eV + \epsilon, T_A) - f(E_f + \epsilon, T_B), \quad (2.10)$$

which describes the energy interval over which Equation (2.7) is non-zero. In the limiting case of $T_{A/B} = 0$ this is a boxcar function, but as we will be concerned with finite temperatures and temperature differences this dependence must be examined in more detail.

To illustrate this, α and $\Delta\alpha = [\alpha - \alpha(\Delta T = 0)]$ are plotted as a function of E for varying values of ΔT in Section 2.2. Here T_B was kept constant,

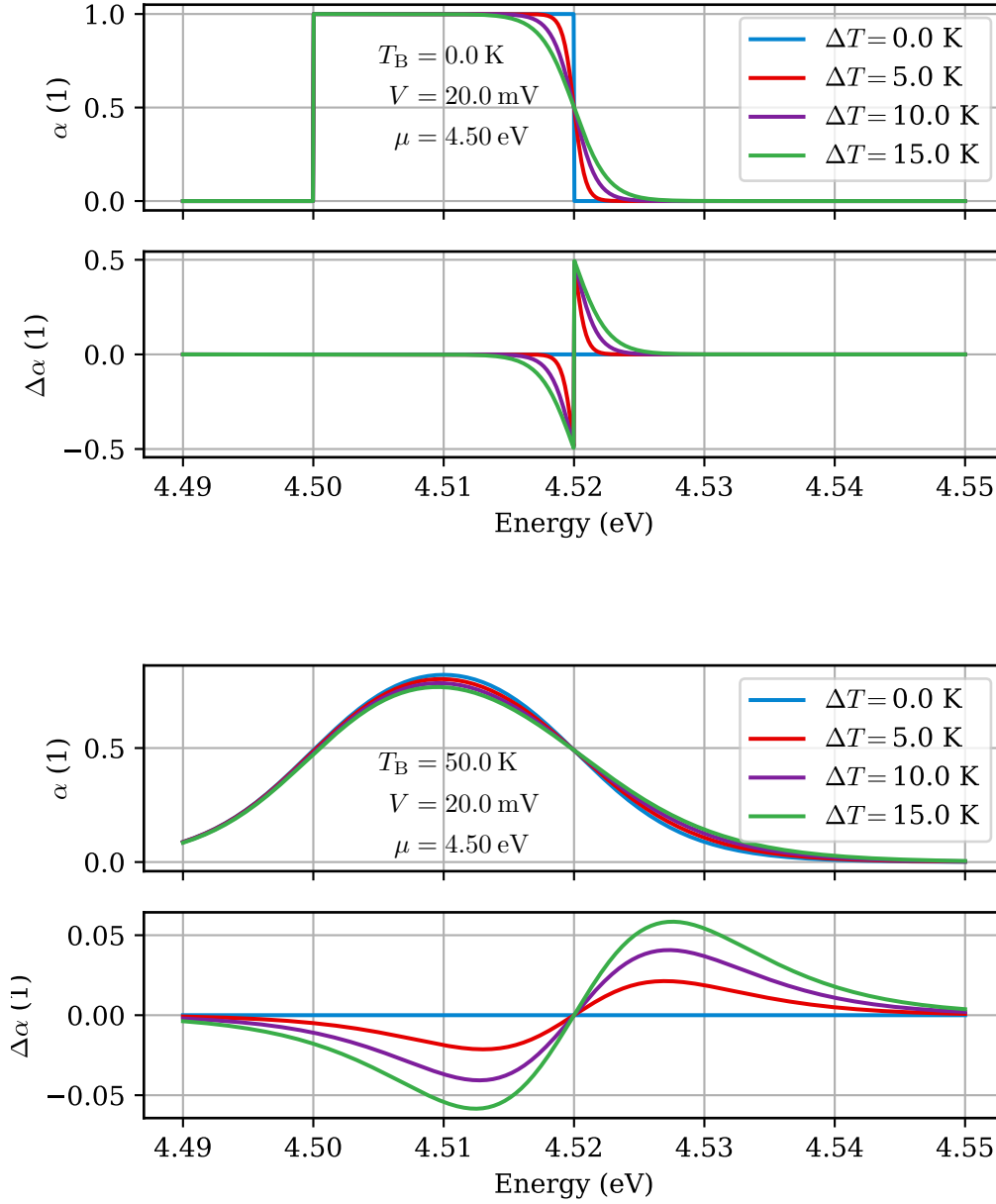


Figure 2.1: α and $\Delta\alpha = [\alpha - \alpha(\Delta T = 0)]$ plotted for a range of $\Delta T = T_A - T_B$. The base temperature $T_B = 50$ K was used for the majority of the measurements.

and values of $\mu = 4.5 \text{ eV}$ and $V = 20 \text{ mV}$ were chosen to be similar to our experiments. The upper plot, with $T_B = 0 \text{ K}$, shows a step function at $E = \mu$, corresponding to the energy of electrode B. The increased temperature of electrode A leads to a rounding off of α at $E = \mu + eV$, which is the Fermi energy of electrode A. The difference plot illustrates the symmetry of this modulation with respect to E_f . Since $I(E) \propto \alpha$, we can predict that there will be increased tunneling current from states above E_f , opposed by increased tunneling current from states below E_f . Thus, if there is any asymmetry in the DOS around E_f , this will lead to a net tunneling current, which we refer to as Seebeck tunneling.

It is also important to note which states will dominate this thermally induced tunneling current. In Section 2.2, α and $\Delta\alpha$ have been plotted with the same parameters as above, but for $T_B = 50 \text{ K}$. We see that the box function is significantly rounded on both corners by the increased temperature, and the difference plot reveals that the effects of ΔT are spread over a much larger range. The minimum and maximum of $\Delta\alpha$ occurs at a slightly higher energy, $\pm 7.5 \text{ meV}$, than the average thermal kinetic energy $E_{\text{therm}} = \frac{3}{2} k_b T$, which for 50 K equals 6.5 meV . Qualitatively, we can see from the plot that the majority of the thermal tunneling effects will occur within $|E - E_f| < 2E_{\text{therm}}$. This demonstrates the energy range of interest going forward.

A more quantitative result can be found by applying the assumption of low tunneling energies and temperatures to Equation (2.7). This has been done previously in the work of Støvneng and Lipavský [40]. For metal tunneling electrodes, the DOS will vary relatively slowly near E_f , justifying a linear approximation:

$$\rho_A \rho_B \approx \rho_A(0) \rho_B(0) + [\rho_A(0) \rho_B(0)]' E. \quad (2.11)$$

Here we have defined E as being relative to E_f . We are only interested in the thermal contribution to the tunneling current, and while the temperature will always have an effect on the current, the relative effect will be largest for small V . We will also assume that $M = M(0)$ will remain approximately constant in the energy region of interest [39], which implies a fixed electrode separation.

With these conditions, we can consider a polynomial expansion of I as a function of the bias voltage V , around $V = 0$. This has the form

$$I(V) = \sum_{i=0}^{\infty} \frac{\partial^i I}{\partial V^i} \Big|_{V=0} V^i. \quad (2.12)$$

Starting from Equation (2.7), and applying Equation (2.11), the lowest order term $i = 0$, which we will refer to as the thermal current I_{therm} , has

the form

$$I_{\text{therm}} \approx a \left[\rho_A(0) \rho_B(0) \int_{-\infty}^{\infty} (f_A - f_B) d\epsilon + [\rho_A(0) \rho_B(0)]' \cdot \int_{-\infty}^{\infty} (f_A - f_B) \epsilon d\epsilon \right], \quad (2.13)$$

where a is a constant containing M , and f is as defined in Equation (2.5). It is clear from this expression that for $T_A = T_B$ no current is expected to flow. To solve the integrals, we apply the Sommerfeld approximation, which is valid for $T \ll T_F$, where T_F is the Fermi temperature [5]. This approximation has the form

$$\int_{-\infty}^{\infty} H(\epsilon) f(\epsilon) d\epsilon = \int_{-\infty}^{E_F} H(\epsilon) d\epsilon + \frac{\pi^2}{6} (k_B T)^2 H'(E_F), \quad (2.14)$$

where $H(\epsilon)$ is a function that does not vary too rapidly over $\pm k_B T$. Applying this approximation to Equation (2.13) results in zero for the first integral, leaving

$$I_{\text{therm}} = \frac{\pi^2 k_B^2}{6e^2} (T_A^2 - T_B^2) [\rho_A(0) \rho_B(0)]' \quad (2.15)$$

However, this expression is equivalent to the Mott formula in Equation (2.9). To see this, we use the result of Equation (2.7) that [39]

$$\left(\frac{dI}{dV} \right)_{U=V} \approx \rho_A(E_F + eV) \rho_B(E_F), \quad (2.16)$$

and that for small energies

$$\sigma = \frac{dI}{dV}. \quad (2.17)$$

Equation (2.15) is still defined as a tunneling current, implying a closed circuit condition. Experimentally, this can also be measured in an open circuit, giving the condition of $I = 0$. With the polynomial expansion in Equation (2.12), we can consider the second term, giving

$$\sigma V_- - I_{\text{therm}}, \quad (2.18)$$

which finally can be expanded in the form

$$V_{\text{therm}} = -\frac{\pi^2 k_B^2}{6e^2} \frac{\sigma'}{\sigma} (T_A^2 - T_B^2). \quad (2.19)$$

Defining $T_B = T_A + \Delta T$, and assuming that $\Delta T^2 \ll T_A \Delta T$, gives

$$V_{\text{therm}} = \frac{\pi^2 k_B^2}{3e^2} \frac{\sigma'}{\sigma} T_A \Delta T = -S \Delta T, \quad (2.20)$$

with

$$S_{A/B} = -\frac{\pi^2 k_B^2}{3e^2} \frac{\sigma'}{\sigma} T_A. \quad (2.21)$$

This matches Equation (2.9), and describes the expected Seebeck coefficient for a given tunnel junction, when one side of the junction remains at a fixed temperature while the other is heated. The constant prefactor has a value of

$$\frac{\pi^2 k_B^2}{3e^2} = 24.44 \text{ nV}^2/\text{K}^2. \quad (2.22)$$

With Equation (2.21) the Seebeck coefficient of a tunnel junction as a function of $T_{A/B}$ can be calculated, given measurements of σ , σ' . This will be exploited in our later analysis to predict S in equilibrium conditions before creating a temperature gradient, to provide an independent reference for the actual thermal gradient measurements.

2.3 Magnetic tunnel junctions

We would like to investigate Seebeck tunneling in the case of magnetic tunnel junctions. To understand what to expect under these conditions, the properties of these systems must first be clarified.

The effect of the relative orientation of the electrode magnetizations on the tunneling current was studied theoretically by Slonczewski [23], explaining earlier experimental work by Julliere [41]. We will explain this effect in terms of the previously outlined Bardeen theory of tunneling, as found in the work of Reittu [42] and Chen [39]. This will enable a direct connection to the previous discussion of Seebeck tunneling.

Generally speaking, a magnetic tunnel junction occurs when one or both of the electrodes have a net surface magnetization. The origin of this magnetization will primarily be the valence electrons, which are the same entities involved in the tunneling process [5]. As electrons are fermions, with $S = 1/2$, instead of a single population of charge carriers, we must now consider two populations, consisting of spin-up and spin-down electrons, where the magnetization direction is defined relative to some convenient axis (e.g. an external magnetic field or the magnetic easy axis).

The effect of this spin dependence has consequences for both M and $\rho_{A/B}$ in Equation (2.7). To understand this, we start by examining the consequences for the tunneling between a single pair of states, described by Equation (2.2). Considering spin-dependence requires that the electron wavefunctions be described using a two-component vector:

$$\Psi = \begin{pmatrix} \psi_{\uparrow} \\ \psi_{\downarrow} \end{pmatrix}. \quad (2.23)$$

To describe the tunneling process, M must be defined between each component of both wavefunctions. Thus, a single spin-averaged term M will require four terms, with each defined analogously to Equation (2.1), with the addition of the spin component. For example

$$M_{\mu\uparrow,\nu\downarrow} = \frac{\hbar^2}{2m_e} \int_{z=z_0} \left[\psi_{\mu\uparrow} \frac{\partial \chi_{\nu\downarrow}^*}{\partial z} - \chi_{\nu\downarrow}^* \frac{\partial \psi_{\mu\uparrow}}{\partial z} \right] dx dy, \quad (2.24)$$

where

$$\psi_{\mu\uparrow} = \psi_{\mu} \begin{pmatrix} 1 \\ 0 \end{pmatrix}. \quad (2.25)$$

To make this relation useful, the states must be described in the same reference frame. As the choice of reference frame is arbitrary, it can be chosen as the magnetic easy axis (z) of electrode A. The states of electrode B, with its own arbitrary magnetization direction relative to A, must be transformed into the reference frame of A. This is done using the conventional Euler angles (ϕ , ψ , and θ) and unitary transformation matrices, giving the final result for the tunneling matrix element of

$$\mathbf{M} = \begin{pmatrix} M_{\uparrow\uparrow} & M_{\uparrow\downarrow} \\ M_{\downarrow\uparrow} & M_{\downarrow\downarrow} \end{pmatrix} = M_0 \begin{pmatrix} e^{i(\phi+\psi)/2} \cos \theta/2 & i e^{i(\phi-\psi)/2} \sin \theta/2 \\ i e^{-i(\phi-\psi)/2} \sin \theta/2 & e^{-i(\phi+\psi)/2} \cos \theta/2 \end{pmatrix} \quad (2.26)$$

where M_0 is as defined in Equation (2.1). The exponential factors will always have a magnitude of unity. Thus the tunneling current between the different states will be modulated by the angle θ between the electrode magnetizations.

As in Section 2.1, the net tunneling current is found by a summation over the available states for tunneling, modulated by M . Again the concept of the DOS can be used, in this case split into spin-dependent components:

$$\rho_{A/B} = \rho_{A/B\uparrow} + \rho_{A/B\downarrow}. \quad (2.27)$$

In a magnetized electrode, these components will not be equal:

$$\rho_{(A/B)\uparrow} \neq \rho_{(A/B)\downarrow} . \quad (2.28)$$

Using Equations (2.26) and (2.27) with Equation (2.7) gives

$$I = \frac{4\pi e}{\hbar} \int_{-\infty}^{\infty} \alpha (\rho_{A\uparrow}\rho_{B\uparrow}|M_{\uparrow\uparrow}|^2 + \rho_{A\uparrow}\rho_{B\downarrow}|M_{\uparrow\downarrow}|^2 + \rho_{A\downarrow}\rho_{B\uparrow}|M_{\downarrow\uparrow}|^2 + \rho_{A\downarrow}\rho_{B\downarrow}|M_{\downarrow\downarrow}|^2) d\epsilon . \quad (2.29)$$

Considering Equations (2.26), (2.27) and (2.29), and defining the spin-polarized DOS

$$m_{A/B} = \rho_{A/B\uparrow} - \rho_{A/B\downarrow} , \quad (2.30)$$

gives an expression for the tunneling current dependent on θ :

$$I = \frac{4\pi e}{\hbar} \int_{-\infty}^{\infty} \alpha (T_A, T_B, \epsilon) |M_0|^2 (\rho_A\rho_B + m_A m_B \cos \theta) d\epsilon . \quad (2.31)$$

The dependence of I on $\cos \theta$ is referred to as the spin-valve effect, and is the key property of magnetic tunnel junctions.

2.4 Magneto-Seebeck tunneling

The results of Sections 2.2 and 2.3 can be combined to find the effect of the tunnel junction magnetization on the thermally generated tunneling current. This effect is referred to as magneto-Seebeck tunneling, and is the central topic of this thesis.

We consider the spin-dependent tunneling current described in Equation (2.29). This can be written in a more convenient form as

$$I = \frac{4\pi e}{\hbar} \sum_{s_A, s_B} \int_{-\infty}^{\infty} \alpha \rho_{A, s_A} \rho_{B, s_B} |M_{s_A, s_B}|^2 d\epsilon . \quad (2.32)$$

where $s_{A/B}$ are the spin orientations of the electrodes. Each element in this sum has the same form as that used in our previous derivation of the thermal tunneling current. We can thus apply the same procedure to each element, starting with the linear approximation for the product of the DOS from Equation (2.11), followed by the application of the Sommerfeld approximation. Again using the matrix elements from Equation (2.26), we get a similar form to Equation (2.31):

$$I_{\text{therm}} = \frac{\pi^2 k_{\text{B}}^2}{6e^2} (T_{\text{A}}^2 - T_{\text{B}}^2) \left[(\rho_{\text{A}}\rho_{\text{B}})' + (m_{\text{A}}m_{\text{B}})' \cos \theta \right]. \quad (2.33)$$

With this result we can now expect the Seebeck value of the tunneling junction to have the same cosine dependence on the relative magnetization angle as the tunneling current. The magnitude of the effect is now proportional to the first derivative of the spin-split DOS relative to energy. Thus, if we can simultaneously measure both the tunneling conductance and the tunneling thermopower as a function of θ , we expect them to exhibit the same modulation.

2.5 Spin-polarized scanning tunneling microscopy

In the previous sections, the properties of tunnel junctions have been discussed in terms of a generic planar junction. The details of the specific wavefunctions involved in the tunneling, and the effect of non-planar geometry have not been evaluated. However, in this thesis, the previous effects have been studied in the context of scanning tunneling microscopy (STM), and thus the properties of this instrument must be discussed. In particular, the equivalence of STM to the previous planar junction must be established, in order to justify the measurement of those effects with this experimental approach.

The basic structure and primary components of a scanning tunneling microscope are shown in Figure 2.2 [39], and will be discussed further in Chapter 3. The principal challenge of this device is to maintain a constant separation between the conductive tip and sample, on the order of hundreds of pm, despite relative drift due to thermal fluctuations or mechanical noise. Furthermore the separation must be maintained whilst scanning the tip over the sample surface.

This is typically achieved via a hollow piezoelectric cylinder, on which the tip is mounted. Voltages applied to opposing outer faces of the tube will deflect the tip laterally, where the coordinates x and y are defined as parallel to the sample surface. Another electrode, covering the entire inner area of the cylinder, will extend or retract the tip, according to the sign of the voltage, providing vertical (z) deflection. Both the tip and the sample are electrically isolated, with single lines allowing for the application of a bias voltage and the measurement of the tunneling current.

The difference between the tunneling junction of an STM and the previously discussed ideal planar junction is the geometry of one of the electrodes; the tip. The tip of an STM is sharpened such that tunneling will now occur

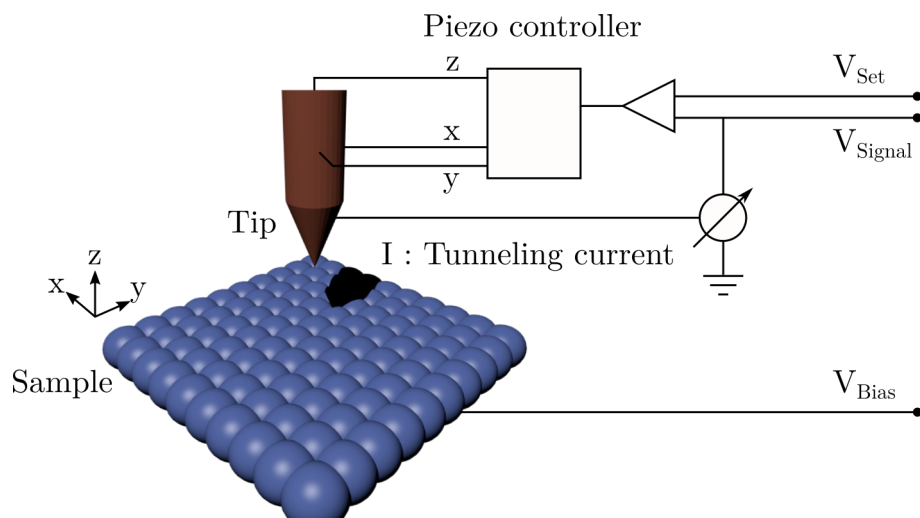


Figure 2.2: A standard scanning tunneling microscope consists of an atomically sharp conductive tip, mounted on a piezoelectric cylinder, approached to within tunneling distance of a conductive sample. A voltage V_{Bias} is applied across the junction to generate a tunneling current I . A current-to-voltage amplifier converts I into an output signal V_{Signal} , and a feedback loop adjusts the tip height to match V_{Signal} to V_{Set} . The tip is then raster-scanned over the sample, and the tip height and tunneling current are recorded over time, creating a topographic map of the surface.

primarily between a single apex tip atom and the local states on the surface beneath this tip. Considering again the exponential decay of the surface state into the vacuum barrier, the overlap between the tip and sample wavefunctions will occur only in a small region directly beneath the tip, which gives the STM its localized imaging capabilities.

To make the connection to Equation (2.1) explicit, the tunneling matrix element M is again found, now for an STM junction. For a planar junction, the integration was over a plane at $z = z_0$, assumed to lie roughly in the middle of the two electrodes. For this tip-sample geometry, as pointed out in [39], one can modify Equation (2.2) to be an integration over a non-planar separation surface Σ . This has the form

$$M_{\nu\mu} = \frac{\hbar^2}{2m_e} \int_{\Sigma} (\psi_{\mu} \nabla \chi_{\nu}^* - \chi_{\nu}^* \nabla \psi_{\mu}) d\mathbf{S} \quad (2.34)$$

where the wavefunctions ψ and χ , previously defined as being for the electrodes, are now the wavefunctions of tip and sample, as noted in Figure 2.2. The choice of integration surface is again not critical, but will generally lie between the tip and sample.

However, this three-dimensional form is entirely compatible with the previous derivation of Seebeck tunneling, following the same approximations and substitutions, meaning we also expect thermally-induced electron tunneling to be present in a STM [40]. In addition, with this change, one can see that the previous arguments for spin-sensitive tunneling apply equally well to the case of an STM. This special case is known as spin-polarized STM (SP-STM) [43], and has been used extensively to investigate surface magnetism [44, 45, 46, 47].

Thus, by this reasoning, a scanning tunneling microscope is a suitable tool for studying Seebeck tunneling, and the addition of a spin-polarized tip and sample should make possible the observation of magneto-Seebeck tunneling.

Chapter 3

Experimental implementation

This Chapter describes our approach to measuring the tunneling effects outlined in Chapter 2, in the context of a spin-polarized scanning tunneling microscope (SP-STM). This requires three major components: the creation of a stable and controllable magnetic tunnel junction (MTJ); the control and measurement of both the equilibrium temperature and temperature gradient across this junction; and the measurement of the resulting electric potential while maintaining the previous conditions. First, we will describe in Section 3.1 the STM instrument, tips, and samples used in this work to create a reliable MTJ. Starting from this basic configuration, the modifications necessary to perform the measurements can then be elaborated in subsequent sections. Section 3.2 will discuss the method of temperature control in more detail, including the creation of a temperature gradient. The experimental description will be completed with Section 3.3, with a discussion of the measurement of the tip-sample potential, in the context of the previous two sections, giving a complete method for measuring S . Section 3.4 and Section 3.5 will present two supplementary methods for determining S that will be used to validate the main approach. The Chapter will close in Section 3.6 with a summary of the experimental protocol for the later measurements.

3.1 Creating a magnetic tunnel junction

The first requirement for the experiments is the creation of a magnetic tunnel junction. For purposes of lateral resolution and precise control of the tunneling junction properties, a scanning tunneling microscope was used to achieve this. First the design of the STM itself will be presented, which enables high-resolution, low-noise positioning of a tip and sample in tunneling contact. This includes the ultra-high vacuum system needed to maintain

clean sample surfaces, and the cryostat and thermal properties that enable stable equilibrium temperatures. With this established, the choice of tip and sample to create the desired junction properties can be discussed.

3.1.1 A variable-temperature scanning tunneling microscope

The central idea of STM was previously mentioned in Section 2.5. Here we will discuss the experimental requirements for the apparatus, and the experimental implementation that matches these conditions.

To reiterate, the goal is to position a sharp conductive tip within tunneling distance of a conductive sample whilst measuring the tunneling current at sufficiently high speeds to allow making picometer scale (with nanometer range) adjustments to the tip height via a fast-reacting feedback loop. This feedback system must operate at sufficient speeds to allow for laterally scanning the tip with sub-ångström lateral precision over the sample while countering changes in tip-sample separation from vibrational noise and scanning over both gradual and abrupt topographical changes (e.g. atomic step edges).

In addition, in our experiments the differential conductance, $\frac{dI}{dV}$, is used extensively, both as a measurement channel and as a feedback signal. This is measured using a lock-in amplifier, which applies a small excitation bias at a particular frequency, and measures the amplitude and phase of the resulting signal at the same frequency after the tunnel junction. This requires a time-resolved measurement of the current at the chosen excitation frequency. Thus the current measurement must also have sufficiently high bandwidth to allow for this measurement at frequencies higher than the rate of change in any signal of interest.

To match these requirements, the measurements in this thesis were performed using a home-built STM, constructed by Torben Hänke, further details of which can be found in his doctoral thesis [48]. An image and schematic of the STM are shown in Figure 3.1, taken from the thesis. Here one can see the actual STM itself, the body of which is constructed out of gold-plated phosphor bronze. The sample plate, an example of which can be seen in Figure 3.2, can be inserted into the electrically-isolated (from the body) receptacle above the tip. A single wire then connects outside of the STM for biasing the sample. A temperature sensing diode (GaAs/GaAlAs) is fixed with a thin layer of glue to the STM body, inside of the cavity, very near to the sample. Two curved-wire springs act to fix the sample plate inside of the slot, to dampen vibrations.

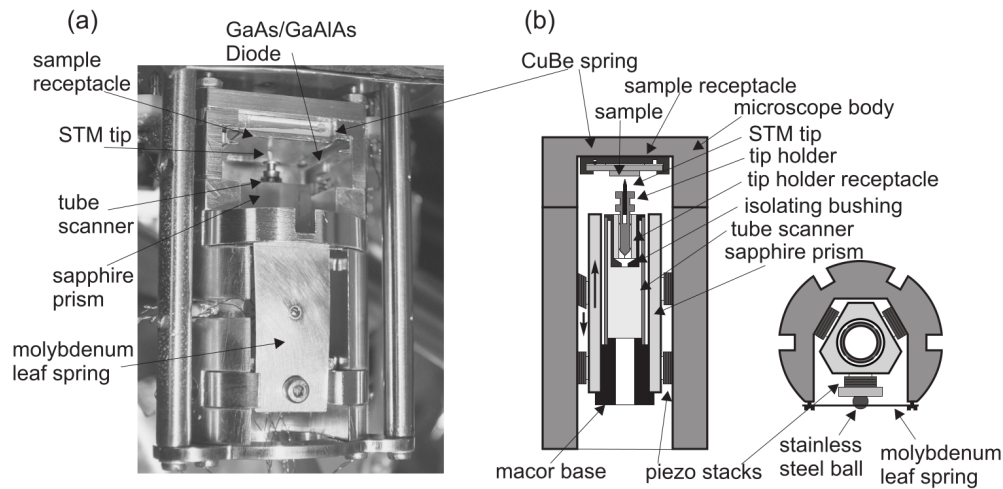


Figure 3.1: Figure taken from [48]. (a) The scanning tunneling microscope used in the experiments. The position of the tip, and the receptacle for the sample plate are indicated. The GaAs/GaAlAs thermal diode is positioned near the sample, directly connected to the STM body. The tip, tube scanner, and sapphire prism, are moved vertically in coarse steps used a stick-slip piezo-stack method, and the tip can be scanned in precise picometer movements via the indicated scanner tube. (b) Schematic view of the STM. The sample receptacle is electrically isolated from the STM body by a thin layer of non-conductive glue. The tip and tip holder are isolated from the scanner tube by an insulating ceramic bushing, as indicated. For further electrical noise isolation, there is a conductive coating on part of the bushing, which has a dedicated electrical connection outside of the STM for grounding.

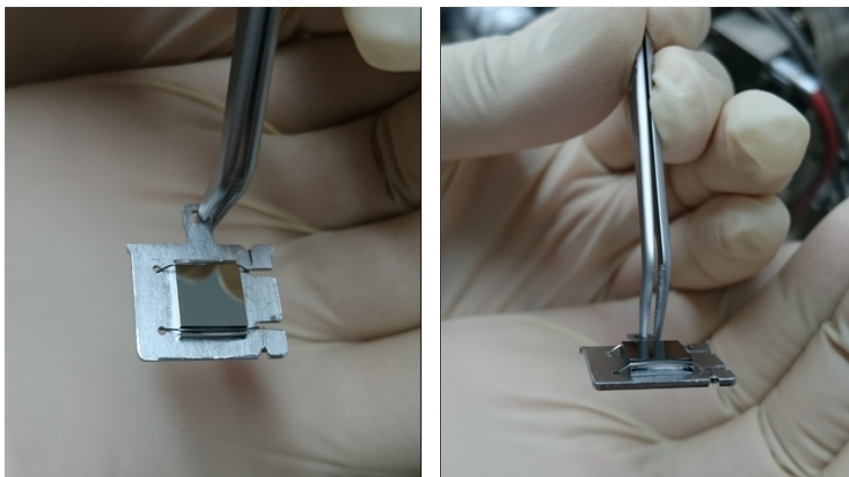


Figure 3.2: A bound metallic crystal on a sample plate.

The tip is fixed inside a metal tip holder, either by pressure or conductive glue. This holder is then fixed into the tip receptacle, held by a spring. The holder is designed such that a shuttle can be used to insert and remove the tip holder inside of the STM without opening the chamber, allowing for tip exchange. The tip receptacle sits inside an electrically insulating ceramic piece, which is then glued to the top scanner tube. The glass-ceramic Macor was used, for its machineability and thermal properties [49]. Another ceramic piece joins the bottom of the scanner tube to the sapphire prism. This prism, which must maintain its shape at a wide range of temperatures, is clamped between three sets of two piezo stacks. These stacks are driven with a sawtooth voltage pattern, which results in a stick-slip motion of the prism. With this method, the tip can be driven in coarse steps perpendicular to the sample at a wide range of temperatures, while still being stiffly clamped to the STM body for relative vibration reduction.

The entire STM is contained within a stainless steel chamber, capable of being pumped down to ultra-high vacuum (UHV) pressures below 1×10^{-10} mbar. This ultra-low pressure allows for atomically clean sample surfaces to be prepared and maintained on the timescale of weeks, barring contamination during the course of an experiment. This pressure is achieved by first baking the system for days at 120°C with running turbomolecular pumps. This removes any water inside the system, which can be verified used quadrupole mass spectrometers. After baking, continuous pumping using ion getter pumps, titanium sublimation pumps, and non-evaporable getter pumps [50], brings the pressure into the UHV regime. The turbomolecular pumps can be used during sample preparation as required, e.g. during high partial pressure annealing, but remain off for scanning.

Surrounding the STM is a heat shield, shown in Figure 3.3. Instead of being exposed to incident thermal radiation from the surrounding room-temperature UHV chamber, the STM will only be exposed to the radiation from the shield. If the shield is cooled, in this case by exhaust gases from the flow cryostat, the reduction in ambient radiation will allow the STM to reach significantly lower temperatures. The STM itself is suspended on three stainless steel rods inside of the shield, which provide the majority of the heat input into the device at low temperatures.

The cooling of the STM is achieved using a flow-cryostat, which uses a continuous flow of cryogen, in our case liquid helium, to cool a metal block inside of the UHV chamber, which effectively acts as a heat exchanger. The thermal connection between this block and the STM is provided by braids of thin silver-plated copper wires, which can also be seen in Figure 3.4. These are screwed onto the cooling block, and fed through a hole in the heat shield to connect to the STM itself. A second braid, attached to the

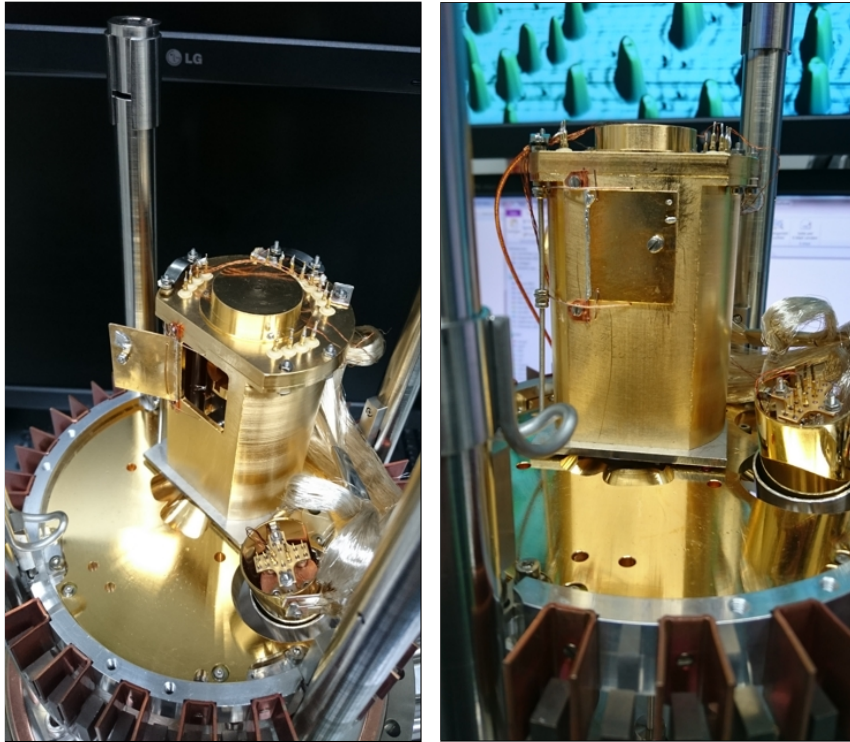


Figure 3.3: The heat shield of the STM, shown from two angles. The heat shield is cooled by the exhaust gas of the cryostat, resulting in a temperature somewhere between room temperature and the STM temperature. This results in the STM being exposed to a reduced temperature of thermal radiation, which is essential for efficiently reaching cryogenic temperatures. The electrical feedthroughs at the top of the shield allow for electrically isolated connections through the shield, between a UHV electrical feedthrough flange and the STM itself.

warmer side of the heat exchanger, is used to cool the heat shield, giving it a temperature intermediate between room-temperature and the equilibrium STM temperature.

A heater built into the cryostat can be used to warm the block, thereby allowing for fine adjustment of the final temperature. In practice, this heater is connected to a proportional-integral (PI) feedback controller which, combined with control of the liquid He flux, can be used to achieve an arbitrary temperature at the STM. This system is relatively stable against fluctuations in the temperature of the room or small variations in the He flow rate.

With this approach, the equilibrium temperature of the entire STM can be adjusted from room temperature, down to approximately 25.5 K. The details of the deliberate creation of a thermal gradient inside of the system will be discussed in Section 3.2.

Both the tip and the sample are connected to isolated feedthroughs in the top of the shield via low thermal conductance kapton-coated manganin wires, with a diameter of 50 μm . These cables have a resistance of $\approx 50 \Omega$. Since the resistance of the tunneling junction is usually in the range of $\text{M}\Omega$, this cable resistance is relatively negligible, ensuring that the applied potential set in the controlling electronics is practically the same as that applied to the tunneling junction.

The heat shield is mounted to an eddy-current damping stage. This is shown in Figure 3.4. The STM stage is suspended from soft springs inside of vertical stainless steel cylinders, of which three can be seen. Surrounding the edge of the stage is an interlocking set of permanent magnets, fixed relative to the chamber, and copper U-pieces mounted to the stage. As the stage vibrates, the change in magnetic flux through the copper pieces will induce eddy currents which will then, via Lenz's law, induce counter currents. These counter currents will interact with the magnets and oppose the motion, leading to effective damping [51].

This method of vibration damping is broadly effective with respect to frequency [52], which is especially important when using a flow cryostat, which will add significant vibrational noise to the system. However, a critical drawback is that the magnetic damping is incompatible with any strong externally applied magnetic field. This necessitates a careful choice of tip and sample in order to create the desired magnetic tunnel junction features, which will be discussed in later sections.

Electrical system

In principle, three separate subsystems for the control of the STM can be defined; the driving electronics for the coarse piezo stacks and the scanner

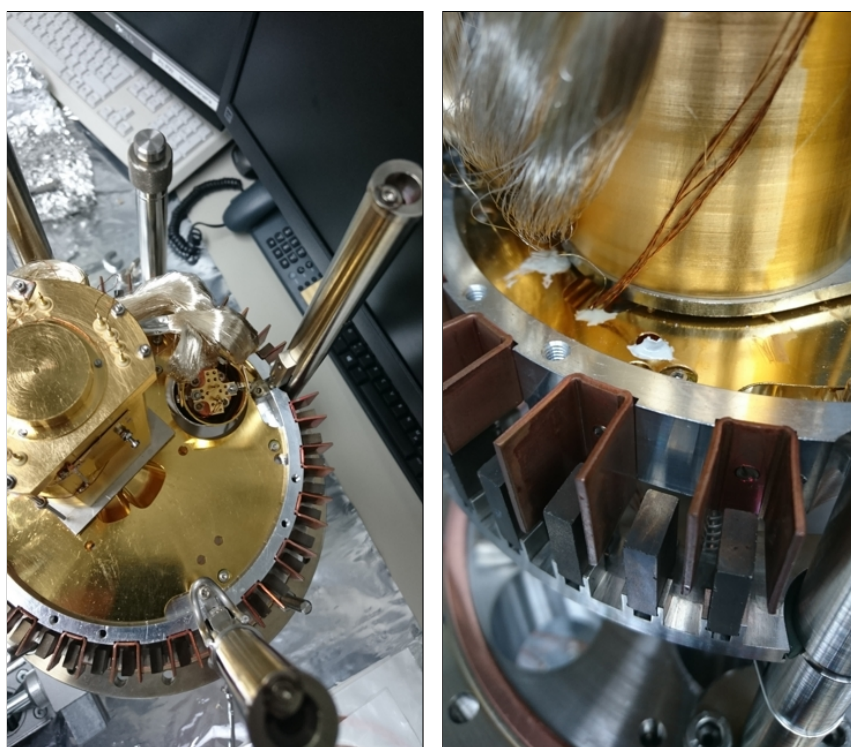


Figure 3.4: Eddy-current damping stage, on which the STM is seen mounted. The magnetic suspension acoustically decouples the instrument from the chamber, providing vibrational isolation.

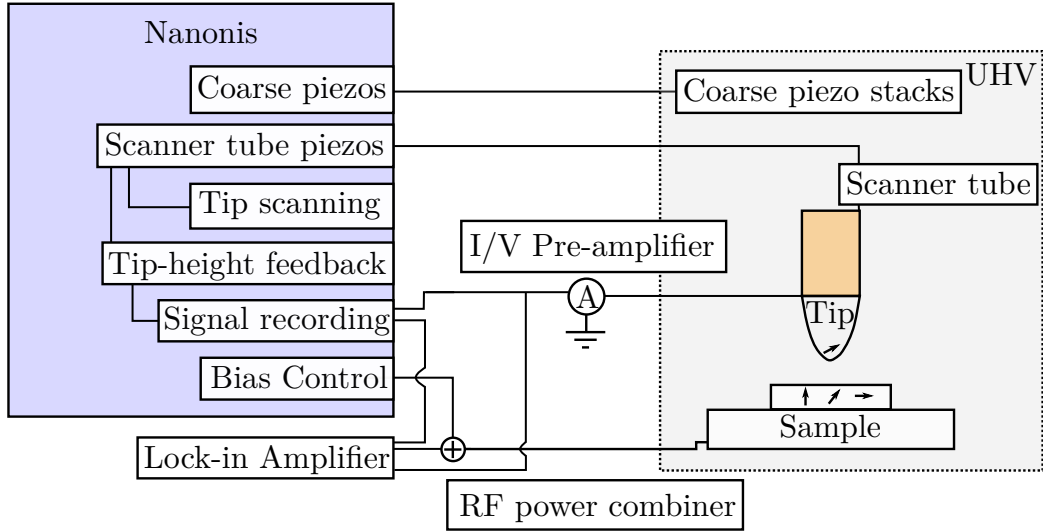


Figure 3.5: Schematic layout of the electronic subsystems of the STM. The logical connections shown inside of the Nanonis system are entirely digital. This allows for quickly switching between alternative signals for the feedback control, executing arbitrary logical operations on scanning parameters, and programmatically controlling the applied potential.

tube, the signal generation for both constant (DC) and time-varying (AC) signals, and the tunneling current detection system.

A schematic of the electronic system of the STM is shown in Figure 3.5. Three main components provide the required functions; the Nanonis controller, the lock-in amplifier, and the I/V pre-amplifier.

The Nanonis control system stack [53] contains the high-voltage (HV) amplifier necessary for driving the STM piezoelectric elements, and an internal computer controlling a field-programmable gate array (FPGA), which is configured to control the tip position feedback loop. A signal input/output breakout box allows for arbitrarily programmable output signals and simultaneous recording of ± 10 V signals.

In practice, at least four of the output channels will be dedicated to basic STM control; the lateral (x/y) and vertical (z) piezo signals, which are connected to the HV-amplifier, and the tip-sample bias potential $U = eV$. Correspondingly, two input channels will be used at a minimum, for recording both the tunneling current I and $\frac{dI}{dV}$. The tunneling current signal is provided by a Femto DLCPA-200 transimpedance I/V pre-amplifier [54], which converts the tunneling current directly after the STM into a proportionally scaled ± 10 V signal, which is directly measured by the Nanonis. In this configuration the tunneling junction is virtually grounded on the tip side.

For measuring $\frac{dI}{dV}$, a lock-in amplifier is used. The majority of the measurements were performed with a Stanford Instruments SR830 amplifier, with some additional data gathered using a Zurich Instruments MFLI amplifier. While the details of their implementation differ, primarily in the analog approach of the SR830 versus the fully digital MFLI, the basic principle of demodulation of I , or a voltage proportional to I , at a specific frequency is the same. The Nanonis also has a lock-in capability, through internal digital processing, but the performance of the dedicated hardware units was found to be superior.

To apply the excitation signal, the output of the amplifier is combined with the DC bias potential from the Nanonis using a Mini-Circuits ZFRSC-183-S+ RF power combiner. This combined signal is then connected to the sample side of the STM. The measured tunneling current from the Femto pre-amplifier is split off with a T-junction and connected to the input of the amplifier. The lock-in amplifier will then provide an output voltage proportional to the amplitude of the tunneling AC signal, which is connected to a signal input on the Nanonis. With this approach, the Nanonis can measure $\frac{dI}{dV}$ simultaneously with I , meaning that images of the topography, current, and $\frac{dI}{dV}$ are all produced with a single scan.

The actual operation of the STM is done using the Nanonis software interface, based on LabVIEW. This is a program for setting all scanning parameters, including calibration constants for converting HV piezo signals into distances, sizes and positions of scanning areas, and feedback parameters. This software approach to instrument control also allows the possibility of creating arbitrary sequences of measurement actions via a programming interface. Modules for performing various forms of spectroscopic measurements, most importantly fixed bias and/or fixed tip position, are also available.

3.1.2 Tunneling tips

The primary goal of this work is to demonstrate that magneto-Seebeck tunneling can be observed using an STM. To do this, the base effect of non-magnetic Seebeck tunneling will first be established, before considering a magnetic tunnel junction. We thus require two tip materials; non-magnetic and magnetic. As we only require a verifiable observation of the effects, the particular choice of material, which will affect the magnitude of the signal, is not initially critical.

The choice of material for the STM must simultaneously satisfy a general set of requirements for tunneling tips and the specific conditions imposed by the particular experiment. The first issue with a tip is the fabrication. A

sharp tip, both on the macroscopic and microscopic scales is desired. Once stable atom-to-atom tunneling is achieved, this will only be dependent on the actual atomic species, but reliably achieving this contact requires consistent tip fabrication procedures.

The macroscopic formation can be done with a diversity of methods, including mechanical shearing and electrochemical etching [55]. This must be a somewhat reliable process, as each tip must be brought into the vacuum chamber and prepared before testing, which is a time-consuming process.

With electrochemical etching, a shard a few centimeters long is first cut from the bulk material, which is either a film or a rod. After rough shaping to fit the tip holder, approximately half of it is then coated with a non-reactive film (e.g. nail polish), and suspended (coated surface downwards) in an etching solution, with the uncoated surface just touching the top of the liquid. The choice of solution depends on the tip material. A current is run through the shard, into the solution, with a circular electrode in the solution ensuring a homogeneous etching rate around the circumference of the tip. At the interface between the material and the solution, the etching process then begins. This will continue until the hanging section breaks off, leaving a sharp point on the fixed upper section. The current is then stopped, either manually or using a cut-off circuit which senses the open circuit between the remaining material and the bath. If further etching were allowed to occur, it would result in a more rounded tip. The uncoated section can then be used as an STM tip.

After etching, or other mechanical means of fabrication, the next issue is the formation of insulating oxides on the metal surface during production or transport [56]. These layers, common on metals, are difficult to avoid with room-condition fabrication, and due to their insulating nature can inhibit stable tunneling contact. This leaves the options of either fabrication and transport in a neutral atmosphere (practically difficult) or, more commonly, further in-situ processing.

In the UHV chamber, the tip can be quickly heated to high temperatures (flashing), to evaporate any oxide layer [57]. As this is achieved using electron-beam heating, with the tip apex closest to the electron source, the tip apex will experience the greatest heating, causing it to reform and present a fresh tip surface.

Once a macroscopically stable and microscopically clean tip has been formed with these processes and brought into tunneling contact, the imaging may still be of poor quality. A few common problems include: fast-switching of the tip electronic state, which will appear as high-frequency noise in the resulting signals; tip instability which can lead to material loss on the sample surface; malformed tip apex which leads to direction-dependent imaging or

incorrect topography; or the appearance of double-tip effects, which appear as identical copies of features in an image, due to the tip apex switching to a nearby cluster while scanning.

To address these problems, the microscopic tip configuration must be changed. This is usually done either by electrical pulsing of up to 10 V over 200 ms, or controlled dipping of the tip into the sample. In the first case, since this is done with the tip in tunneling contact with the sample, the close proximity and sharp tip apex will lead to very large field gradients. This is often sufficient to either reconfigure the tip apex or entirely remove tip material, resulting in a new tunneling site. This can be done repeatedly, until a desirable tip is found.

The second approach of controlled tip preparation involves driving the tip a few 100 pm into the sample, followed by application of a finite bias voltage and a relatively slow withdrawal of the tip, on the timescale of seconds, out of the sample. This leads to a high current density through the atomic-scale contact junction, which ideally melts the material. One interpretation is that as the tip pulls away, this melted region is stretched and breaks, resulting in a sharper material.

However, as the procedure cannot be reliably imaged, at least in our apparatus, the actual details of the process are unavailable. However this is not a problem, as long as the resulting tip is sharp. One concern with this technique is that the clean tip surface can be contaminated by the sample material. Thus, if a rigorously clean tip is required, this technique should be used with caution.

Only once these issues have been dealt with, can the resulting images be interpreted in terms of the tunneling current in Equation (2.7), and the resulting effects discussed in Chapter 2.

W tip for non-magnetic imaging

Considering the requirements previously listed, a bulk W tip was used to gather the non-spin-polarized data. This is a common tip material in STM [55], used both bare and with various coatings, with preparation procedures compatible with UHV conditions.

The tip was fabricated using electrochemical etching, in a potassium hydroxide solution [55]. Once inside the UHV chamber, the tip was flashed for 7 s, with an emission current of $I_{\text{em}} = 40$ mA, with a HV of 500 V, to remove any oxide or other impurities. Once inside the STM, further tip preparation was performed by electrical pulsing.

Bulk Cr tip for magnetic imaging

To produce a magnetic tunnel junction, a tip material with a stable magnetic ground state is required. The experiments will be performed at cryogenic temperatures, which allows for additional materials to be considered, other than the usual room temperature ferromagnets such as Fe, Ni, or Co. We will be imaging nanoscale magnetic structures. At these size scales, the coercivity of the magnetic states can be quite low [58]. Thus, a tip with a minimal magnetic dipolar stray field is also required.

These requirements are met by bulk Cr tips. The magnetic properties of these tips have been studied previously [59, 60], and bulk Cr tips have been used in many SP-STM studies [61]. At cryogenic temperatures, bulk Cr is anti-ferromagnetic. This means that a minimal stray field will be produced by the tip, as compared to a ferromagnetic material such as Fe. While the spin polarization of the tunneling current is generally lower than with ferromagnetic tips [59], the anti-ferromagnetic character is sufficiently advantageous to outweigh this cost.

For our experimentals, Cr tips were produced similarly to the W tips. The bulk material was a 99.99% pure Cr film. The tip was again electrochemically etched, this time using a hydrochloric acid solution, and prepared in-situ using only electrical pulsing [62]. With each restructuring of the tip apex, the tip magnetization will in general change. Through repeated cycles of pulsing and scanning of known magnetic structures, the desired tip magnetization orientation can be achieved.

Steel tip

For the measurement of the Fe ML islands, a steel tip was used. Originally, a Cr tip was intended to be used. However, a material supplier error led to a steel tip being prepared instead, using the same procedure as described for the Cr tips. However, it was found that the tip performed well during the experiments, and resulted in well-defined topographic images and distinct magnetic contrast. This was attributed to an Fe cluster being at the tip apex. Thus, the tip will effectively be considered equivalent to an Fe-coated W tip, a commonly used tip system for SP-STM.

3.1.3 Sample systems

With the previously described STM instrument, and having selected appropriate tunneling tip materials, all that remains for creating a magnetic tunnel junction is the choice of sample surface. Before attempting to mea-

sure additional thermal tunneling effects, an understanding of the features and contrast expected using regular STM and SP-STM is necessary. This baseline is critical for understanding the changes that will arise from the addition of the thermal gradient. Thus, for each prepared sample system the preparation technique, as well as STM and SP-STM data will be presented, and compared to literature results where possible. In this way, the presence of the correct surface can be assured.

As described in Section 2.5, the conductive surface must be prepared atomically flat, and for this STM (Section 3.1.1), we have the restriction that no external magnetic field is available. However, as per our prediction of the cosine dependence of Seebeck tunneling on the relative orientation of tip and sample magnetizations Θ (where $\Theta = \theta_{\text{tip}} - \theta_{\text{sample}}$) in Section 2.4, we require access to multiple values of Θ in a single experiment, without re-preparing the tip or sample.

To achieve this, sample systems were chosen with magnetic ground states exhibiting multiple magnetization directions on the scale of tens of nm. Three systems, each with particular advantages, were investigated. In all cases, the general procedure is the same: A clean substrate is produced by a combination of Ar⁺ sputter, O₂ annealing, and high-temperature flashing. An electron-beam evaporator is then used to deposit the required material on the sample. This can be followed by further sample annealing, promoting the desired growth mode of the surface.

Fe DL on W(110)

The primary system used in the experiments was the atomic double-layer (DL) of Fe on a W(110) substrate. This is a well-known magnetic system, which has been the subject of many previous SP-STM studies [44, 63, 59].

Of key interest is the magnetic ground state at low temperatures. This has, in previous works, been characterized as alternating out-of-plane magnetic domains, separated by chiral domain walls [63]. In a uniform DL stripe, with no external magnetic field, these domains will be of approximately equal size. The chiral sense of the domain walls is given by the presence of the Dzyaloshinskii-Moriya interaction, arising from the interface between the magnetic Fe and the W substrate, with its strong spin-orbit coupling.

To prepare the surface, a clean W(110) sample is first produced. This follows the work of Bode et al. [57]. To start, a freshly inserted W crystal will have accumulated an oxide layer due to atmospheric exposure. As the melting point of W is very high ($\approx 3400^\circ\text{C}$), this layer can be removed by high temperature flashing.

After this, the sample is still left with significant carbon impurities in

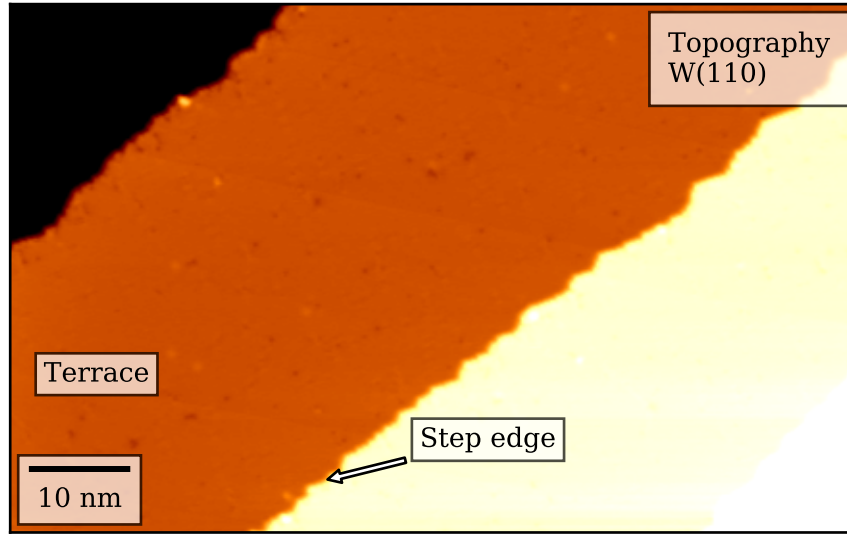


Figure 3.6: Topographic image of the clean W(110) surface, imaged with a W tip, $V = 1$ V, at a current setpoint of $I = 100$ pA. The STM temperature was $T = 50$ K. The average terrace width is approximately 30 nm, and the average step height is 200 pm.

the bulk. To remove these requires annealing the sample at an elevated temperature of ≈ 1300 °C, in a high O_2 partial pressure of 2×10^{-6} mbar. The carbon on the surface will react with the O_2 atmosphere to produce CO [64]. The raised temperature increases the mobility of the bulk impurities, which can migrate to the surface for reaction. It is assumed that these CO molecules will remain on the surface, forming a layer. After annealing for some time, another high temperature flash is applied, removing the CO layer. The procedure is repeated whilst stepwise decreasing the partial pressure of O_2 to 8×10^{-8} mbar.

To verify that the surface was clean, it was imaged with conventional STM. This is generally done once to verify that the preparation procedure was correctly performed. For further preparations with the same parameters, the surface is then assumed to be clean. The resulting surface is shown in Figure 3.6. As can be seen, this method produces atomically flat terraces, suitable for deposition of further materials.

With this completed, approximately 1.5 atomic layers of Fe were then evaporated onto the surface, followed by at least ten minutes of further annealing at >220 °C. At this temperature, the Fe clusters deposited on the surface will dissociate into a single atom thick wetting layer. The DL will

then grow, in a step-flow fashion, on top of this layer [65, 66]. At higher temperatures, instead of a flat DL, taller islands will be the preferred growth pattern [66], which must be avoided. The required evaporation parameters were known from previous experiments with this instrument, and by comparing repeated preparations to published examples of the target surface.

A representative example of the produced surface is shown in Figure 3.7, imaged using a W tip. The annotated features, including the step-flow grown terraces, dislocation lines, and difference in $\frac{dI}{dV}$, are consistent with known structures from the literature, confirming that the correct surface was prepared. The dislocation lines are parallel to the [001] direction, giving a fixed reference orientation on the surface.

A particularly interesting feature is the clearly visible darker lines across the terraces. These are in fact the magnetic domain walls, imaged via tunneling anisotropic magnetoresistance (TAMR) contrast. This has been previously observed in this tip-sample system [67]. The origin of this effect is the strength of the spin-orbit coupling at the surface. The non-easy-axis alignment of the local magnetization will apply a torque on the electron orbits via this coupling. This will lead to an energetic shift in the local DOS which, as per the relationship in Section 2.1, will manifest as a change in the $\frac{dI}{dV}$ signal. It must be emphasized that this effect is purely dependent on the sample magnetization, θ_{sample} , and not on Θ . We thus classify it as an electronic tunneling effect, which must be accounted for when attempting to extract the purely magnetic signal.

To characterize this quantitatively, it has been found that, similarly to the spin-valve behaviour, this effect will have a sinusoidal dependence on the sample magnetization direction, θ_{sample} , defined relative to the easy axis [63]. If one considers an in-plane profile perpendicular to the domain wall, the change in contrast has been found to have the form

$$\sigma(r) = y_0 + y_{\text{SOC}} \sin^2(\theta_{\text{sample}}(r)) , \quad (3.1)$$

where the differential conductance σ is a function of the lateral dimension r , y_0 is a surface dependent offset, and y_{SOC} is the magnitude of the TAMR modulation.

Previous work has assumed a Bloch wall profile for θ_{sample} , given by [63]

$$\theta_{\text{sample}} = \arcsin\left(\tanh\left(\frac{r - r_0}{w/2}\right)\right) , \quad (3.2)$$

where w and r_0 are the width and position of the domain wall, respectively. However, later work has shown that the walls are in fact of the Néel type [68], with a lateral profile of the form

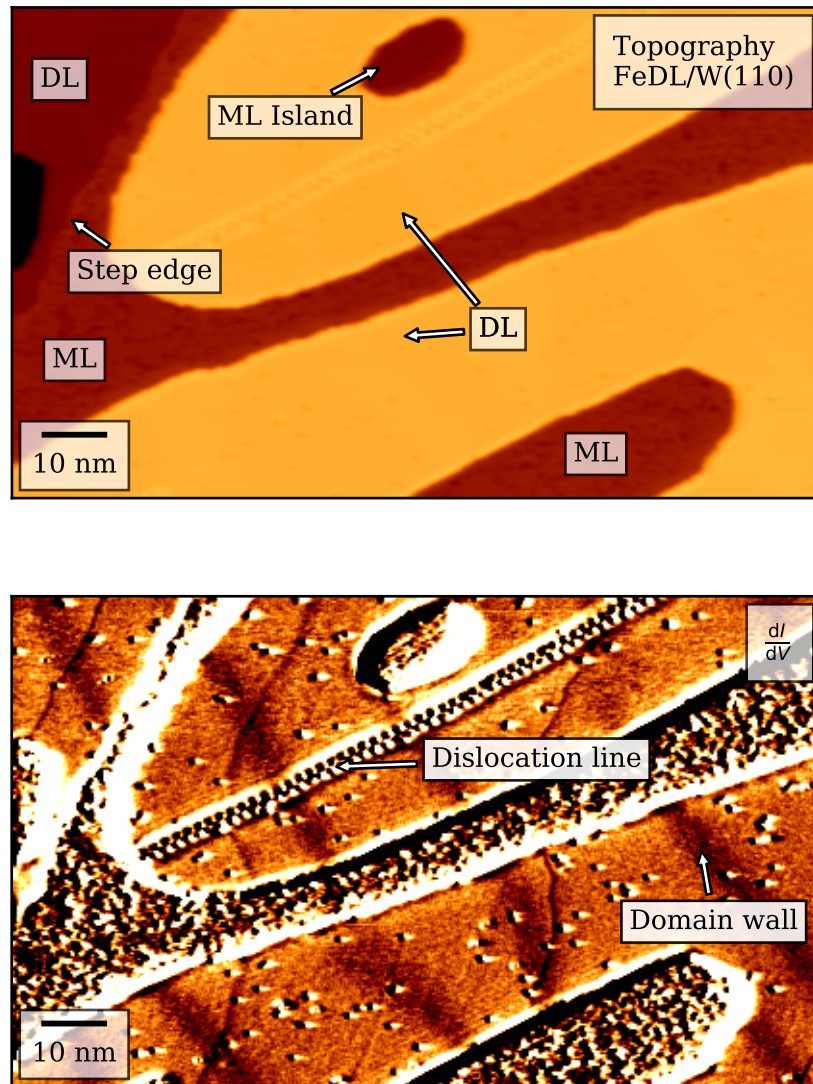


Figure 3.7: Topographic and differential conductance image of the Fe DL on W(110), imaged using a W tip, with $V = 25$ mV, $I_{\text{set}} = 1$ nA, and $T_{\text{STM}} = 50$ K. $\frac{dI}{dV}$ was measured at 4.3 kHz, with a modulation amplitude of 40 mV.

$$\theta_{\text{sample}} = \pm \arccos \left(\tanh \left(\frac{K}{A} (r - r_0) \right) \right). \quad (3.3)$$

Here K is the anisotropy coefficient, A is the spin stiffness, and the sign of the function is determined by the handedness of the domain wall rotation.

Both functions can be used to fit a lateral profile of the same domain wall magnetization when only the relative change in signal is being considered, since

$$\arccos(\theta) = \frac{\pi}{2} - \arcsin(\theta). \quad (3.4)$$

The constant $\pi/2$ offset will be accounted for in the profile by a difference in y_0 , and the sign of y_{SOC} will be opposite for the two domain wall types.

We will consider here the walls to be of the Bloch type. Thus, a line profile across a single domain wall should have the form

$$\sigma(r) = y_0 + y_{\text{SOC}} * \sin^2 \left(\arcsin \left(\tanh \left(\frac{r - r_0}{w/2} \right) \right) \right). \quad (3.5)$$

Multiple domain walls can be modeled by a summation of each wall's contribution to θ_{sample} :

$$\theta_{\text{sample}} = \sum_i \arcsin \left(\tanh \left(\frac{r_i - r_0}{w/2} \right) \right), \quad (3.6)$$

where the summation is over the individual wall positions r_i , and w has been assumed to be constant.

To demonstrate the applicability of the model, a line profile has been extracted from the image in Figure 3.7, and been fitted with the model of Equation (3.1). The result is shown in Figure 3.8.

From the line profile, we can see that the TAMR contrast is clearly visible, and the model is well-suited to describe it. As a general method of quantifying the strength of a signal, relative to some baseline, we can define

$$S(y) = \frac{y - y_0}{y + y_0}. \quad (3.7)$$

For the TAMR contrast, this gives $S_{\text{SOC}} = -7\%$. This relative definition is in general better for quantifying such effects, as the actual magnitude will vary with the specific settings used for the measurement. The wall width of $w = 4.9 \text{ nm} \pm 0.3 \text{ nm}$ is smaller than the literature values [63]. However, a

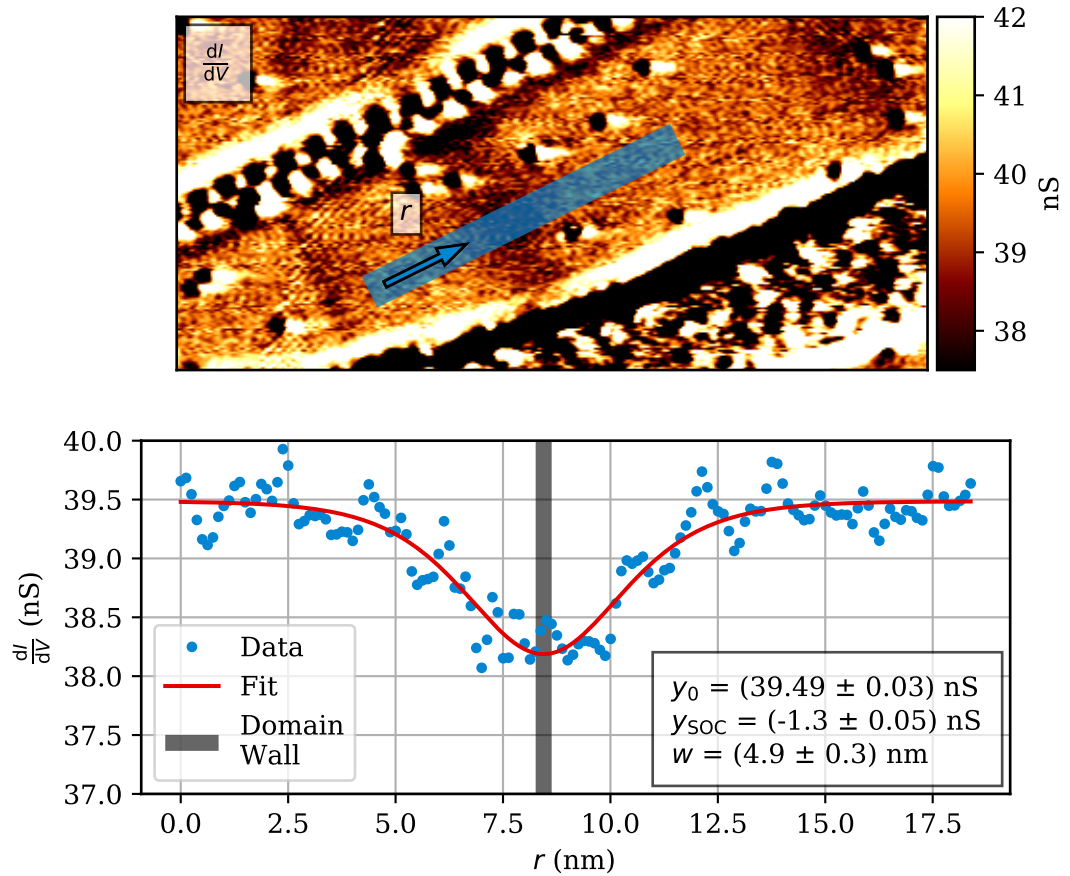


Figure 3.8: (Top) Closer image of a domain wall, taken from the $\frac{dI}{dV}$ channel of the reference image in Figure 3.7. A line profile over the domain wall is indicated by the blue box, with the box width corresponding to the perpendicular averaging width of the profile, and with the profile direction r indicated by the arrow. (Bottom) Fit of the TAMR contrast model (red) from Equation (3.1) to the profile data (blue).

large range of widths has been reported, from 6 nm to 9 nm, and the width can vary with temperature [69].

Having verified the imaging contrast with a non-magnetic tip, SP-STM imaging with a spin-sensitive bulk Cr tip can now be discussed. A representative image is shown in Figure 3.9. The bias potential was chosen based on literature values for energies with significant spin polarization.

The major topographical features appear again with this tip, including the step edges and dislocation lines. In addition, as predicted, a strong alternating domain pattern is observed. The DL has an out-of-plane magnetization, while the ML will have an in-plane magnetization, due to spin-orbit coupling with the W substrate. As the magnetic contrast depends on the projection of the tip magnetic moment onto the surface magnetization, Θ , there will be tip states that reveal magnetic contrast in only the DL or the ML. It can also occur that contrast will be exhibited in both areas simultaneously, in the case of the tip magnetization having both in-plane and out-of-plane components.

The Curie temperature is known from literature, and the STM temperature was chosen to be below this [70]. Depending on the tip configuration, the magnetic structure can appear in either or both the topographic channel and the $\frac{dI}{dV}$ channel. The sources of these two contrasts are related. In both cases the change in Θ modulates the tunneling conductance. However, the Z channel is sensitive to the total conductance, which is the energy integrated differential conductance $\frac{dI}{dV}$. Even if in principle spin contrast should always be present in both channels (assuming no energy regions with negative $\frac{dI}{dV}$), experimental noise limits its detection.

Qualitatively, if the spin polarization of the current is sufficiently large, the change in conductance will require a change in tip height to maintain a constant current, thus translating a change in Θ into a height change in topography. However, at the fixed bias voltage of the scan $\frac{dI}{dV}$, which varies with energy, might be quite small. The inverse can occur as well, since the lock-in technique used to measure $\frac{dI}{dV}$ has a large signal-to-noise ratio with a small bandwidth, and may thus return a spin-sensitive signal, even though the total conductance did not change sufficiently to be observed in the topographic channel.

As expected, magnetic domains and domain walls can be seen in Figure 3.9. We note here that without an external magnetic field to fix the magnetization of the STM tip, it cannot be determined if a bright (or dark) domain in the $\frac{dI}{dV}$ map corresponds to a magnetization oriented into or out of the sample. Thus we will refer to them as bright and dark domains.

There are now two sources of contrast that lead to their structure [63, 67]: spin-valve behaviour and the TAMR effect. These two effects have

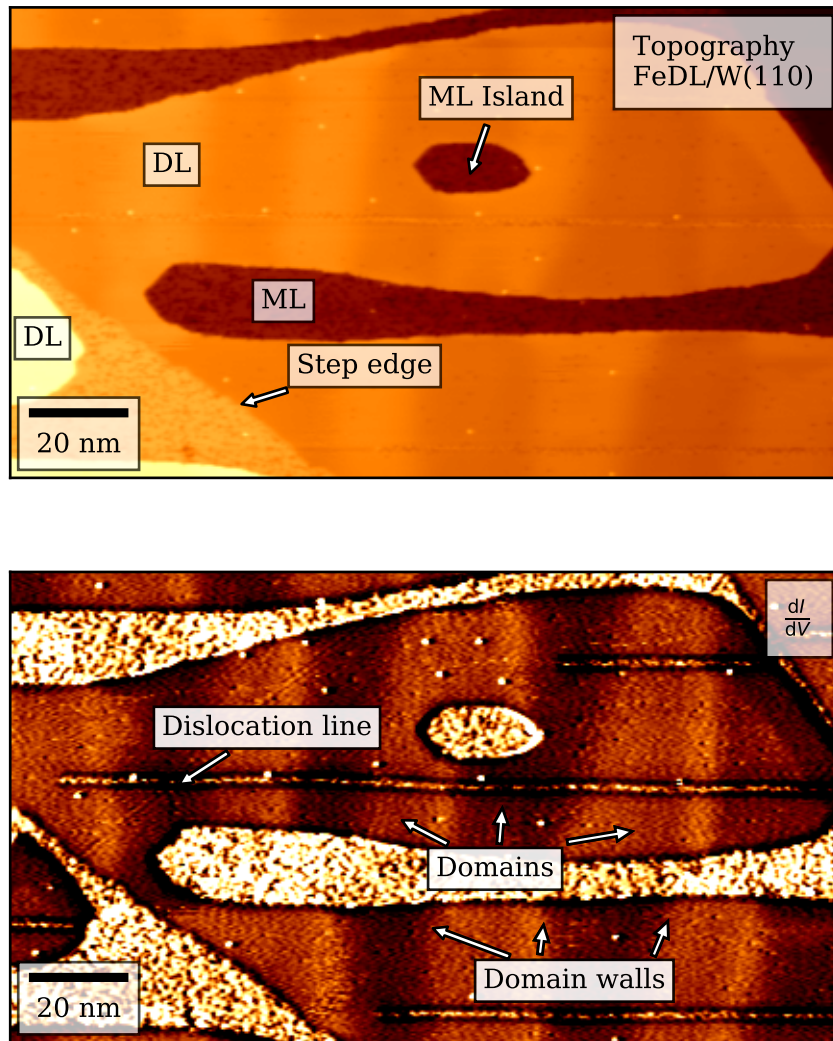


Figure 3.9: Topographic and spin-resolved differential conductance image of the Fe DL on W(110), imaged using a Cr tip, with $V = 250$ mV, $I_{\text{set}} = 1$ nA, and $T_{\text{STM}} = 50$ K. $\frac{dI}{dV}$ was measured at 4.3 kHz, with a modulation amplitude of 40 mV. An alternating magnetic domain structure is indicated.

been shown to sum together to explain the observed lateral contrast when transitioning between domains. The combined model has the form

$$\sigma(r) = y_0 + y_{\text{SP}} \cos(\Theta) + y_{\text{SOC}} \sin^2(\theta_{\text{sample}}) , \quad (3.8)$$

where again, $\Theta = \theta_{\text{tip}} - \theta_{\text{sample}}$, with the tip magnetization assumed to have no dependence on x , and the sample magnetization θ_{sample} has the form previously defined in Equation (3.2).

To verify this model, we again consider a line profile from the $\frac{dI}{dV}$ channel of the image in Figure 3.9, where the profile now spans two domain walls, transitioning from a dark domain to a bright domain, and back again. The profile, and the resulting fit from applying Equation (3.8) and Equation (3.6) are shown in Figure 3.10.

Again, it can be seen that the model describes the lateral data well. From the fit, we can determine values of $\theta_{\text{tip}} = 50^\circ \pm 3^\circ$, and $\lambda = 5.5 \text{ nm} \pm 0.3 \text{ nm}$, which is reasonable compared to literature values. Using the previous definition of S from Equation (3.7), we have $S_{\text{SOC}} = 4\%$ and $S_{\text{SP}} = 13\%$. These values will be used later for comparison.

With the previous results, we can conclude that the Fe DL samples that were produced have the same quality and characteristics as previous work, allowing for direct comparison of results in the later analysis.

Fe ML/DL on Ir(111)

The second sample system used in this work was the Fe ML and DL on the Ir(111) substrate. This surface is of note for its non-collinear spin textures at low temperatures $< 26 \text{ K}$ [71]. At these temperatures, the spins on the ML form a nano-skyrmion lattice, with a periodicity of approximately 1 nm. For the purposes of this work, this system serves as a benchmark test for lateral resolution of the detection of magneto-Seebeck tunneling effects. Thus, rather than a detailed fitting of lateral profiles, our primary interest is the correlation of the nano-skyrmion lattice to any observed magneto-Seebeck signal.

The substrate was prepared by sputtering with Ar gas, followed by flashing at 1200°C . The Fe DL was then deposited on the, still-warm, clean surface, again via an e-beam evaporator. This resulted in continuous ML and DL areas, as seen in Figure 3.11.

In this constant-current SP-STM image, both the ML and DL Fe areas are visible in the top overview image. From literature, it is known that the ML grows pseudomorphically [72]. In the zoomed image of the ML, the expected square nanoskyrmion lattice is clearly visible, in accordance with literature results [71].

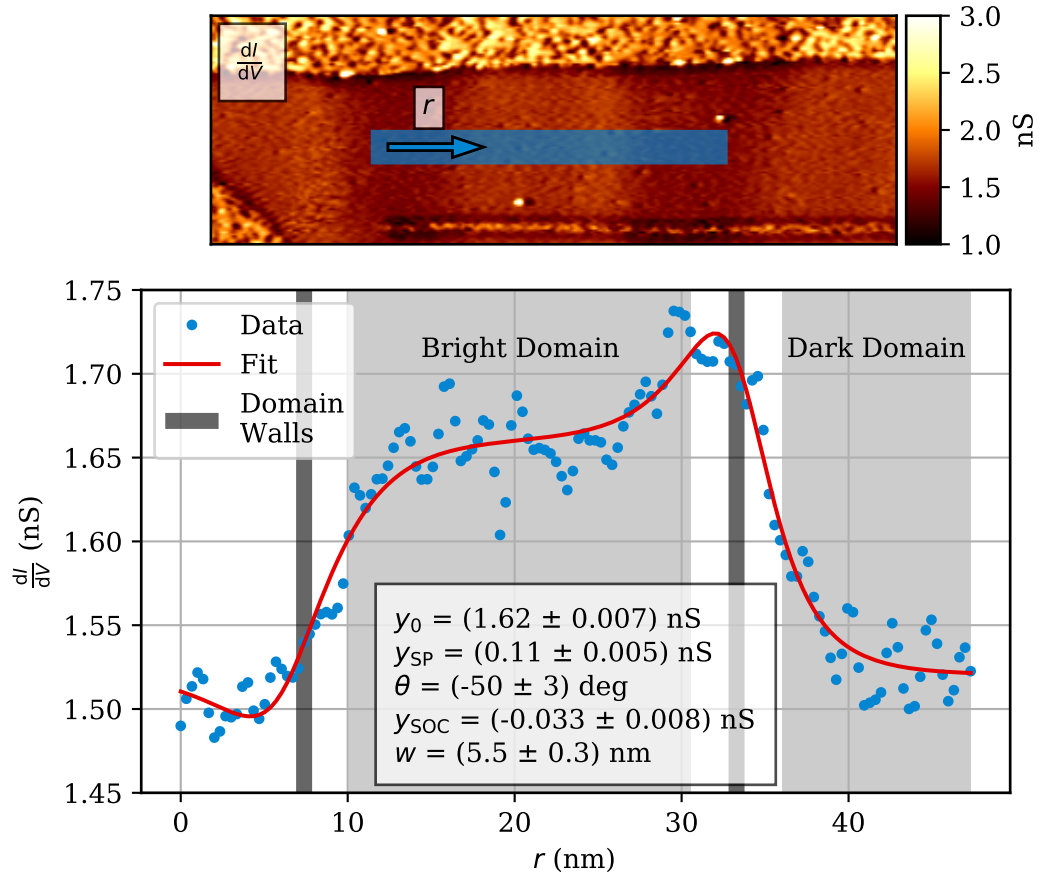


Figure 3.10: (Top) Line profile indicated in blue, perpendicular to two domain walls, proceeding from a dark domain, to a bright domain, to a dark domain. The data is taken from the $\frac{dI}{dV}$ channel of the image in Figure 3.9. (Bottom) Line profile (blue) fitted with the model of spin and TAMR contrast (red) from Equation (3.8). The fitted domain wall positions are shown (dark grey). The gap between the indicated domains is equal to the fitted wall width.

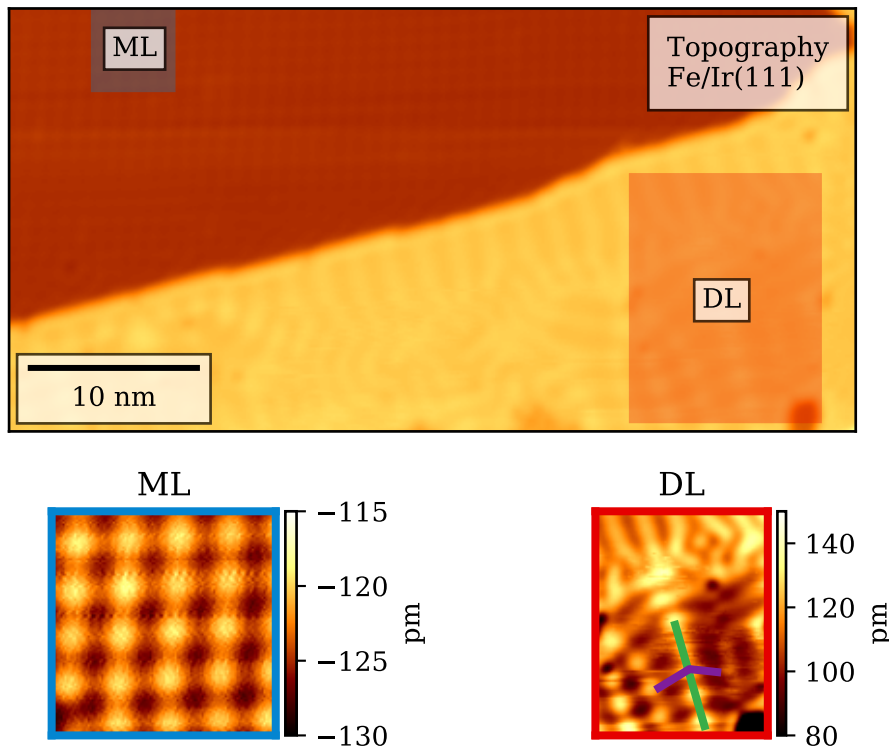


Figure 3.11: (Top) Spin-resolved constant-current image of the Fe ML and DL on Ir(111), imaged using a Cr tip, with $V = 250$ mV, $I_{\text{set}} = 1$ nA, and $T_{\text{STM}} = 25.37$ K. $\frac{dI}{dV}$ was measured at 4 kHz, with a modulation amplitude of 50 mV. (Bottom left) Cropped image of the Fe ML, exhibiting the square nanoskyrmion lattice, with a periodicity of approximately 1 nm. (Bottom right) Cropped image of the Fe DL, showing the dislocation line (green), and the spin spiral wave front (purple).

The DL can exhibit two growth modes; pseudomorphic or relaxed. In this image, the second phase is evident, resulting in dislocation lines for stress relief. The bottom left image highlights this structure, with the green line marking the location of a dislocation line. Previous SP-STM studies [73] have determined that a spin spiral state is present, with a zig-zag wavefront (contour of magnetization) that changes direction at the dislocation lines. This is marked by the purple line.

As can be seen, the expected structural and magnetic features are present in our samples of Fe on Ir(111). Thus, the system can be prepared with sufficient quality to suit its use as a test of lateral magnetic resolution, using the nanoskymion lattice on the Fe ML.

3.2 Thermal system of the STM

Having established the instrumentation and sample systems to be used, the next step is the creation and measurement of a well-defined temperature gradient between the STM tip and the sample. In this section, the equilibrium situation of tip and sample at the same temperature will first be analyzed. With the resulting understanding of the thermal fluxes and conductivities present in the system, we can discuss the application of heating power via an externally mounted laser, and the resulting development of a temperature gradient between the tip and the sample. This includes both the experimental approach, and the measurement of the resulting ΔT , which is required for the eventual determination of S .

3.2.1 Description of thermal elements

To start, the thermal elements of the system and their connections must be defined. The basic components consist of the UHV chamber at room temperature, the heat shield, the STM body, the sample, the tip, and the heat exchanger of the cryostat. These are variously connected via both radiative and thermal diffusion based channels, that are depicted schematically in Figure 3.12.

The heat shield (HS) is radiatively coupled to the external environment of the UHV chamber walls over its entire surface, except for the bottom face, and internally to the STM, sample, and tip. It is connected mechanically to the underlying damping stage via three ruby ball spacers, but since the damping stage is only loosely connected to the UHV chamber, we will ignore this connection. Internally, the heat shield is connected via a system of ruby ball spacers, steel rods, and steel plates to the internally hanging STM. In

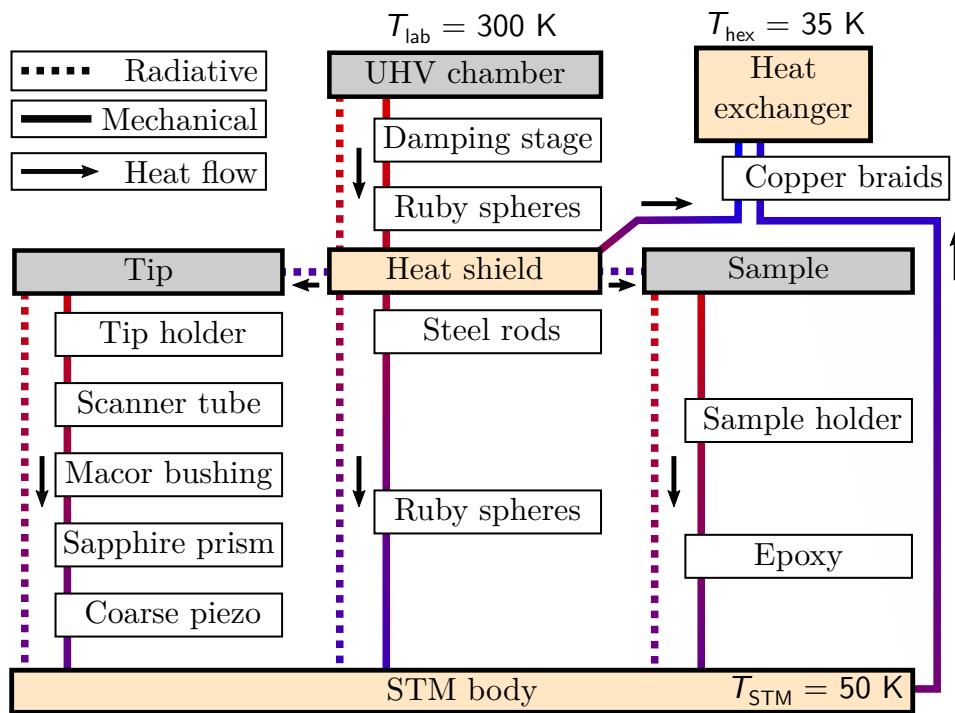


Figure 3.12: Macroscopic thermal system of the STM, with the major sources of thermal conductivity between the elements. For modeling purposes the elements in white boxes will be combined into a single thermal conductance connecting the other elements in the colored boxes, which will be assumed have to a well defined, uniform temperature. The connection between the tip and the sample will be discussed in more detail separately.

addition, a 20 cm long copper braid consisting of 800 strands, each with a diameter of 50 μm , provide a connection to the heat exchanger exhaust gas shield, which is cooled by the cryogen after it has passed the connection point for the STM cooling.

The STM body is coupled to the heat shield via radiative heat transfer and by mechanical mounting to the heat shield, with cooling power provided by a second copper braid, identical to the one for the heat shield, connected to the heat exchanger. The temperature of the body is directly measured via a thermal diode, which provides a reference point for modelling the equilibrium temperatures.

The sample is in good thermal contact with the STM body via binding to the sample plate, which is clamped into the sample receptacle. This receptacle is glued with strongly thermally conducting epoxy to the body. The front opening in the STM will allow some radiative coupling to the heat shield, but the majority of thermal radiation will come from the internal cavity of the STM. For an equilibrium situation with no temperature gradient, we expect no net radiative transfer between the tip and sample, but this will change if a significant temperature gradient is present.

The thermal connection between the tip and tip holder, and the STM body is considerably more complex, as shown in Figure 3.12. Starting from the tip, there is the metallic tip holder, a macor mounting piece, the piezo scanner tube, a second macor bushing, the sapphire prism, and the six coarse drive piezo stacks. All these elements will combine into a considerable thermal resistance between the tip and STM body. This makes the tip a much more suitable candidate for temperature modification than the sample, as the required heating power will be much less for a given temperature change, minimizing additional effects from the heating approach. The radiative coupling is essentially the same as that for the sample, consisting of a small view to the heat shield, and the dominant source of thermal radiation being the internal STM body cavity.

There is also wiring into the STM to consider, for sample biasing and tip current sensing, as well as for the piezo elements. The tip and sample are connected to feedthroughs on the heat shield via thin manganin wires. However, while these would be considerable heat sources at e.g. <1 K temperatures, for our experiments they will be a negligible heat source, and can be considered for modelling purposes as perturbative only.

3.2.2 Equilibrium tip temperature modeling

For determining S , the starting equilibrium temperature of tip and sample, before any additional heating is applied, must be known. As stated in the

previous section, the sample temperature is assumed to be equal to that of the temperature of the STM body, which is measured nearby. However the tip is much more insulated from the body by intervening components, but is still subject to ambient radiation both from the STM body and from the heat shield, which is presumably at a higher temperature. As the absolute tip temperature is not directly measured, we will develop a model here for estimating the equilibrium tip temperature T_{tip} , given these thermal couplings. This will provide an order of magnitude estimate of the expected temperatures and thermal fluxes in the system, which will be used as a reference for discussion of the later temperature difference modeling.

We are thus interested in three temperatures; the tip temperature T_{tip} , the STM temperature T_{STM} , and the heat shield temperature T_{HS} . Referring to Figure 3.12, we will consider $T_{\text{sample}} = T_{\text{STM}}$, T_{hex} and T_{UHV} to be constant, and consider the thermal connections as labeled in the figure. For simplicity, the elements will be assumed to be homogeneous, and at a single temperature.

For each element, the time-dependent change in temperature will depend on the heat capacity C and the change in internal energy U :

$$\frac{dT}{dt} = \frac{1}{C} \frac{dU}{dt} , \quad (3.9)$$

where $\frac{dU}{dt}$ is the sum of the heat fluxes into and out of the element and the work done by the element. The system as we consider it will be closed, and have no work performed on or by it. Thus, the only change in U for each element can come from heat transfer between the thermal elements and the environment. As no large electrical currents or magnetic fields are present, we need only consider radiative and diffusive heat sources:

$$\left(\frac{dU}{dt} \right)_i = \sum_{j \neq i} (q_{\text{rad}(i-j)} + q_{\text{diff}(i-j)}) . \quad (3.10)$$

Here the net change in internal energy for element i is the sum of the net radiative power transfer between i and j , $q_{\text{rad}(i-j)}$, and the net heat flux between them, $q_{\text{diff}(i-j)}$, for every element j in the system.

The heat capacity is only important for the thermal dynamics, as for an equilibrium situation, where $\frac{dT}{dt} = 0$, Equation (3.9) reduces to

$$\frac{dU}{dt} = 0 . \quad (3.11)$$

Given the condition of Equation (3.11), the simultaneous solution of Equation (3.10) for every element of the system will give the set of equilibrium temperatures.

For a quantitative analysis then, the task is to define $q_{\text{rad}(i-j)}$ and $q_{\text{diff}(i-j)}$ for each pair of elements. For many pairings, given the choice of how to divide the system into separate elements, it is immediately apparent that these values are zero (e.g. the STM body is not in mechanical contact to the UHV chamber, but rather to the heat shield). Thus we will only discuss the non-zero values.

Thermal conductance

The thermal conductance of $q_{\text{diff}(i-j)}$ will be modeled using Fourier's Law [74], which is sufficient for macroscopic heat flux analysis. In discrete form, this law can be stated as

$$q_{\text{diff}(i-j)} = -k_{i-j} (T_i - T_j) , \quad (3.12)$$

where the thermal conductance k_{i-j} between the elements is a function of their mechanical connection. This consists of both contact thermal resistance at interfaces, and heat conduction through any intervening elements:

$$k_{A-B}^{-1} = \sum_{i-j} k_{i-j}^{-1} , \quad (3.13)$$

where the sum is over the thermal conductances across all of the intervening elements, and the thermal contact conductances. In this case the intervening elements are treated as thermal conductors only, ignoring any heat sources or sinks, or radiative coupling. This is sufficiently accurate if the parts are small, relative to the main elements.

Thermal radiation

For the radiative power transfer, as we initially have no directed light sources, we are considering only the ambient thermal radiation of the various surfaces, assuming macroscopic separations. The surface of every element in the system is simultaneously absorbing incident radiation and emitting both its own thermal radiation and reflections of any incident radiation. If we assume gray, diffusively emitting surfaces we can define the net heat flux through a surface, due to radiation, as [75]:

$$q_{\text{rad}} = \epsilon E_b - \alpha H , \quad (3.14)$$

The emittance of the surface ϵ , which is the ratio between the emitted radiation and that of an ideal blackbody, is a surface and material specific

constant. This will come from knowledge of the utilized materials and surfaces (e.g. polished vs. unpolished). This also applies to α , which is the absorptance of the surface. H is the net incident radiation on the surface. E_b is the ideal blackbody radiation, defined in the Stefan-Boltzmann Law as

$$E_b = \sigma_B T^4, \quad (3.15)$$

where the surface is at temperature T , and $\sigma_B = 56.70 \text{ nW/m}^2\text{K}^4$ is the Stefan-Boltzmann constant.

The flux H contains the incident radiation from the other surfaces, H_{inc} , as well as any external sources of radiation H_{ext} . Each surface in the system is assumed to diffusely emit thermal radiation, defined by the radiosity J :

$$J = \epsilon E_b + (1 - \alpha) H. \quad (3.16)$$

If we consider a single surface i , only some fraction of J from the other surfaces will be absorbed by i . We thus define the view factor F_{j-i} , which is the fraction of the total diffuse radiation from element j that is incident on element i . It is a purely geometric factor related to the relative position, shape, and orientations of the considered surfaces.

In its most general form, solving for H_{inc} involves integration over both the emitting surfaces and the receiving surface, with view factors varying by both positions. However, a more practical approach is to divide the enclosing emitting surfaces into a set of N subsurfaces. If these are chosen such that they can be assumed to be homogeneous, both in J and in F_{i-N} , then the integration can be avoided. This results in a discrete form of H for surface i :

$$H_i = \sum_{j=1}^N J_j F_{i-j} + H_{\text{ext}-i} \quad (3.17)$$

with the total flux on surface i , H_i , being the sum of the radiosity J_j of every surface (including i itself), modulated by the view factor from i to j , F_{i-j} , with the final addition of the external flux $H_{\text{ext}-i}$ [75].

The substitution of Equations (3.15) to (3.17) into Equation (3.14) gives the result

$$\frac{q_i}{\epsilon_i} - \sum_{j=1}^N \left(\frac{1}{\epsilon_j} - 1 \right) F_{i-j} q_j + H_{\text{ext}-i} = \sum_{j=1}^N F_{i-j} (E_{b_i} - E_{b_j}). \quad (3.18)$$

Here the sum is over all surfaces, including i . Equation (3.18) contains both the heat flux through surface i , and the temperature of the surface, via

E_{bi} . Given the determination of F for each pair of surfaces, this relation can be combined with Equation (3.12) for calculating the net heat change in the thermal elements.

Combined model

The above relations describe a general approach to modeling the equilibrium temperature of a connected system of thermal elements. We will use this both for an estimate of the entire STM system, with no heating power and a closed heat shield door, and later for the case of applied heating power.

To combine the above relations into a single model, we reformulate Equations (3.12) and (3.18) into vector form. For the radiative heat flux,

$$\mathbf{q}_{\text{rad}} = \mathbf{C}^{-1} \cdot [\mathbf{A} \cdot \mathbf{e}_b - \mathbf{h}_0] , \quad (3.19)$$

where \mathbf{q}_{rad} , \mathbf{e}_b , and \mathbf{h}_0 are the radiative heat flux, blackbody radiation, and external radiation of the thermal elements, and the matrices \mathbf{C} and \mathbf{A} are defined as

$$C_{ij} = \frac{\delta_{ij}}{\epsilon_j} - \left(\frac{1}{\epsilon_j} - 1 \right) F_{i-j} , \quad (3.20)$$

and

$$A_{ij} = \delta_{ij} - F_{i-j} . \quad (3.21)$$

Here δ_{ij} is the Kronecker delta function. For the thermal conductance, we have

$$\mathbf{q}_{\text{diff}} = \mathbf{K} \cdot \mathbf{T} - \mathbf{b} , \quad (3.22)$$

where

$$K_{ij} = (1 - \delta_{ij}) k_{j-i} - \delta_{ij} \sum_j k_{i-j} , \quad (3.23)$$

and $k_{i-j} = k_{j-i}$.

The matrix \mathbf{K} defines the thermal conductance between the elements of the system. The vector \mathbf{b} has the form

$$b_i = - \sum_l k_{i-l} T_l , \quad (3.24)$$

and defines the heat exchange of the elements with fixed external heat baths; e.g. the heat exchanger and the UHV chamber.

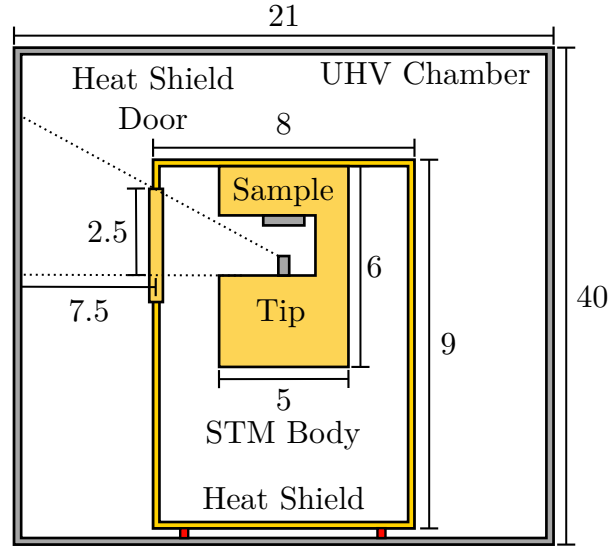


Figure 3.13: Sketched geometries of the thermal elements, with relevant dimensions labeled.

Thus we have, in vector form, the full definition of the heat fluxes of the system:

$$\mathbf{q} = \mathbf{q}_{\text{diff}} + \mathbf{q}_{\text{rad}} = \mathbf{K} \cdot \mathbf{T} - \mathbf{b} + \mathbf{C}^{-1} \cdot [\mathbf{A} \cdot \mathbf{e}_b - \mathbf{h}_0] . \quad (3.25)$$

The solution of Equation (3.25) for $\mathbf{q} = 0$, will yield the equilibrium temperatures of the system.

Thermal model of heat shield, STM, and tip

As has been labeled in Figure 3.12, the later measurements were all performed at an STM temperature of 50 K, which required a heat exchanger temperature of $T_{\text{hex}} = 35$ K. This heat exchanger temperature, and the room temperature of $T_{\text{env}} = 300$ K, will be taken as constants in the analysis.

The geometry we use to approximate the system is shown in Figure 3.13. For simplicity, cylindrical and planar approximations of the elements have been used.

Catalogues of view factors, solved for various elemental geometries, are available in literature [75]. These have been used, along with the known and labeled dimensions of the system, to calculate F for each coupling. These are summarized in Table 3.1. Additional details regarding the calculation of these factors can be found in Appendix A.

The emissivities of the surfaces can also be found in literature. The UHV chamber consists of unpolished stainless steel, the heat shield and STM

Elements (A-B)	F_{i-j}	F_{j-i}
Env-Heat Shield	0.05	0.5
Heat Shield-STM Body	0.27	1
Heat Shield-Tip	0.002	0.16
STM Body-Tip	0.002	0.84

Table 3.1: View-factors and areas.

body have polished gold surfaces, and the sample and tip are dependent on the experiment. The emissivities of the necessary elements are tabulated in Table 3.2. The values for the steel are for room temperature, while the others are taken at temperatures to approximately match the known conditions; 50 K for the STM and 150 K for the heat shield.

Material	ϵ
W	0.4 [76]
Unpolished steel	0.7 [75]
Polished gold (150 K)	0.01 [75]
Polished gold (50 K)	0.002 [75]

Table 3.2: Emissivities of elements used in the thermal model. The temperature dependence of emissivities of metals means that at 150 K it will be approximately halved relative to room temperature [77].

The thermal conductance between the elements of the system was calculated, using the materials and geometries from the previous section, giving the values in Table 3.3. The calculations and assumptions are discussed in more detail in Appendix A. The resulting thermal conductances between the components of the system are in the range of 100 $\mu\text{W K}^{-1}$ to 1 mW K^{-1} .

	k ($\mu\text{W K}^{-1}$)
Heat Shield-STM Body (150 K)	133
STM Body-Tip (50 K)	848
Heat Shield-Heat Exchanger (35 K)	2300
STM Body-Heat Exchanger (35 K)	2300

Table 3.3: Estimated thermal conductances between elements of the system. The thermal conductivities used for calculation were taken at the temperatures indicated.

Using the values from Tables 3.1 and 3.2, Equation (3.25) was solved numerically, using the SymPy [78], SciPy, and NumPy modules for the Python

programming language [79].

The goal of the modeling was to set the overall scale of expected heat fluxes and temperatures in the system, and more importantly their sensitivity to the system parameters. For this idealized element modeling approach, fixed temperature reference points provide a useful check on the quality of the model. Both an unconstrained and constrained non-linear solver were used. The constrained solver used the condition of $T_{\text{STM}} = 50 \text{ K}$. As this was directly measured in the experiments, this is taken as the more accurate solution, with a large divergence between the solvers taken as a sign of numerical instability of a solution.

Overall, the model was capable of reproducing the expected temperatures. Experimenting with the input parameters revealed a broad dependence of the final temperatures on the ratio between the radiative heating and conductive cooling components, as expected. It was found to be necessary to increase the conductance to the heat exchanger by a factor of two to match the reference temperature of the STM. This seemed reasonable as the emissivities of simple surfaces not subject to oxidation, especially gold-coated ones, should be quite comparable to literature. In practice, the resulting temperatures were quite sensitive to the input system parameters. Thus, we will extract some broad conclusions from this model.

With this taken into consideration, the constrained model estimated that $T_{\text{HS}} = 152 \text{ K}$, $T_{\text{STM}} = 50 \text{ K}$, and $T_{\text{Tip}} = 50.1 \text{ K}$. However, the unconstrained solver returned $T_{\text{HS}} = 152 \text{ K}$, $T_{\text{STM}} = 50 \text{ K}$, and $T_{\text{Tip}} = 54 \text{ K}$. From this, we conclude that a temperature difference of a few Kelvin between tip and sample, even in equilibrium, is plausible.

The influence of the opening of the heat shield door on the tip could be evaluated by adjusting the view factors between environment and tip, and heat shield and tip, accordingly. Effectively, opening the door resulted in a change in tip temperature ranging from 50 mK, for the unconstrained solver, to 1.8 K, for the constrained solver.

Finally, an application of 1 mW of external irradiation to the tip results in an increase of T_{Tip} in a range from 100 mK, for the unconstrained solver, to 4 K, for the constrained solver. These values depended sensitively on the emissivity of the tip and the thermal conductance to the STM body, as expected. This sets the range of expected heating, if external radiation is applied to the tip, as will be discussed in the following sections.

3.2.3 Implementation of tip heating via laser

With the previous understanding of the thermal conductivities in the system, the creation of a temperature gradient can be discussed. Tunneling Seebeck

coefficients from the literature are on the order of $10 \mu\text{V K}^{-1}$ [22]. For more robust measurements that are simple to distinguish from noise, relative signals on the order of $100 \mu\text{V}$ or more would be preferable. This implies a temperature gradient of a few degrees Kelvin at a minimum is desired. However it should also not be too large, as at this point the linear approximations outlined in Section 2.2 will become less applicable, once again complicating interpretation.

Given the relative thermal isolation of the tip from the STM body compared to the sample, we will heat the tip in order to create ΔT . The small conductivity means both that less heating power will be required for a given ΔT , and that the tip temperature will be slower to react to drifts in the STM body temperature, effectively filtering out higher frequency variations.

Ideally we would like to be able to both heat and cool the tip relative to the sample within the same experiment, but this is not possible with the current apparatus, and will be left for future work. There are a variety of possible approaches to heating the tip, including resistive heating elements, thermal bridges, or radiative power transfer. These will be discussed in turn.

A resistive element, simply consisting of an electrically resistive element located near the tip, has the disadvantage of requiring additional modification of the STM, and introducing an additional potential source for electrical noise into the system. The relative heating efficiency will also be quite low, since it would need to be electrically well-isolated from the tip, both by distance and insulating elements, implying a corresponding thermal isolation.

A thermal bridge, consisting of a mechanical connection between the tip or tip holder and a warmer area of the system is also impractical without extensive modifications, and would be much more difficult to smoothly adjust the applied heating power. Also, given the difficult nature of exactly determining temperatures, as seen in the previous section, this approach would lack the required accuracy and repeatability necessary for reliable measurements.

A hybrid of the two approaches could be considered for future work. A heating element could be mounted relatively far away from the tip and sample, with an electrically-insulating wire connecting it to the tip holder region. Much higher heating powers could then be applied to the element without concern for electrical interference. However the implementation details would also be complex.

For this work, the third approach of radiative heat transfer was chosen. In contrast to the discussion in Section 3.2 of passive blackbody radiation, a focused laser beam was used to deliver heating power directly to the tip holder, through the open door of the STM. This solution is superior to the other approaches due to the lack of modifications to the STM, the avoidance

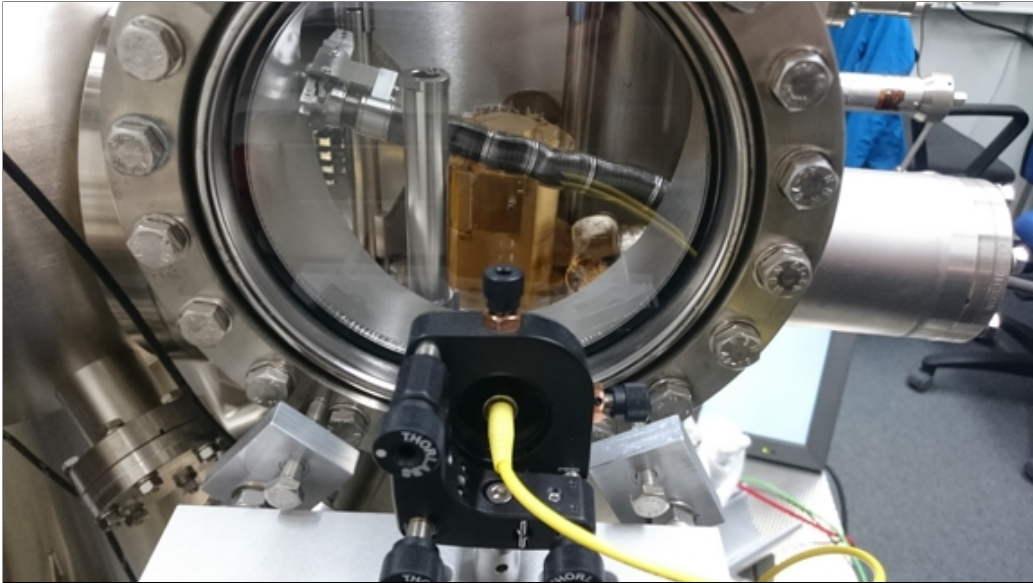


Figure 3.14: Mounting of the optical fiber for the laser to the output collimator.

of any additional electrical input into the system, and the precision with which the heating power can be adjusted. The tip holder was chosen for heating to avoid any photoassisted tunneling effects [80].

An image of the utilized setup is shown in Figure 3.14. A fiber coupled S1FC660 Fabry-Perot benchtop diode laser, supplied by ThorLabs, was used, with a wavelength of 659 nm. The output power was adjustable, in increments of 10 μ W, from 0 mW to the maximum output power of 15 mW. The manufacturer specified error for the power output was 10%. This laser was connected, via a multi-mode optical fibre, to an adjustable collimator mounted inside of a 5-axis stage as shown in the figure. This allowed for precise adjustments of the laser spot within the STM.

For operation, with the door open, the tip is approached to within tunneling distance of the sample, then retracted a few hundred nanometers. The laser, set to minimum power, is turned on, and the laser spot adjusted to shine on the tip holder. The indent in the tip holder, necessary for the tip exchange mechanism, should effectively increase the absorptance of the holder via multiple reflections. The collimator was adjusted such that the beam had a minimum spot size at the tip holder. After this, the laser can be turned off, and STM operation continued as normal, with the door open in preparation for later heating.

3.2.4 Measurement of temperature difference

With the approach to creating ΔT decided, a method is needed to measure it. Previous work measuring thermopower with STM lacked a detailed analysis of the temperature gradient, relying either on binary heating/no-heating approaches or scaling of thermopower with applied heating power [19, 81, 32]. However, an accurate determination of ΔT is crucial for acquiring a reasonable measurement of the Seebeck coefficient. We have therefore undertaken a more detailed analysis to obtain this [82]. This modeling was performed as part of the Master thesis of Hermann Osterhage, which was supervised in the context of this work [83], and further discussion can also be found there.

Following from Section 3.2.3, we will assume the sample temperature to be fixed at the temperature of the STM ($T_{\text{sample}} = T_{\text{STM}}$), meaning only a measurement of the relative change of T_{tip} is required. In principle, the signal used to measure the temperature should originate as close as possible to the tunneling junction. A thermal diode or thermistor placed close to the tip requires electronic leads for measurement, providing an additional pathway for heat into the STM. In addition, the accuracy of the measurement would in general be low, due to unknown thermal conductivities between the sensor and the STM elements.

A more accurate approach is the measurement of a temperature dependent property of the tip itself. Many properties of solid materials are strongly dependent on the temperature, but the optimal choice is one that is already measured with high accuracy in the context of STM measurements. Thus, we have used the thermal expansion of the tip and tip holder as a function of applied laser heating power as a thermometer. As the tip position is controlled via the piezo scanner tube with an accuracy of picometers, this results in a sensitive signal for the temperature. To demonstrate this technique, an expansion dataset will be analyzed in detail in the following.

Experimentally, the tip is brought into tunneling contact with the sample, with no applied laser power. Once in equilibrium, the laser power is then switched on, with the tip piezo feedback loop still closed. As described previously, the tip holder rather than the tip is the target of the laser, but it has been found that the temperature of the tip will essentially match that of the tip holder while heating [83].

The tip and tip holder will begin to expand as the temperature rises, bringing the tip closer to the sample. As the bias voltage remains fixed, the tunneling current will rise, and the feedback loop will retract the scanner tube in response. Although a thermal tunneling current will already be present, the use of a bias voltage of at least some mV means that the dominant tunneling will be due to this applied bias.

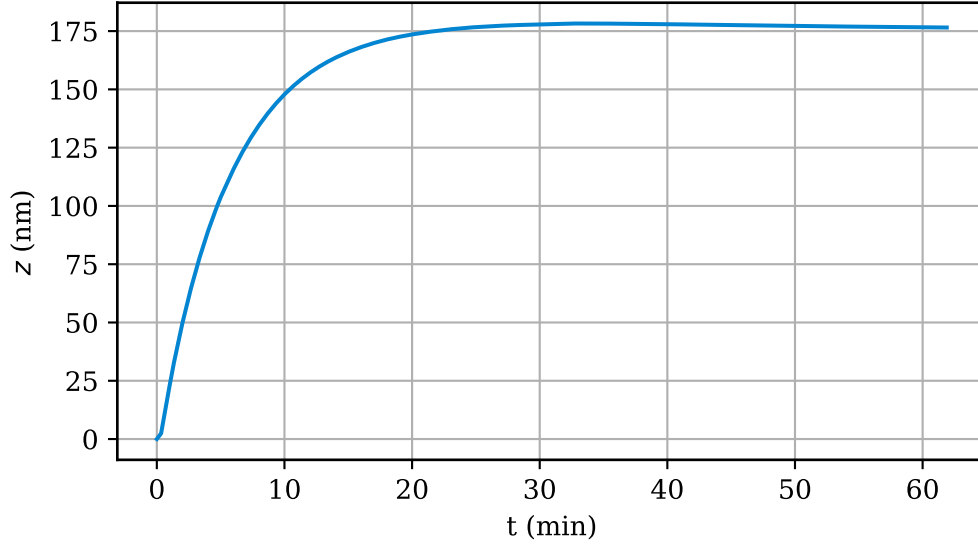


Figure 3.15: Tip position normal to the surface as a function of time. The tip was made from W, at a starting temperature of 50 K. Prior to $t = 0$ the tip was in equilibrium, with $V = 250$ mV and $I_{\text{set}} = 100$ pA, and the drift rate in z was minimal. The applied laser power was then changed from 0 mW to 1.66 mW. The maximum expansion was 178 nm.

As long as the feedback loop is fast enough relative to the thermal expansion, tunneling contact will be maintained. The tip position normal to the sample is then recorded over time, until the tip position reaches a new equilibrium, giving data such as that shown in Figure 3.15.

The data shown was collected with a W tip, starting at a base temperature of 50 K. As per the procedure, the laser power was set to 1.66 mW while remaining in tunneling contact. To understand this curve, we first consider the change in equilibrium tip extension. In general, materials will change size in response to temperature, with a relative change in length. This change, along a single axis and using a linear approximation, is described by

$$\alpha = \frac{1}{L} \frac{dL}{dT}, \quad (3.26)$$

or, assuming a constant α , which is appropriate for small changes in temperature,

$$\Delta L = \alpha L_0 \Delta T. \quad (3.27)$$

The thermal expansion coefficient α is material and temperature dependent, and the reference length L_0 is measured at a starting reference temperature (in our case with no laser power). We take this to be the difference between the starting position and the peak tip position, after approximately 30 min in Figure 3.15. Values for α for the materials used for the tips and tip holders are given in Table 3.4. These are assumed to be constant, as the expected temperature change is expected to be relatively small.

Material	$\alpha (T = 50 \text{ K}) \text{ K}^{-1}$
W	1.02×10^{-6} [84]
Cr	3.01×10^{-7} [85]
Steel	3.86×10^{-6} [86]
Molybdenum	1.04×10^{-6} [84]

Table 3.4: Thermal expansion coefficients for utilized materials.

In the simplest approach, Equation (3.26) is sufficient to estimate ΔT , given some estimation for L_0 . We will assume the tip and the tip holder to be at the same temperature. The lengths used will be the extent of the tip above the holder, and the height of the tip holder, as illustrated in Figure 3.16. The values can be measured directly, before inserting the tip into the UHV system.

Given the values in Table 3.4 and Figure 3.16, and the indicated expansion of 178 nm from Figure 3.15, we can calculate ΔT using Equation (3.26), applied to both elements separately. In this case, the combined expansion must equal the measured expansion:

$$\Delta L_{\text{total}} = \Delta L_{\text{tip}} + \Delta L_{\text{holder}} = (\alpha_{\text{tip}} L_{0\text{-tip}} + \alpha_{\text{holder}} L_{0\text{-holder}}) \Delta T \quad (3.28)$$

giving a value of $\Delta T = 15.7 \text{ K}$. This is an effective heating ratio of 9.4 K mW^{-1} . This is twice as large as that predicted in Section 3.2, but in the correctly predicted order of magnitude. A likely cause could be a larger thermal resistance between the tip holder and the tip receptacle, as the spring that fixes the holder is quite weak.

Additionally, when the tip holder is heated, there will be some temperature gradient created in the holder and the other thermal elements, each of which will also change length in response. Thus the determination of the effective L for the tip and tip holder is not trivial, even with measurements of the tip holder and tip lengths. To improve our approach, we incorporate additional measured quantities into our model, namely the time dependence

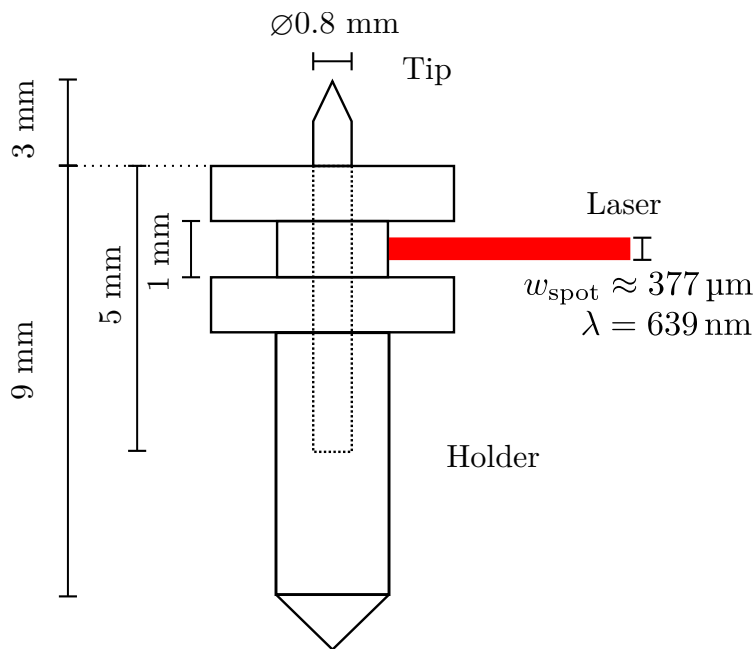


Figure 3.16: Sideview diagram of the tip and tip-holder, with marked lengths used for modeling the change in temperature. For the equilibrium calculation, a tip height of 3 mm and a tip holder height of 9 mm were used. The spot size was calculated from the specifications of the optical fibre and the collimator. Figure adapted from [83].

of the expansion. We can restate Equation (3.26) in a time-dependent form as

$$\frac{dL}{dt} = \alpha L \frac{dT}{dt} . \quad (3.29)$$

The change in temperature as a function of time depends on the balance of input power from the laser and heat lost to conductive cooling:

$$C \frac{dT}{dt} = AP_{\text{laser}} + k_{\text{Tip-STM}} (T_{\text{Tip}}(t) - T_{\text{STM}}) , \quad (3.30)$$

where C is the heat capacity of the tip/tip-holder system, A is the absorptance of the tip-holder surface at the wavelength of the laser, and $k_{\text{Tip-STM}}$ is the thermal conductance between the tip-holder and the STM body. The laser power P_{laser} we will take to mean the nominal output power set for the laser. Although this will have some error, we assume it to be systematic, resulting in an inconsequential shift in A .

For relatively small changes in T_{tip} , we can assume that α , C , A , and k are constant. However, they are still unknown, meaning that multi-variable optimization will be required to match this model to the measured curve. This is an advantage, as many data points were recorded during the expansion, as opposed to only two data points from the equilibrium measurement. The fitted temperature from this approach will thus be better constrained to the actual system.

Boundary conditions were used based on physical restrictions: A was bounded between 0 and 1 and per our previous discussion, the tip and tip holder were assumed to be at the same temperature.

As mentioned, the tip and tip holder will have different effective expansion lengths, and will in some cases be made of different materials with different values for α . Since these lengths are not precisely known, they should also be used as fitting parameters, albeit with boundaries set by the approximately known geometry.

We can however remove a fitting parameter, by noting that the heat capacity C can be calculated directly from the tip and tip holder lengths: $C = c_{\text{p}}V$, where c is the material dependent specific heat. This will be utilized for the fitting, with the added simplification of taking the base temperature of the tip for the value of c . As a check, we can also look at the retraction of the tip, after the laser power is turned off. In this case, the value for A has no effect, further reducing the parameter space. As can be seen, the retraction curves also match the measured data very well.

Thus, to perform the fitting, for each step of the fitting, the coefficients L_{tip} , L_{holder} , A , and $k_{\text{Tip-STM}}$, were chosen by a non-linear optimization algo-

rithm, and then used to solve Equation (3.30). The resulting $\frac{dT}{dt}$ can be used to calculate $\frac{dL}{dt}$, via Equation (3.29), to give a modeled expansion(retraction) curve. The resulted curve was then evaluated at the same time steps as the actual data, and the sum of the squares of the difference at each point was calculated. This was used as a fitness value for the optimization algorithm, which attempts to find a parameter set to minimize this value.

This was done for every tip used, with multiple expansion and retraction curves. To illustrate this, data taken with a bulk Cr tip attached to a steel tip holder, on the Fe DL on W(110), were fitted, with the result shown in Figure 3.17. At the marked points there is a break in the curve, as the laser power was held constant for some hours for scanning and spectroscopy to be performed. As can be seen, the model fits the behaviour very well. The equilibrium Z values are repeatedly well-matched at the same laser power, although some difference in expansion lengths can be noted. From the bottom plot of the modeled temperatures, this results in a variation of approximately ± 1 K. This variation was used as an estimate of the error in the final modeled temperatures.

The peak temperatures retrieved from the model are plotted against the applied laser power in Figure 3.18. A linear fit to the resulting data gives a final heating efficiency of 4.7 K mW^{-1} . This is very near the upper end of the range of heating efficiencies roughly estimated in Section 3.2. The linearity of the temperature with respect to the laser power was predicted in literature, where a Greens function method was used, with the assumption of uniform irradiance of a conical metal emitter [87].

Although the fitting results are well-matched to the data, it is still unclear if there are degeneracies in the system. This can lead to unphysical values from the fitting, despite a good match to data. For example, a higher laser absorptance will lead to a higher energy input into the system, which can be countered by a larger thermal conductivity. However, we can compare the fitted value for the thermal conductances to the calculated value in Section 3.2. The fitted model gives an average value of $k_{\text{Tip-STM}} = 109 \text{ } \mu\text{W K}^{-1}$, while the direct calculation results in $k_{\text{Tip-STM}} = 848 \text{ } \mu\text{W K}^{-1}$. While certainly different, these values are still on the same order of magnitude, meaning the fitted results are of the correct physical scale.

This procedure must be performed for every realignment of the laser, which will give different effective heating powers, and for every tip, necessitating the collection of expansion/retraction data with every dataset. For the same tip and sample, in subsequent experiments it is also sufficient to note only the maximum expansion/retraction as a function of the laser power, and calibrate this to a temperature using the fitting data from previous experiments. In this case the heating efficiency is recast in units of K nm^{-1} .

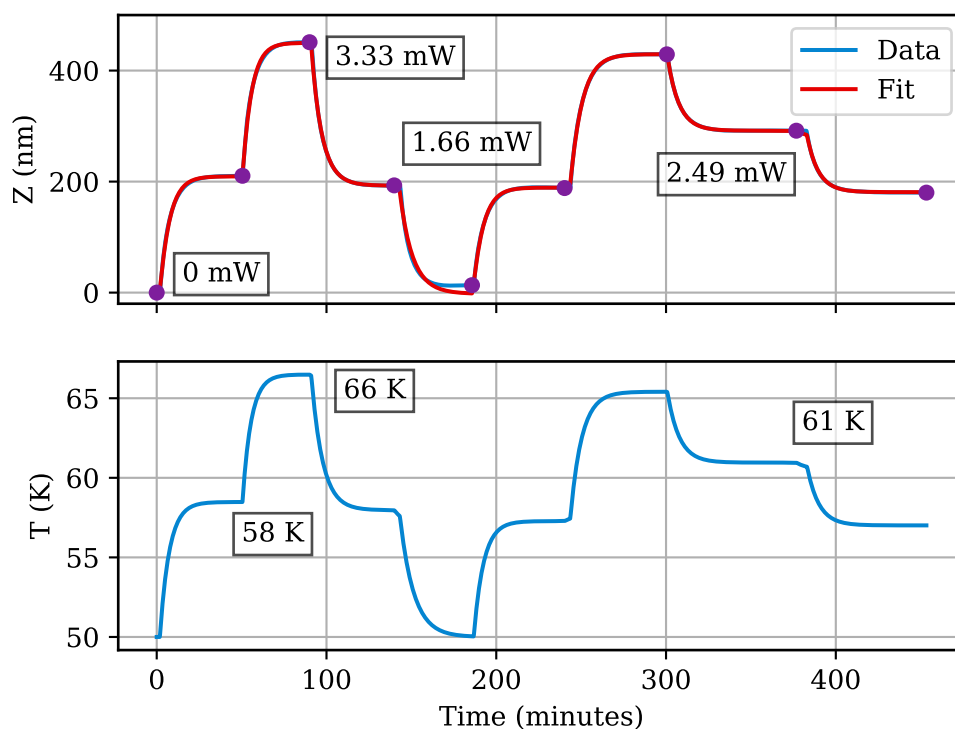


Figure 3.17: (Top) Tip position normal to the surface (blue), with fitted model (red), as a function of time, using a bulk Cr tip with steel tip holder. Laser power was held constant at the marked points while imaging and spectroscopy were performed, on the timescale of hours. Each section of Z data has been fitted separately and offset to match the end point of the previous section, to compensate for thermal drift in the STM. (Bottom) Corresponding tip temperature returned by the model. The difference of approximately 1 K between identical laser powers for the two heating sequences was taken as the error in the temperature determination.

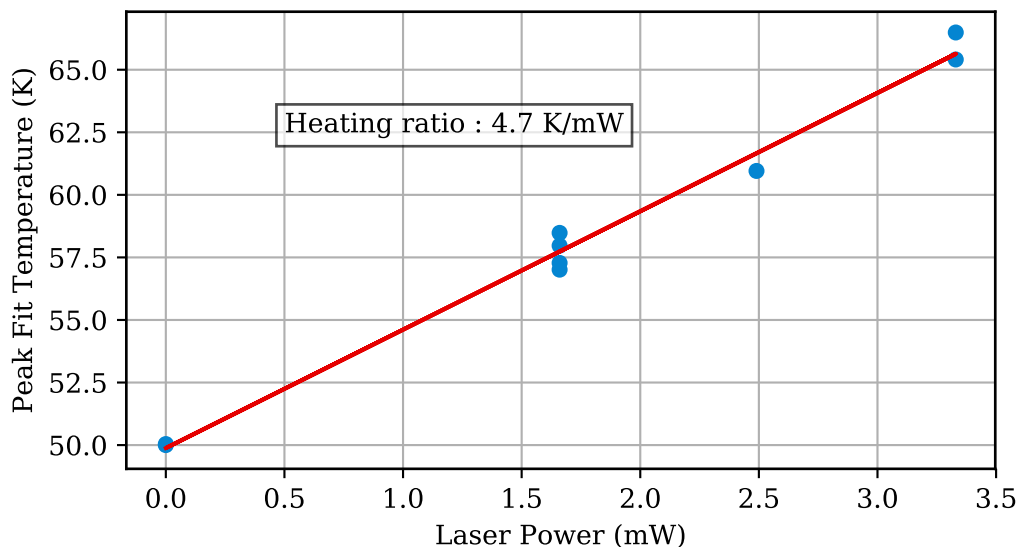


Figure 3.18: Modeled peak temperatures as a function of the applied laser power, for a bulk Cr tip. A linear fit (red) results in a heating efficiency of 4.7 K mW^{-1} .

As these results are self consistent and give reasonable values for the heating, this method of fitting the expansion of the tip and tip holder with a linear thermal expansion model will be used to provide the values of ΔT used in the following experimental analyses. This is a macroscopic approach, and will give a temperature for the bulk of the tip, but will neglect microscopic effects occurring directly at the junction. However, as the Seebeck effect is defined on a macroscopic level, this is consistent and sufficient with the measurement.

3.3 Tip-sample potential measurement

Thus far, all the requirements for inducing magneto-Seebeck tunneling have been described. The remaining step is the measurement of the generated potential, which we will describe in this section.

Based on the previous discussion, we must be able to accurately measure a change in the electrical potential between the tip and the sample on the scale of μV . However, this must be done such that the tunnel junction (i.e. the tip-sample separation) does not change appreciably during the measurement. In a solid-state planar junction, this process generally involves attaching the

measurement probes from a nanovoltmeter, or small current ammeter, to either side of the tunneling junction. With an STM however, we require continuous measurement of the tunneling current in order to maintain the tip-sample separation. This removes the ability to make open-circuit potential measurements, without some modification to the scanning procedure. Any method must also be sufficiently quick such that the sample can be scanned without lateral thermal drift becoming too large of an issue, so that atomic-scale structures can still be identified.

For this, we rely on the method of scanning tunneling potentiometry, originally introduced in the work of Muralt and Pohl [36]. This approach has been used successfully to study a variety of effects, involving both tunneling thermopower [88, 89, 33], and lateral potential gradients [90]. The general technique consists of two components: the use of an alternate feedback signal for maintaining the tip-sample separation, that is not dependent on the DC tunneling current, and a DC current compensation approach to measuring the tip-sample potential. We will discuss these in turn.

3.3.1 Constant-conductance STM

For maintaining the tip-sample separation, two approaches are apparent: The tip positioning loop can be switched on and off in a gated scheme, or an alternative signal for the tip positioning can be used. The latter must allow for simultaneous measurement of the DC tip-sample potential or current, while maintaining tip-sample tunneling contact.

The first option has been used in previous work [81], but the switching time is prohibitive, as some settling time is required after switching, either to accurately measure the potential, or to return to an equilibrium tip position prior to further scanning.

We have elected to use the second approach. The two primary candidates for alternative signals, which must be at least as sensitive to the tip-sample separation as the tunneling current (i.e. an exponential dependence), are the tunneling noise and the differential conductance. Both have been shown to depend exponentially on the tip-sample separation [91], but the thermal noise has the disadvantage of requiring extensive averaging time due to the small signal-to-noise ratio, which limits the achievable scanning speed. Critically, we require that the feedback signal will be only weakly dependent on the DC bias, when scanning with low voltages. Provided the noise is measured over some band that is well offset from 0 Hz, or that $\frac{dI}{dV}$ is measured in a linear region, both signals will fulfil this requirement.

Thus, according to our requirements, the differential conductance was used as a feedback signal for the tip positioning. This was measured using

the lock-in amplifier, as per the data shown in Section 3.1.3. In the following, we will refer to this tip-positioning feedback approach as σ – STM.

Regarding the previous requirements, we must address the data in Section 3.1.3, where it was visible that the measured $\frac{dI}{dV}$ is a mixture of topographic features and electronic structure [91, 92]. For use as a scanning feedback signal, we must show that the electronic structure contribution is minimized near the Fermi level, where the tunneling thermovoltage will be measured. We consider the expression for the tunneling current, for simplicity at zero temperature [92]:

$$I \propto \int_0^{eV} d\epsilon \rho_S(E) \rho_T(E + eV) T(V) , \quad (3.31)$$

with the transmission factor

$$T = \exp\left(-\frac{2\sqrt{2m_e}(\phi - E + eV)}{\hbar}\right) . \quad (3.32)$$

With the assumption of near-constant DOS near the Fermi level, this results in [91]

$$\frac{dI}{dV}(V) \propto e\rho_T(0)\rho_S(eV)T(V) + \int_0^{eV} d\epsilon \rho_T(\pm eV \mp \epsilon)\rho_S(\epsilon)\frac{d}{dU}T(V) . \quad (3.33)$$

Thus, with small applied bias voltages, the second term in Equation (3.33) is considered negligible, leaving only the first term, which is equivalent to Equation (3.31) for $V = 0$. Thus, when scanning in this mode at low bias voltages, the same topographic contour will be followed as in constant-current mode. This means a one-to-one correspondence between topographic features is expected between constant-current and constant-conductance images, which we will use to verify the correct operation of the scanning, and cross-talk from purely electronic features will be suppressed.

However, as outlined in Section 2.2, Seebeck tunneling also depends on the structure of the density of states directly at the Fermi level. If the tip feedback method and the Seebeck coefficient are dependent on the same tunneling parameter, then cross-talk can occur between the topographic channel and the potential measurement channel. To prevent this, a significantly larger modulation voltage for the lock-in amplification was used (> 10 mVPk – Pk), as compared to the expected thermovoltages. This means that the signal used for the positioning feedback is effectively averaged over a much larger energy band than the smaller scale Seebeck effects we are interested in. This should

aid in decoupling changes in topography from changes in S . In addition, the scan will ideally follow a contour defined by $\frac{d\sigma}{dx,y} = 0$. But as per Equation (2.21), $S \propto \sigma'$, and thus this mode will not merely scan along a contour of S .

The change in feedback signal was implemented via software in the STM controller, without requiring any change in cabling. This allows for quick switching between conventional STM and $\sigma - \text{STM}$. Experimentally, the tip can be approached to the sample using conventional STM with known settings, and once equilibrium has been achieved and the desired surface conditions have been verified, the method of tip feedback can be switched.

3.3.2 Bias compensation

As has been described in the literature [36], the tip-sample potential for a tunnel junction can be defined as the negative of the external bias that must be applied in order to maintain zero tunneling current. For measuring the potential, we note that the STM apparatus as described in Section 3.1.1 is analogous to a closed circuit, via the virtual ground of the I/V pre-amplifier. This means that a thermopower will generate an associated thermal tunneling current, which will be detected by the pre-amplifier.

The implementation of constant-conductance feedback for the tip position enables the adjustment of the DC tunnel bias without changing the tip position, at least for small changes in V and for time scales much slower than the few kHz used for the lock-in amplifier measurement. Thus, for small tunneling currents, the potential can be measured by adjusting the DC bias such that the average tunneling current is zero.

It can be pointed out that the thermal tunneling current is related to the thermopower by the tunneling resistance, which can be independently measured, and so is an equivalent measurement of Seebeck tunneling. Thus, a scan over the sample with fixed $V_{\text{bias}} = 0$, while recording the tunneling current, is also a measurement of Seebeck tunneling, only requiring a measurement of σ for an actual conversion to S . However, the practical advantage of measuring the potential directly via current compensation is that any other effects due to current, such as Joule heating, can be avoided.

To perform this potential measurement in a closed circuit situation, a feedback loop is added that measures the tunneling current and applies a compensating bias voltage to the junction, such that zero net tunneling current results. This feedback loop, operating as a PI controller, can be implemented directly as an analog component of the measurement circuit [32]. For our measurements, it was implemented using the STM control system shown in Figure 3.5, via a provided software module. With this approach,

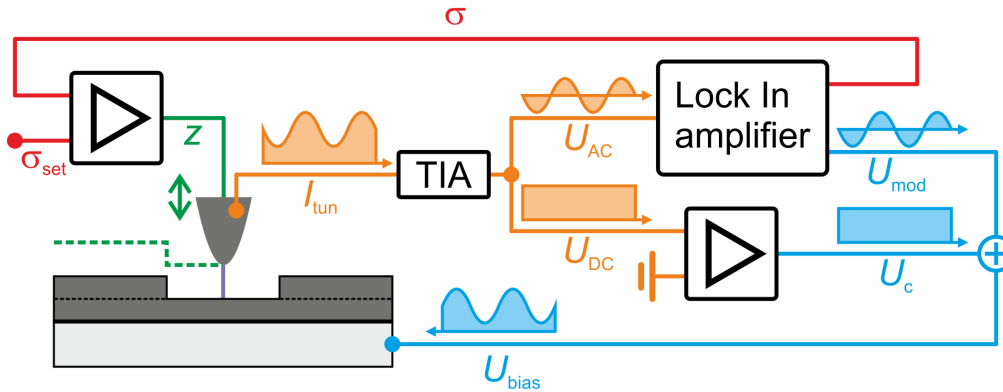


Figure 3.19: Schematic representation of the STM electronics, when operating with constant conductance and bias compensation.

the feedback loop runs on the internal FPGA, which operates directly on the input signals without any processing, minimizing the response time of the feedback. This allows for the compensation signal to be treated identically to all other measured STM quantities, meaning it can be immediately used for further calculation, as a signal for spectroscopy or feedback modules, and saved as an additional channel of any scanned images.

The only settings required are the standard PI controller parameters, in our case formulated as a proportionality constant and a time constant. These can be initially estimated by knowing the scanning speed and junction resistance. For fine tuning, the scanning speed and PI constants were adjusted while scanning to minimize overshoot effects at step edges. These can be directly identified by comparing both directions of a line scan over this feature, and minimizing the difference between them.

The implementation of the combined bias compensation and σ – STM is shown schematically in Figure 3.19. For convenience, we will still refer to this combined system as σ – STM.

3.4 AC rectification

With the previously defined apparatus, material choices, and temperature and potential measurement techniques, we can consider any complicating additional effects that may appear in the current compensation data. Given the choice of using a lock-in amplifier to measure the differential conductance, an additional effect must be considered: rectification of AC signals in the tunneling junction.

This effect is well-known for tunneling junctions, and was one of the first practical uses for these devices [80]. It arises from the asymmetric behaviour of the tunneling conductance with respect to voltage. Considering for simplicity a single frequency sinusoidal signal, this means that the average tunneling current over one period can be non-zero. This has been clearly derived in the literature, in the context of rectified laser frequencies, starting with a general Taylor expansion around $V = V_0$ of $I(V)$ [93]:

$$I(V) = \sum_{n=0}^{\infty} \frac{1}{n!} \frac{d^n I_0}{dV^n} (V - V_0)^n . \quad (3.34)$$

As per our assumption for the applied voltage, we take

$$V = V_0 + V_{AC} \cos \omega t . \quad (3.35)$$

The substitution of Equation (3.35) into Equation (3.34), followed by averaging over time, results in a DC component of the tunneling current with the form

$$I_{DC} = I_0 + \sum_{n=1}^{\infty} \frac{V_{AC}^{2n}}{2^n (2n)!} \frac{d^{2n} I_0}{dV^{2n}} \quad (3.36)$$

Here $I_0 = I(V_0)$, which is the current resulting from the DC voltage V_0 . Thus, non-zero even-numbered derivatives of $I(V)$ will result in a DC tunneling current component dependent on the modulation voltage V_{AC} . If we assume only the $n = 1$ term of the summation is significant, we get

$$I_{DC} \approx I_0 + \frac{V_{AC}^2}{4} \frac{d^2 I_0}{dV_{AC}^2} . \quad (3.37)$$

If we make the further definition that $I_0 = \sigma V_0$, and assume from the compensated conditions of the experiment that $I_{DC} = 0$, we are left with

$$V_0 = -\frac{V_{AC}^2}{4} \frac{\Sigma}{\sigma} = V_{AC\text{-rect}} , \quad (3.38)$$

where

$$\Sigma = \sigma' = \frac{d^2 I}{dV^2} . \quad (3.39)$$

The parameter V_0 in Equation (3.38) will be the voltage output by the bias compensation system.

This result can be compared to our previous expression for S from Equation (2.21):

$$S_{A/B} = -\frac{\pi^2 k_B^2 \Sigma}{6e^2 \sigma} T_{A/B}. \quad (3.40)$$

From this, it can be seen that the rectification effect has the same dependence on the ratio of the non-linear to the linear conductance. In fact, the tunneling thermopower can also be viewed as fundamentally being a rectification effect. Thermally excited electrons tunnel back and forth across the junction, but due to electronic asymmetries are slightly more likely to remain on one side of the junction rather than the other.

In general, the tunnel junction is subject to a time-dependent electrical potential, which is most commonly decomposed into a sinusoidal spectrum. We will refer to individual non-zero frequency signals within this spectrum as AC signals. These include both deliberately applied signals, such as that from the lock-in amplifier, and unwanted noise signals. This AC noise can come from either the external environment, e.g. via an open heat shield, through the STM cabling, or be generated from other physical processes, e.g. mechanical vibration varying the tunneling resistance.

In particular, the metallic, unshielded tip can act as an effective antenna for radio waves [94]. As a rough approximation, assuming the tip and holder to form an approximately 1 cm long resonator, this corresponds to a range from a few hundred MHz up to some GHz, which is potentially problematic as many measurement electronics operate in this frequency range.

Assuming for the moment a single AC signal, applied by the lock-in amplifier, we then have:

$$V_{\text{comp}} = -(V_{\text{therm}} + V_{\text{AC-Rect}}) = \left(\frac{\pi^2 k_B^2}{3e^2} T_S \Delta T + \frac{V_{\text{AC}}^2}{4} \right) \frac{\Sigma}{\sigma}. \quad (3.41)$$

Here the voltage across the tunnel junction, compensated by V_{comp} , is composed of two contributions: the thermally generated voltage, V_{therm} , and the DC voltage created by the rectification effect, $V_{\text{AC-rect}}$, as per Equation (3.38).

From this linear relationship then, the amplitude of one signal can be used to predict the other. If V_{comp} is measured for $\Delta T = 0$, then Equation (3.41) can be solved for Σ/σ . This in turn can be used to calculate S :

$$S = \frac{V_{\text{therm}}}{\Delta T} = \frac{\pi^2 k_B^2}{3e^2} T_S \frac{\Sigma}{\sigma} = -\frac{\pi^2 k_B^2}{3e^2} \frac{4V_{\text{AC-rect}}}{V_{\text{AC}}^2} T_S. \quad (3.42)$$

However, it should be noted that this relies on complete knowledge of the actual time-dependent potential present at the tunnel junction. In practice

this may be difficult to determine, e.g. given external noise sources and thermal excitations. Regardless of their source, any periodic potential will be subject to the rectification effect, as per Equation (3.38).

For relatively low amplitudes, it is reasonable to assume that the tunnel junction will react linearly [95], leading to a summation of the rectified currents due to each signal:

$$V_{\text{measured}} = V_0 + V_{\text{DC}} + \sum_{\nu} \frac{V_{\text{AC}}(\nu)^2}{4} \frac{\Sigma(\nu)}{\sigma(\nu)}, \quad (3.43)$$

where V_0 is the unmodified tip-sample potential that we would like to measure, V_{DC} is the sum of any external DC biases, and $V_{\text{AC}}(\nu)$ is the frequency dependent AC amplitude. This approximation relies on the summed amplitudes of the AC signals being small enough such that any higher order terms in $I(V)$ remain negligible. Stated another way, we must remain in a region of $I(V)$ that is well-modeled by a quadratic function.

There exists an extensive body of literature regarding the interaction and rectification of AC signals, both electronically and optically induced, in STM tunnel junctions [80, 87]. This includes detection of beat frequencies, and variation of the rectification voltage due to both thermal oscillations and time-dependent modification of the tunneling barrier. However, in this experiment we are only concerned with the net generated DC signal, and can ignore any time-dependent effects due to interacting AC signals. To simplify the analysis, we will thus define a single effective AC voltage, $V_{\text{AC-eff}}$, such that

$$\frac{V_{\text{AC-eff}}^2}{4} \frac{\Sigma(0)}{\sigma(0)} = \sum_{\nu} \frac{V_{\text{AC}}(\nu)^2}{4} \frac{\Sigma(\nu)}{\sigma(\nu)}. \quad (3.44)$$

A method for determining $V_{\text{AC-eff}}$ for a particular experiment will be shown in later analysis. The physical interpretation of $V_{\text{AC-eff}}$ is problematic, but in the low-noise environment of a well-shielded STM junction, this can be simplified as just the sum of a few incident AC signals.

The rectification will only be linear up to some high-frequency limit, determined by the mean lifetime of the electronic states that are involved in the tunneling and the operational tunneling time [80]. The idea here is that due to the discrete nature of electron tunneling, if an AC signal is of such high frequency that an electron tunneling event cannot occur in one half-wavelength, then no tunneling will occur, and the rectification current will be identically zero. In practice this limit is a few femtoseconds, corresponding to visible light, although the interpretation of these studies is ongoing.

Significant fluxes of higher energy radiation are unlikely in our experimental setup, so any non-linear effects should not be significant, and regardless would still be contained within V_{AC-eff} . Since our laser spot is focused a macroscopic distance away from the tunnel junction, we can thus assume that photo-assisted tunneling, due to stray photons from the laser or the ambient environment, will be negligible. For our purposes then, we will consider only the regime of relatively low frequency signals.

3.5 Bias spectroscopy

For an additional determination of S , we can take advantage of the low-noise spectroscopy available in cryogenic STM to directly measure $I(V)$ around the Fermi level. This is done by first establishing tunneling contact and waiting for any drift in tip position to settle. The tip height and bias compensation feedback loops are then broken, and the bias voltage swept over a specified range while measuring the resulting tunnel current. After the sweep the feedback loop is again closed, and normal operation of the STM can continue.

With sufficient resolution and averaging, accurate values for σ and Σ are acquired by numerical differentiation of the resulting spectroscopy curves. These values can then be substituted into Equation (2.21) to predict S . They can also be used to predict the rectification voltage via Equation (3.36).

3.6 Measurement technique for Seebeck tunneling

Given the description of the basic STM in Section 3.1.1, the tip and sample systems in Sections 3.1.2 and 3.1.3, the thermal gradient creation and measurement in Section 3.2, and the measurement of the tip-sample potential in Section 3.3, the measurement of magneto-Seebeck tunneling is possible.

Starting with the prepared sample and tip in the cooled STM, the basic procedure will be as follows. First the tip is approached to within tunneling distance of the sample, either in conventional STM or σ -STM mode. The laser is mounted and aligned, then switched off, and the system is monitored until thermal equilibrium returns, as observed in the drift rate of the tip position. The tip is then scanned over the sample, using the σ -STM mode, and, at minimum, the topographic and compensating bias signals are simultaneously recorded.

The laser is then switched on at some defined power. The resulting tip expansion due to heating is recorded by maintaining tunnel contact and

recording the vertical tip position over time. Once this has reached some plateau, indicating a new thermal equilibrium has been reached, the sample is again scanned with the same feedback parameters and the change in tip-sample potential for the different areas of the sample is recorded. This change, stated as a function of the change in temperature acquired from the expansion data, then gives a measure of S . The measurement is repeated for multiple steps in laser power, both increasing and decreasing, to increase the accuracy of the final result.

For additional confidence in the acquired measurement of S via tip-heating and potential measurement, additional independent approaches to measuring S in the same tunneling conditions are required. From the previous sections, we have defined two separate purely electronic methods to predict S while assuming $\Delta T = 0$. The comparison of these results to the directly measured value for S serves first as a verification of the preceding assumptions for temperature modeling, and second as a proposal to use these methods, which are experimentally easier to implement, as a useful tool to quickly predict S in existing STM setups without requiring any modifications.

In equilibrium conditions then, for the same tip, bias spectroscopy curves and the compensation voltage as a function of the amplitude of the lock-in modulation are also recorded. These can then be used to calculate predicted values for S , giving a complete set of inter-related measurements, providing increased confidence in our approach.

3.7 Summary

In this Chapter, we have presented the necessary experimental elements for measuring (magneto-)Seebeck tunneling using an STM.

First, the realization of the necessary tunneling junction was presented. This required a description of the VT-STM used for the experiments, as well as the tunneling tips and sample systems used in the experiments.

Following this, the thermal environment of the STM was presented in more detail. This involved modeling of the equilibrium heat transfer between the major components of the system, description of the heating of the tip via external laser, and the proposed method for measuring the resulting temperature differential between the tip and the sample.

With the thermal environment understood, we then discussed the method for measuring the electric potential between the tip and the sample. This constant-conductance STM (σ -STM) allows for lateral imaging of this potential, and is an established technique in literature. For our experiments, it was

combined with a magnetic tunneling tip to allow for magnetically resolved measurements.

Finally, experimental considerations were explored, with the effect of AC rectification, the technique of bias spectroscopy, and a summary of our measurement technique for Seebeck tunneling detailed.

Chapter 4

Spin-averaged Seebeck tunneling

In this Chapter, the result of applying the previously outlined experimental methods to a sample of single and double atomic layers of Fe on W(110), recorded using a bulk W tip, will be presented. The resulting data, lacking spin-contrast, will be used to demonstrate the behaviour of the constant-conductance, compensated current STM method ($\sigma - \text{STM}$), and verify the predictions made in Chapters 2 and 3. This will establish a basis for later chapters, which will focus on the magnetic results. Parts of this analysis has been published in Journal of Physics D [82].

First, the baseline performance and attributes of $\sigma - \text{STM}$ will be demonstrated, using images of the surface recorded with no tip heating. The processing and analysis of these images will be outlined, and comparisons will be made to conventional STM images of the same area.

This will lead into a discussion of the measured V_{Comp} without tip heating. Bias spectroscopy will be used to predict the expected AC rectification potential, and a technique will be presented to account for systematic biases in both DC and AC signals.

Following this, we make predictions for S , on both the Fe DL and Fe ML, along with values for the various surface structures, using bias spectroscopy and AC rectification results. This is followed by the effect of heating power being applied to the tip, which results in a direct measurement of S for surface structures. The predictions and measured data will then be compared and discussed. The results of multiple datasets will be presented, to demonstrate the reliability of the measurement technique.

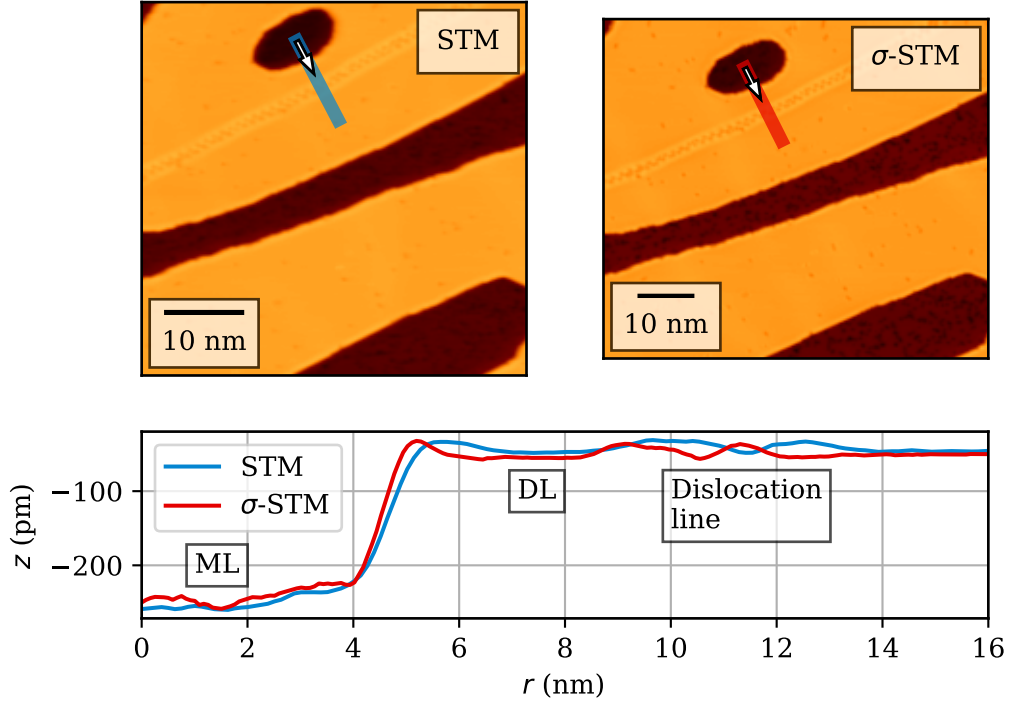


Figure 4.1: (Top left) Topographic STM image of the Fe DL on W(110), imaged using a W tip, with $U = 25$ mV, $I_{\text{set}} = 1$ nA, and $T_{\text{Sample/Tip}} = 50$ K. (Top right) Same area subsequently imaged using σ -STM, with a conductance setpoint of 2.8 nS. The bias feedback loop was closed, meaning the nominal DC current for the image was zero. (Bottom) Comparison of indicated lateral profiles from the STM and σ -STM images.

4.1 Topographic comparison

The result of imaging the topography of a sample of nominally 1.7 atomic layers of Fe on W(110) using σ -STM is shown in Figure 4.1. This was performed on the same area as the data in Figure 3.7, which is shown again here for comparison. The regular STM data was collected with a setpoint of 1 nA with a bias of 25 mV. The σ -STM data was collected using a conductance setpoint of 3.3×10^{-9} nA V $^{-1}$, as measured using a lock-in amplifier. The amplifier was operated with an output sinusoidal voltage $V_{\text{AC}} = 6$ mVRMS, at a frequency of 3.2 kHz. The trans-impedance amplifier was set to a gain of 10×10^8 A V $^{-1}$, which results in a manufacturer specified bandwidth of 7 kHz, allowing for adequate detection of the conducted AC signal.

As can be seen from the figure, the same topographical features are

present with both imaging techniques. As can be seen in the comparison of line profiles, effectively the same step height and variation over the dislocation line are measured. In addition, a one-to-one match of impurities is also present.

This is reasonable, because when performing conventional STM scanning with a fixed bias potential, the tip-sample separation is adjusted to maintain a constant current. This also results in a constant conductance contour being followed, albeit the integrated conductance rather than the differential conductance. As the metal-insulator-metal tunnel junctions generally have near-Ohmic behaviour near the Fermi level [95], and we are scanning with low bias voltages, then the integrated and differential conductances are practically equal.

The only difference then is that with $\sigma - \text{STM}$ the conductance must be measured. As this is a second-order effect, with respect to the bias and current, this in general necessitates a longer measurement time, and is more susceptible to measurement noise. Specifically, the STM image in Figure 4.1 was completed in 21 min, while the $\sigma - \text{STM}$ image required 5.7 h.

We can thus conclude that the STM and $\sigma - \text{STM}$ techniques follow the same topographical contours of the sample during scanning, enabling direct comparison of the results. The actual tip-sample separation will depend on the feedback setpoints used.

4.2 Compensated current imaging

The corresponding bias signal for Figure 4.1, collected with the compensating feedback loop closed, is shown in the bottom of Figure 4.2, with the differential conductance map of the same area imaged with regular STM shown above for comparison. As with the topographic channel, there is a one-to-one correspondence between the structures present in both images. The slower scanning speed of the $\sigma - \text{STM}$ image leads to an increased influence of lateral thermal drift, which is readily apparent in the shape of the ML vacancy near the upper-center of the images, which differs between the images.

While the equivalence of the surface geometry is apparent, the connection between the relative changes in amplitude of the two signals requires further consideration. From Equation (2.16) it is understood that $\frac{dI}{dV}$ is a result of the product of the DOS of tip and sample, offset by the applied bias potential. However, the actual measurement of $\frac{dI}{dV}$ is not a point measurement, but is rather a result of the averaged DOS over the energy range of the applied lock-in signal, $\pm V_{AC}$. This is relevant, if we consider the regime of low bias voltages, as we are using here. During the STM scan, the tip

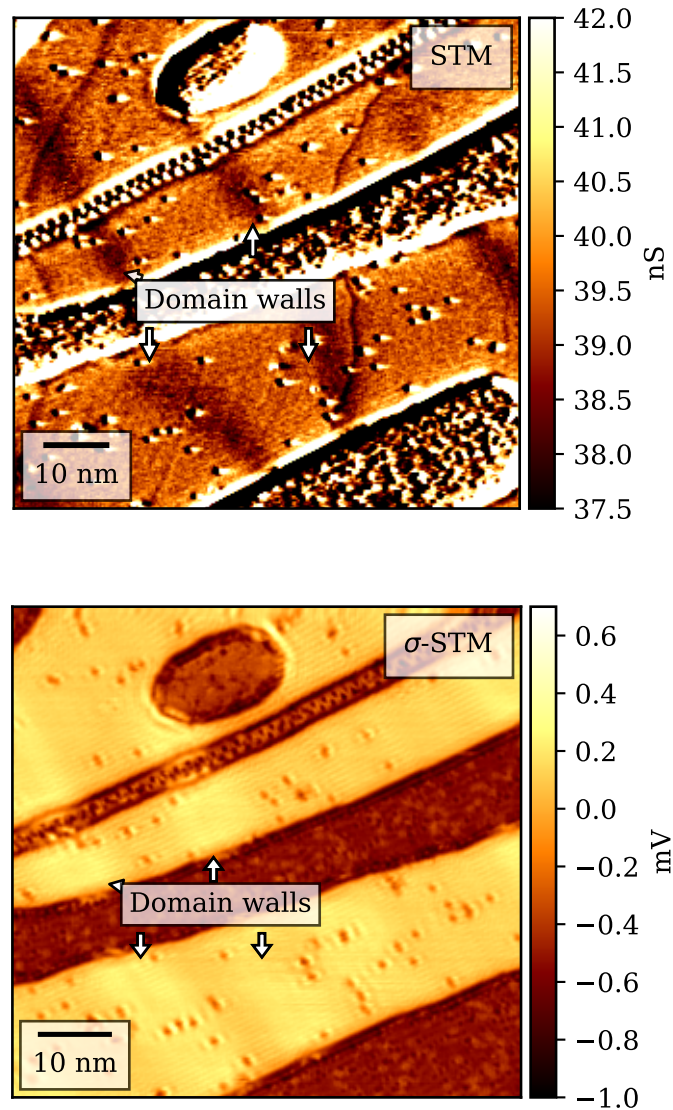


Figure 4.2: (Top) Differential conductance image of the Fe DL on W(110), imaged using a W tip, with $U = 25$ mV, $I_{\text{set}} = 1$ nA, and $T_{\text{Sample/Tip}} = 50$ K. (Bottom) Bias channel of σ -STM image of same area, taken with a conductance setpoint of 2.8 nS. No laser heating was applied while imaging, meaning that the tip is nominally at the same temperature as the sample. The same four domain walls are noted in both images for comparison.

will follow a DOS contour, or equivalently stated, will maintain a constant tunnel conductance. In a perfectly Ohmic regime, the $\frac{dI}{dV}$ would then have the same value as this tunnel conductance, and we would expect no contrast in the $\frac{dI}{dV}$ image. The fact that we do see structure must then come from non-linearities present in the DOS.

This then explains the one-to-one correspondence with the V_{comp} image. As explained earlier, both the Seebeck voltage and any AC rectification voltage depend on the ratio of the 2nd order non-linear conductance $\frac{d^2I}{dV^2}$ to the linear conductance. For the $\frac{dI}{dV}$ contour followed by $\sigma - \text{STM}$ then, any contrast must arise in $\frac{d^2I}{dV^2}$, giving the connection to the $\frac{dI}{dV}$ STM channel. Practically any change in electronic structure should appear in the images, provided it is not just a constant offset, whether due to changes in atomic position for stress relief as in the dislocation lines, or due to tunneling anisotropic magneto-resistance (TAMR) as evidenced by the presence of domain walls in both images (labeled).

The difference in noise and resolution then comes from the details of the feedback techniques. For comparison, we note that the $\frac{dI}{dV}$ image in Figure 4.2 has not been corrected at all, and imaging took 21 min. This relatively fast scanning results in the overshoot observed near the step edges, and low resolution in areas of detailed electronic structure, such as the dislocation lines.

The V_{comp} image, on the other hand, required 5.7 h. The speed of the V_{comp} scanning is limited by the tip-position feedback loop. The speed must be slow enough that the lock-in amplifier can measure $\frac{dI}{dV}$ with sufficient accuracy, so that the tip is moved in the proper direction. If the scan speed is too fast the tip movements will be essentially time delayed, resulting in tip crashes or imaging artifacts. In the case of the scan speed being too fast for the bias feedback loop to maintain zero net tunneling current, the measured value for V_{comp} will be incorrect. This has been corrected by estimating the correct value for V_{comp} using the non-zero tunneling current, as described in Appendix B. This correction has been applied to all images used in this analysis.

Some additional effects can be observed in the V_{comp} image as well. The suppression of overshoot effects at the edges allows for much greater resolution of the interaction of the domain walls with the step edges and dislocation lines. In addition, one can see that the average value for the ML vacancy near the top of the image differs from that of the extended ML areas elsewhere, while this detail is not apparent in the $\frac{dI}{dV}$ image.

4.2.1 Measurement of average tip-sample potential

Before continuing with the discussion of the components of the observed V_{comp} signal, we will first define the procedure for determining the average value of a region. The average compensation biases from Figure 4.2 for the ML and DL domains are $V_{\text{comp-ML}} = -0.52 \text{ mV}$ and $V_{\text{comp-DLDM}} = 0.12 \text{ mV}$ respectively. In addition, as a demonstration of the ability of this approach to examine smaller structures, the value for the domain walls was also determined to be $V_{\text{comp-DL-DMW}} = 0.21 \text{ mV}$.

These were found by creating a histogram of V_{comp} only for the area of interest, determined by drawing a mask over the image. The resulting histograms exhibited a normal distribution, which is reasonable as the applied and measured voltage should both be subject to thermal fluctuations in the electronic components (e.g. cabling, analog-digital converters, etc.). Thus it was sufficient to fit a Gaussian function to the histograms to determine the mean. This is demonstrated in Figure 4.3. For the domains, individual impurities were removed from the mask, but in practice their presence only adds a slight shift in the distribution. In later analysis, this approach will be assumed whenever V_{comp} for a specific surface area is measured.

4.3 Sources of contrast in potential

Now that we have shown that the tip-sample potential can be reliably measured, the possible sources of such a potential can be discussed. The σ -STM image in Figure 4.2 was recorded without laser heating applied to the tip, implying that, at least nominally, $\Delta T = 0 \text{ K}$. The fact that significant contrast was nevertheless observed between sample areas indicates that a careful analysis of additional signal sources is required.

If any DC biases are present, for example from the measurement electronics, these will appear as a systematic error in the measured compensation bias, leading to an offset in the measured values. This can arise from differences in grounding between e.g. the STM control electronics and the lock-in amplifier, or from internal offsets in the instruments. This will give rise to a shift in the DOS of one side of the tunnel junction relative to the other, leading to different values for σ and Σ . However, this would not in general lead to a contrast between different areas of the sample, and so can be treated simply as a voltage offset V_{DC} .

As described in Figure 3.19, an AC signal is applied to the junction via a lock-in amplifier to measure the tunnel conductance. Thus a portion of the observed signal can be attributed to AC rectification of the lock-in applied

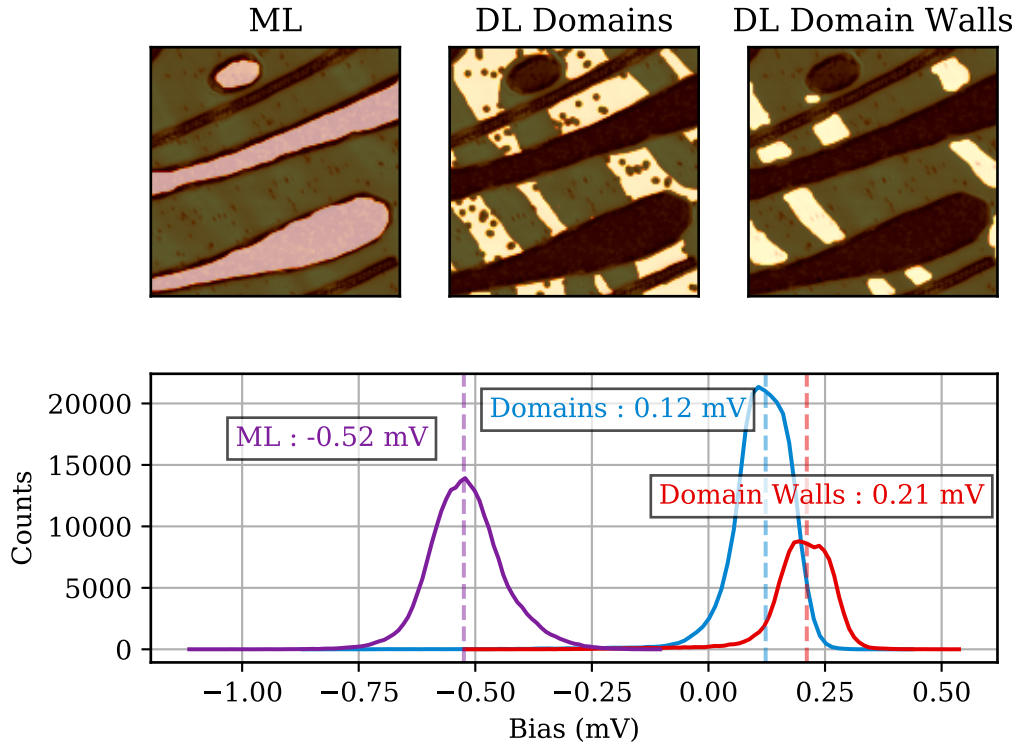


Figure 4.3: (Top) U_{comp} images of Fe on W(110), imaged using a W tip, with $\sigma_{\text{set}} = 3.2 \text{ nA V}^{-1}$, and $T_{\text{Sample/Tip}} = 50 \text{ K}$. Overlaid on the images are manually applied masks (bright) indicating the Fe ML, Fe DL domains, and Fe DL domain walls. (Bottom) Histograms of the areas under the masks, with the labeled means determined by fits of Gaussian functions (not shown), result in values of $V_{\text{comp-ML}} = -0.52 \text{ mV}$, $V_{\text{comp-DL-DM}} = 0.12 \text{ mV}$, and $V_{\text{comp-DL-DMW}} = 0.21 \text{ mV}$.

modulation voltage, as predicted in Section 3.4. Any additional signals, for example from measurement electronics, will also in principle be rectified, contributing to the measured V_{comp} .

4.4 Bias spectroscopy

To understand and decompose these signal contributions, $I(V)$ spectroscopy was performed, with a different tip but same sample preparation, as described in Section 3.5. Examples of the resulting curves, for the ML and for the DL, are shown in Figure 4.4. From these curves, values for σ and Σ were acquired by fitting a third order polynomial to the I/V data.

These values were then used to calculate predictions for V_{rect} for these areas using Equation (3.38), given the known value for V_{AC} from the lock-in amplifier. This procedure results in the prediction of $V_{\text{rect-ML}} = 71 \mu\text{V}$ and $V_{\text{rect-DL}} = 209 \mu\text{V}$. As discussed previously, this arises from $|\Sigma_{\text{DL}}(0)| > |\Sigma_{\text{ML}}(0)|$. However these predictions differ significantly from the average value of these areas in Figure 4.4, both by their offset from zero, and by the difference between the two areas.

4.4.1 Effective AC signal and DC offset

Given the discrepancy between our prediction and the measured values, it must be that $V_{\text{AC-eff}}$ varies significantly from $V_{\text{AC-lockin}}$. If bias spectroscopy is available for two distinct areas of a sample, a relatively simple procedure can be used to simultaneously determine both V_{DC} and $V_{\text{AC-eff}}$. To show this, we will consider the Fe ML and Fe DL data from 4.4. For an analytical explanation, we make the assumption that the same V_{DC} and $V_{\text{AC-eff}}$ must be present when scanning over both areas, as they arise from external sources. It then follows that we must have

$$V_{\text{ML}} = \frac{V_{\text{AC-eff}}^2}{4} \frac{\Sigma_{\text{ML}}}{\sigma_{\text{ML}}} + V_0 = V_{\text{AC}}^2 \beta_{\text{ML}} + V_0 \quad (4.1)$$

and

$$V_{\text{DL}} = V_{\text{AC-eff}}^2 \beta_{\text{DL}} + V_0, \quad (4.2)$$

where the substitution $\beta = \Sigma/4\sigma$ has been made. This system can be solved for V_0 and $V_{\text{AC-eff}}$, giving us

$$V_0 = V_{\text{ML}} - \beta_{\text{ML}} \frac{V_{\text{DL}} - V_{\text{ML}}}{\beta_{\text{DL}} - \beta_{\text{ML}}} \quad (4.3)$$

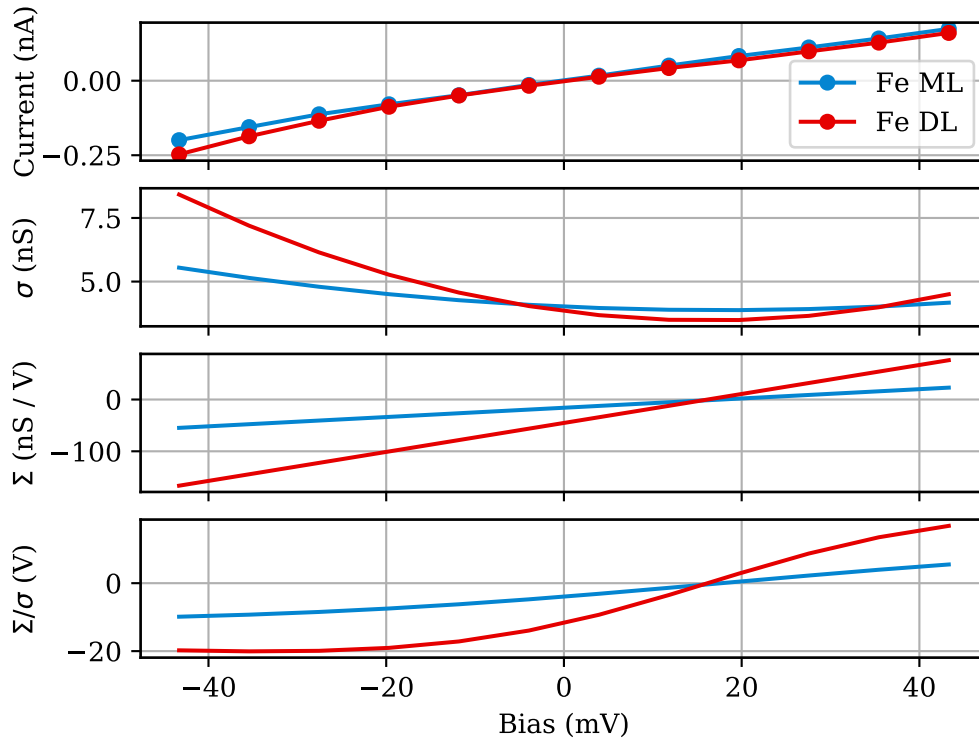


Figure 4.4: Representative curves of $I(V)$ for the Fe ML and DL, with $T_{\text{Tip-Sample}} = 50\text{ K}$ and a modulation voltage of 6 mVRMS . $\sigma - \text{STM}$ was used to position the tip between spectroscopy points, with a feedback setpoint of 3.8 nA V^{-1} . The top plot shows the acquired data points, fitted by a third-order polynomial. The resulting $\sigma(V)$ and $\Sigma(V)$ calculated from this fit are shown in the subsequent plots. The ratio Σ/σ is shown in the bottom plot, showing a difference between the ML and the DL for $V = 0$.

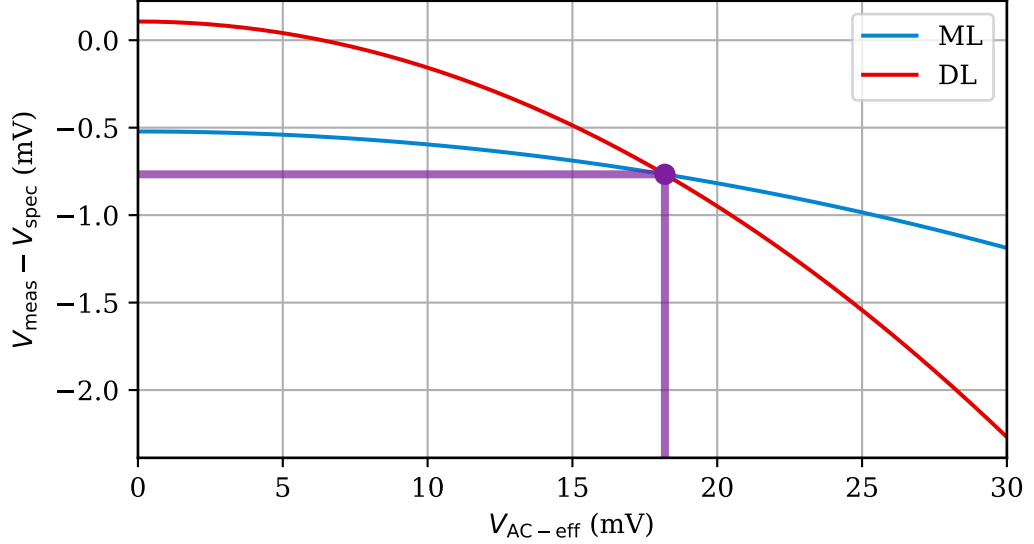


Figure 4.5: Difference between the measured $V_{\text{ML/DL}}$, V_{meas} , and the value calculated from spectroscopic conductances, V_{spec} , as a function of applied modulation voltage. The indicated crossing point gives the result for both $V_0 = -760 \mu\text{V}$ and $V_{\text{AC-eff}} = 18.2 \text{ mV Pk-Pk}$.

and

$$V_{\text{AC}}^2 = \frac{V_{\text{DL}} - V_{\text{ML}}}{\beta_{\text{DL}} - \beta_{\text{ML}}}. \quad (4.4)$$

Thus, given experimental values of $\beta_{\text{ML/DL}}$, the external DC and AC signals can be found. This can be seen as the crossing point of the two curves in Figure 4.5, where the difference between the compensation voltage predicted by Equation (3.38) and the actual measured values, as a function of the applied modulation voltage, are plotted.

As these values will vary between every experiment and apparatus, being able to quickly calculate these values is a useful calibration tool.

4.4.2 AC rectification

To verify that the rectification potential behaves as predicted in Section 3.4, an experiment was performed, with a different sample preparation than the previous data but still Fe on W(110), where the tip was brought into tunneling contact with the sample in $\sigma - \text{STM}$ mode. The door was closed

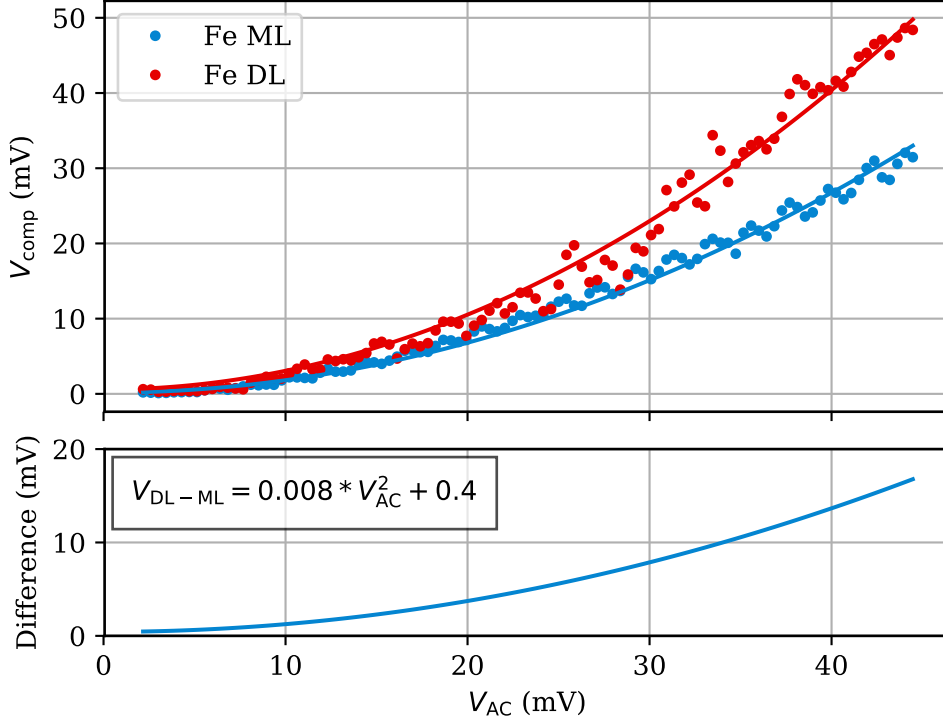


Figure 4.6: (Top) V_{comp} vs. AC amplitude of a second applied AC signal, on the Fe ML and DL on W(110), with a W tip and $T_{Tip-Sample} = 50$ K. The tip position feedback loop was open during the sweep. Both curves are fitted by a quadratic function, and the difference between the fits is plotted (Bottom).

during this experiment, to minimize external signals. A second AC signal, at a different frequency, was applied to the junction, and the peak-to-peak amplitude of this second signal was swept from 0 mV to 45 mV. Representative curves for both the ML and DL are plotted in Figure 4.6.

As can be seen, the compensation bias indeed exhibits a quadratic dependence on the applied AC signal on both areas, indicated by the plotted solid lines. This implies that the rectified AC signal from the lock-in amplifier and the rectified second AC signal indeed combine linearly. Thus, as long as the combined magnitude of the AC signals is small relative to the curvature of Σ in Figure 4.4, we can treat them as independent, as per our assumptions in Section 3.4. We will also assume that σ and Σ are independent of frequency [80].

The difference between the fits of the two areas is given by the function

$V_{\text{DL-ML}} = 8 \mu\text{V}^{-1} V_{\text{AC}}^2 + 0.4 \text{ mV}$. As a check, from the remnant contrast of 0.4 mV , we can calculate that $V_{\text{AC-eff}} = 7 \text{ mV}$, which indeed matches the amplitude of the lock-in amplifier used during the experiment. Thus for this experiment we can see that the only strongly contributing AC signals were the ones applied by the lock-in amplifier and our swept signal. We can thus conclude that the AC rectification effect is present as expected, and that for small signals can be treated as either a linear combination of contributions, or as arising from a single effective AC voltage.

4.5 Predicting Seebeck values

Now that the baseline V_{comp} signal is understood, and the validity of the feedback method established, the actual experimental goal of measuring S can be realized. Before the tip-heating experiment is performed, values for S can be predicted from the AC rectification data, as per Section 3.4, and from bias spectroscopy, as per Section 3.5.

Examples of bias spectroscopy on the ML and DL were already displayed in Figure 4.4. These were taken as part of a line of spectroscopy points, on both the ML and the DL. The reference image for the line of spectroscopy, as well as resulting predictions for V_{rect} and S , are shown in Figure 4.7. The modulation voltage $V_{\text{AC-eff}}$ used to calculate V_{rect} was found as per Section 4.4.1.

Here the ML and DL can be clearly distinguished by an abrupt change in Σ , with a corresponding change in the calculated S . From this data, we can predict Seebeck values of $S_{\text{ML}} = 3.1 \mu\text{V K}^{-1}$ and $S_{\text{DL}} = 13.4 \mu\text{V K}^{-1}$. The agreement between the V_{rect} predicted from spectroscopy and the actual measured values in Figure 4.3, makes the calculated S effectively a prediction from both datasets.

4.6 Tip-heating data

With the previous sections, we have predictions for S on the sample surface: the average ML and DL via bias spectroscopy, and of more detailed structures via AC rectification mapping. We can now compare these to the actual results of tip heating experiments.

The experiments were performed as described in Section 3.6. This was done for two different tip preparations on the same sample preparation, here referred to as datasets 1 and 2, in order to test the reproducibility of the results. The tip consisted of bulk W in a Mo tip holder. The tip expansion

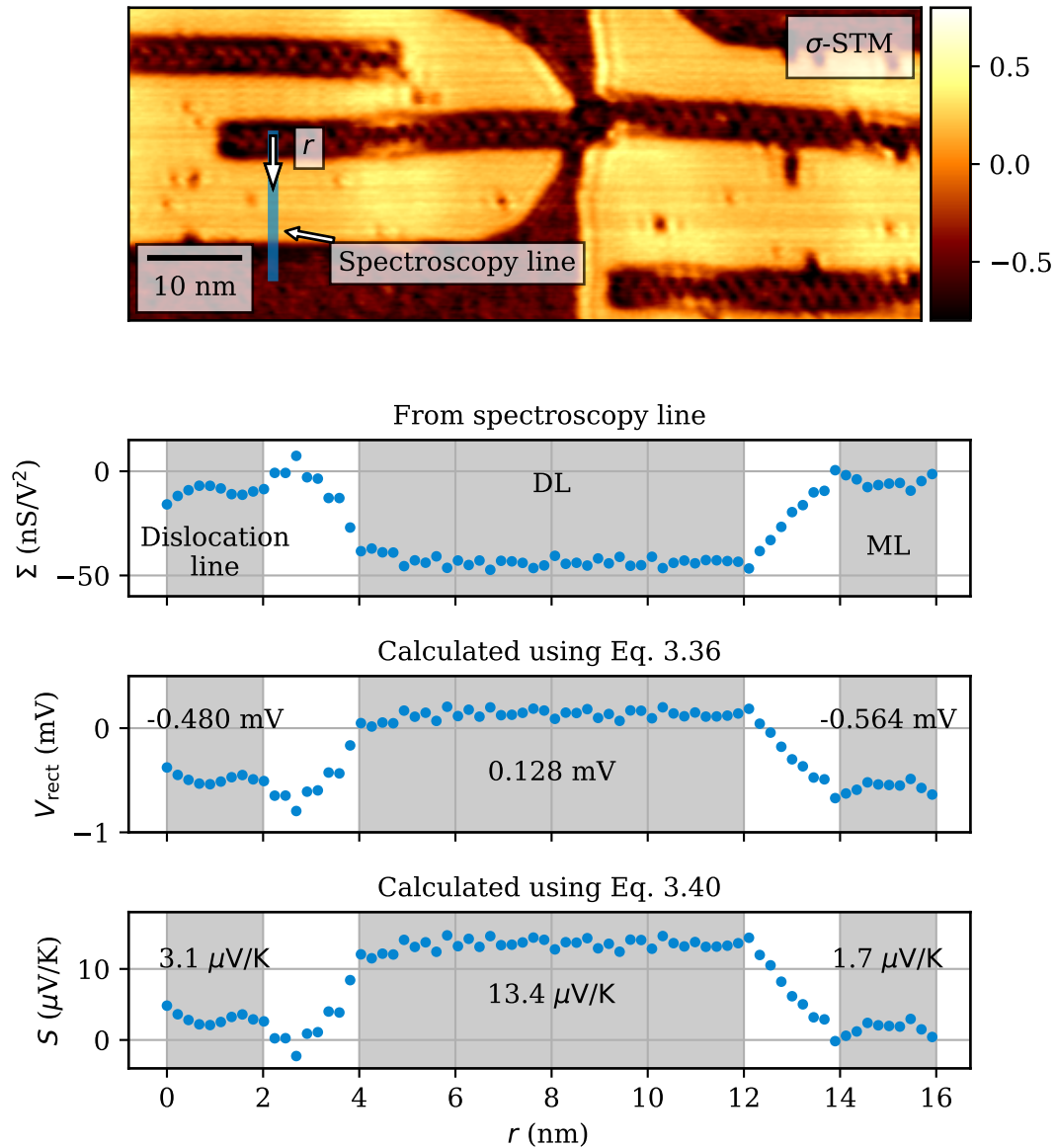


Figure 4.7: Results of bias spectroscopy along a line, proceeding from a dislocation line on the Fe DL, to the Fe DL, and on to Fe ML. (Top) Reference image, with the spectroscopy line indicated. Proceeding downwards, the plots show Σ , acquired from the spectroscopy points as per Figure 4.4, V_{rect} calculated from Equation (3.38) using the experimental parameters, and S , calculated using Equation (3.42).

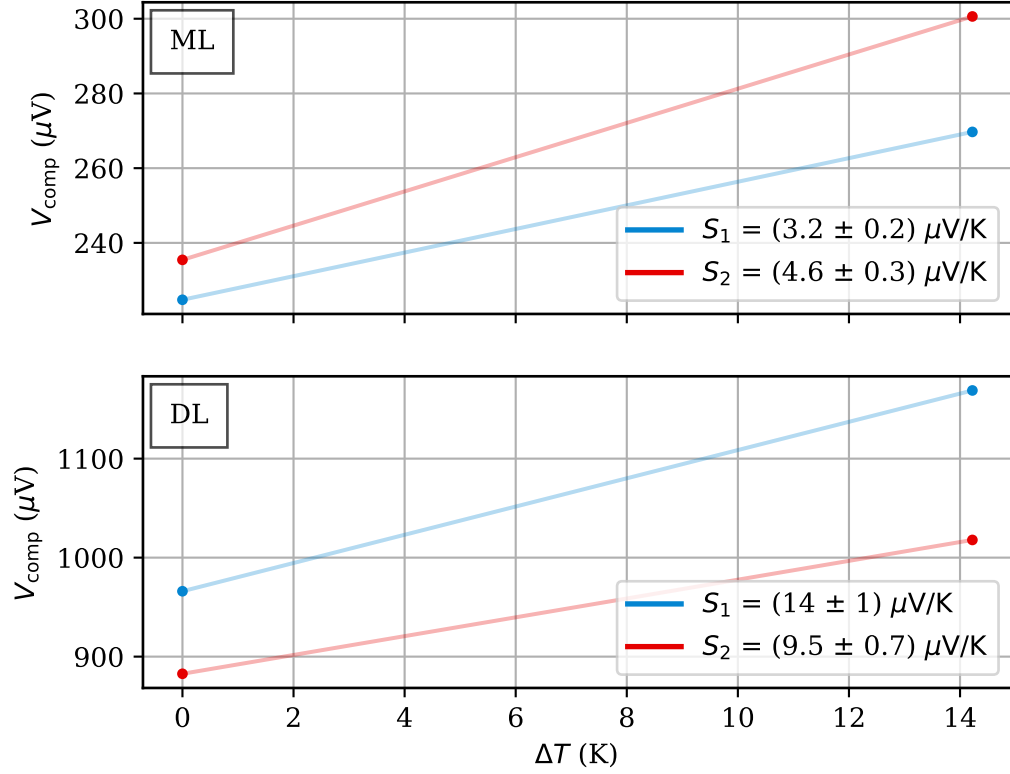


Figure 4.8: Change in compensated bias as a function of ΔT , for the (top) Fe ML and (bottom) Fe DL domains, with the resulting values for S .

data, similar in form to Figure 3.15, was fitted to provide the tip temperature as a function of laser power, giving an effective heating coefficient of 9.4 K mW^{-1} , twice that of the bulk Cr tip. Since the tip temperature tends to follow that of the tip holder, this change can be attributed to the properties of Mo vs steel, in addition to any variation in the alignment of the laser.

For datasets 1 and 2, the initial measurements were performed in thermal equilibrium, with the STM door already open. The laser was then turned on to a fixed value of 1.66 mW , and the second datapoint was collected after equilibrium was again reached. The results for the two datasets are shown in Figure 4.8.

We can now discuss the results in turn. Dataset 1 was measured using the same tip preparation as used for the lateral bias spectroscopy shown in

Figure 4.7. This spectroscopy predicted values of $S_{\text{ML-Spec}} = 3.1 \mu\text{V K}^{-1}$, and $S_{\text{DL-DM-Spec}} = 13.4 \mu\text{V K}^{-1}$. We can compare this to the measured values for $S_{\text{ML-Heated}} = 3.2 \mu\text{V K}^{-1}$ and $S_{\text{DL-DM-Heated}} = 14.3 \mu\text{V K}^{-1}$. As can be seen, there is an excellent agreement between the spectroscopic results and the actual heating data. This agreement is significant, as it validates the method of measuring both V_{comp} and ΔT . While the tip-sample potential measurement for V_{comp} is already established in the literature, the verification of the approach for ΔT is a novel result.

On the topic of repeatability, we can move on to discuss dataset 2. Again, this was the same sample preparation, but with a different W tip preparation. We can see that the contrast between the ML and DL domains is slightly reduced at all data points. As per Section 4.4.2, assuming that the feedback system is keeping σ constant, this means that the difference in Σ between the two areas is reduced. Given the offsets relative to dataset 1 then, we can conclude that Σ_{ML} has increased slightly, and $\Sigma_{\text{DL-DM}}$ has decreased. This should correspond to an increase/decrease in $S_{\text{ML/DL-DM}}$, which is precisely what is observed. This again demonstrates the predicted connection between V_{rect} and V_{comp} .

4.7 Summary

In this Chapter, the results of spin-averaged measurements of V_{comp} on the Fe ML/DL on W(110) were presented and compared to standard STM imaging. It was demonstrated that the σ – STM technique follows equivalent topographical contours as conventional current-feedback STM, and that electronic structures appearing in $\frac{dI}{dV}$ images tend to also appear in V_{comp} images, as expected. A standard method for measuring the averaged V_{comp} value for given areas was then defined.

Following this, the magnitude of the measured potential was discussed. The contrast achieved with no tip-heating was adequately explained in terms of the predicted effect of AC rectification, with support from $I(V)$ spectroscopy. This was used to make predictions for Seebeck values of both the Fe ML and DL. These areas were then investigated using heated-tip imaging, from which values for S were obtained in good agreement with those spectroscopically predicted.

This agreement justifies the applied approximations for the linear expansion tip-heating model employed to calculate ΔT , and the literature predictions for the linear dependence of S on Σ [40]. Additionally, the consistency of these results implies that accurate predictions for S can be made without the need to modify an apparatus to support the creation of ΔT , meaning that

this technique can be applied with only minor software changes to existing STM setups.

Chapter 5

Spin-dependent Seebeck tunneling

In this Chapter we will present the results of applying the method of σ -STM and tip-heating to the Fe mono/double layer (ML/DL) on W(110) for $T_{\text{STM}} = 50$ K, this time using a spin-polarized bulk Cr tip to provide magnetic contrast. In this analysis, we will rely on the results of Chapter 4 regarding the basic behaviour of the spin-averaged results and the correspondence between spectroscopic results and S . Thus we will focus on the magnetic tip-heating data, giving a direct measurement of magneto-Seebeck tunneling on the Fe DL on W(110).

To start, we will again compare the results of imaging the same sample area with STM and with σ -STM (without tip heating), focusing on the comparison of the electronic structure via the $\frac{dI}{dV}$ channel and V_{comp} channel respectively. This will be followed by the actual tip-heating data for the Fe DL, and the resulting surface-dependent values for S will be used to translate a V_{comp} image without tip heating into an image of S . This will then be used to analyze the spin-dependent domain wall structure. As a last step, the results of the imaging technique being applied to the Fe ML/DL on Ir(111) will be shown. A significantly lower STM temperature of 25.3 K was used, as at these temperatures the Fe ML exhibits a nanoskymion lattice, further demonstrating the capability of σ -STM to study S at the nanoscale, and its potential use in future technological applications.

5.1 Method comparison

The sample of Fe layers was again prepared according to Section 3.1.3, and the temperature of the STM was again held constant at 50 K. This temperature was chosen to be as low as possible to increase the relative heating power of the laser, while remaining under the Curie temperature of the Fe layer

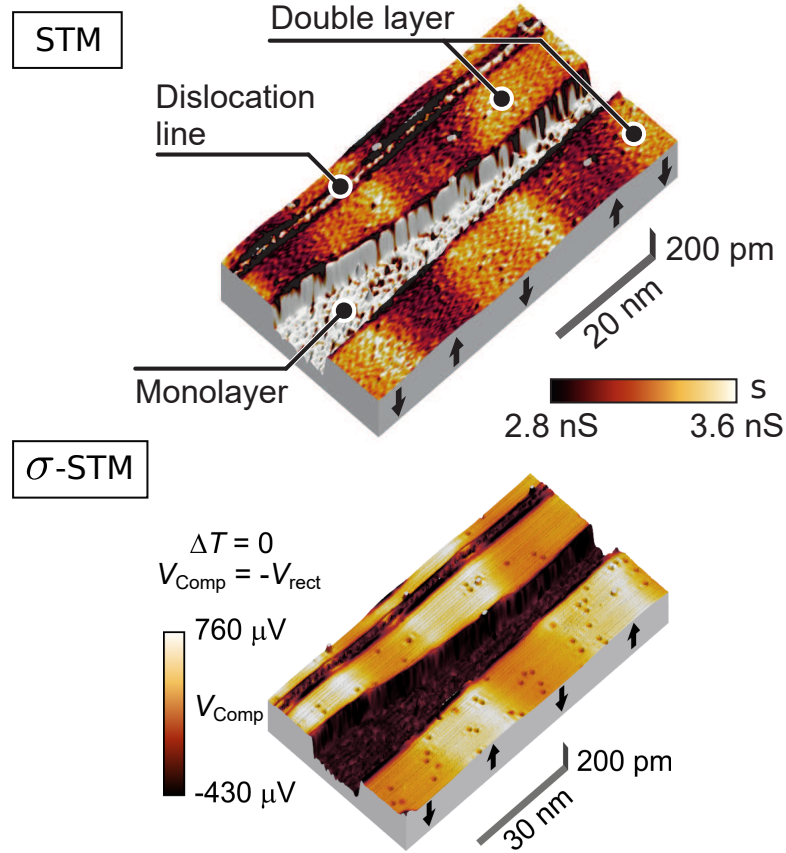


Figure 5.1: (Top) STM image of the Fe DL on W(110), imaged using a bulk Cr tip, with $V = 250 \text{ mV}$, $I = 1 \text{ nA}$, and $T_{\text{STM}} = 50 \text{ K}$. The topography is shown on the vertical axis, and is colored by the $\frac{dI}{dV}$ data. (Bottom) σ -STM image of the same area, with $\sigma_{\text{set}} = 8 \text{ nS}$, and $V_{\text{mod}} = 6 \text{ mVRMS}$. Again, the vertical axis is the topography, now colored by the V_{comp} data.

(220 K [96]) and under the Néel temperature of the bulk Cr tip (311 K [97]), and keeping liquid He consumption low enough to allow for the extended measurement times required by the relatively slow scanning of σ -STM.

The subsequent result of imaging the Fe ML/DL using both STM and σ -STM under these conditions is shown in Figure 5.1. The STM image was taken with a bias voltage of 250 mV, and a current feedback setpoint of 1 nA. For the σ -STM image, the imaging was performed with a RMS voltage of the sinusoidal lock-in signal of 6 mV, and the tip feedback setpoint was set to 8 nS.

As has already been determined from Chapter 4, the topographical data in both images is essentially identical. We will thus focus on the additional

magnetic information in the electronic structure data; i.e. the $\frac{dI}{dV}$ and V_{comp} channels. Here we can see the expected correspondence between the $\frac{dI}{dV}$ and V_{comp} channels, this time with the alternating orientations of the Fe DL domain structure providing additional contrast (labeled with arrows). Of immediate note is the reversal of contrast between the two images, with the same domain having a high (bright) $\frac{dI}{dV}$ signal, and a low (dark) V_{comp} signal. However, the ML also has a larger average value for $\frac{dI}{dV}$ than the DL, which is the opposite of what was observed using the W tip, e.g. in Figure 4.2. This contrast flip is likely due to an adjustment of the lock-in amplifier phase setting, as a change of 180 degrees will reverse the contrast in a $\frac{dI}{dV}$ image, and will have no effect on the determination of S .

We know from Chapter 2 that the magnitude of σ will be largest when the tip and sample magnetizations are aligned parallel, and smallest for an anti-parallel alignment. Thus, the dark V_{comp} domains in Figure 5.1 correspond to a parallel junction, and the bright domains to an anti-parallel junction. However, as the particular alignment is not necessary for our analysis, we will refer to the domains as bright and dark, with the V_{comp} image in Figure 5.1 as a reference.

5.2 Tip-heating results

The results of heating the tip with the laser can now be presented. Again, this experiment was performed with an equilibrium STM temperature of 50 K, with the Fe DL on W(110) prepared as per Section 3.1.3. The measurement was performed with a bulk Cr tip, implying a fixed tip magnetization that was then scanned over the magnetic domains of the sample. A different tip preparation was used, as compared to Figure 5.1. However, during the course of the measurement no tip changes were evident, and the tip was in tunneling contact for the duration of the experiment.

Analogously to the previous chapter, the average V_{comp} values for Fe DL domains (bright and dark) were used to measure the change in thermovoltage while stepwise increasing the laser heating power. The values for ΔT were found via the linear expansion model described in Section 3.2.3.

The results are shown in Figure 5.2, with values for S extracted via a linear fit V_{comp} versus ΔT . From the previous chapter, we know that the difference in V_{comp} between the domains for $\Delta T = 0$ K can be attributed to AC rectification.

As can be seen, the value of V_{comp} for both domains scales linearly with the generated ΔT . Furthermore, we see a distinct value for S for each domain. This is exactly the signature of magneto-Seebeck tunneling that was

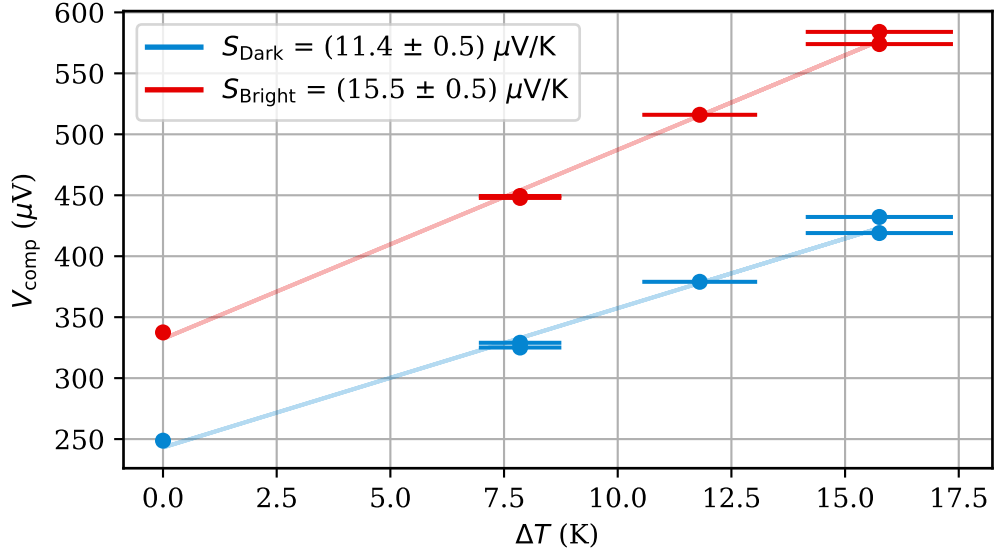


Figure 5.2: Change in V_{comp} for the Fe DL, on the bright and on the dark domains, due to laser heating of the tip. Each dataset has been fitted with a linear function, yielding the values of S shown.

expected, and complies with the prediction of Equation (2.33). With this, we can see that the effect of magneto-Seebeck tunneling applies even on a single-atom scale tunneling junction. The difference between the domains of $4.1 \mu\text{V K}^{-1}$ is reasonable, relative to literature values for planar junctions [22, 98]. The measurement of this effect was the primary goal of this project.

5.3 Seebeck analysis of magnetic domain walls

With the previous tip-heating data, and our explanation for the spectroscopic results, we can again convert an image of V_{rect} into an image of S , and investigate lateral magnetic properties of surface structures. This was done for a section of domain walls on the Fe DL from Figure 5.1, with the results shown in Figure 5.3.

Here the image was converted from V_{comp} to S using the linear conversion from Equation (3.42). We can see that, as with the W tip data, the model of spin-dependent and spin-orbit coupling dependent terms from Equations (3.6) and (3.8) also describes the lateral variation in V_{comp} . Here we equate the tunneling magneto-resistance effect (TMR) to the tunneling magneto-Seebeck effect (TMS), and we introduce the definition of the tunneling anisotropic magneto-Seebeck (TAMS) effect, which is the analog of

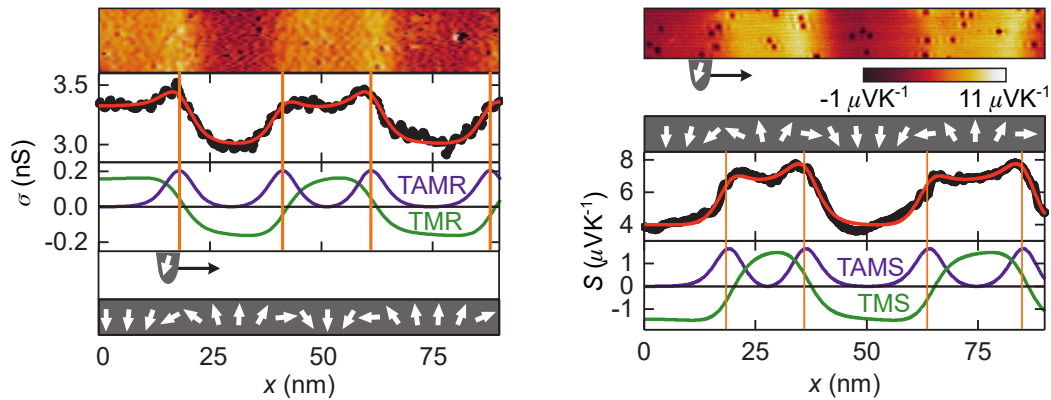


Figure 5.3: (Left, proceeding downwards) STM image of two bright domains and two dark domains, as well as extracted line profile, averaged over the width of the image, fitted with a model of multiple domain walls (locations indicated). The resulting functions for TMR and TAMR contributions are plotted separately, and the fitted phase profile of the sample magnetization is shown. (Right, proceeding downwards) Same domains imaged using σ -STM, linearly converted into a Seebeck image using the experimental parameters: $V_{AC-eff} = 8.5 \text{ mVpk-Pk}$ and $T_{STM} = 50 \text{ K}$. Again, the averaged line profile is shown, fitted by a model of TMR and TAMR contrast, here labeled as tunneling magneto-Seebeck (TMS) and tunneling anisotropic magneto-Seebeck (TAMS) contributions. The lateral profile of the sample magnetization is again indicated.

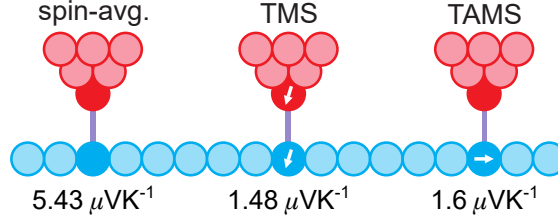


Figure 5.4: Results of fitting a model of TMS and TAMS contrast to a sequence of four magnetic Bloch walls, imaged using σ -STM and converted to values of S using experimental parameters.

the tunneling anisotropic magneto-resistance (TAMR) effect. The fit results are presented in Figure 5.4.

The fitting gives a TMS parameter of $S_{\text{TMS}} = 1.48 \mu\text{V K}^{-1}$, which results in the splitting between the magnetic domains. We also have a TAMS parameter with a value of $S_{\text{TAMS}} = 1.6 \mu\text{V K}^{-1}$. This value however, as with S_{TMS} , is tip-dependent, and so cannot be taken as a definite measure of the Seebeck value for a magnetic domain wall. However, these large values for S_{TMS} and S_{TAMS} support the conclusion that magnetic contributions to S can be of equal or larger magnitude than the observed surface-dependent variations.

5.4 Fe layers on Ir(111)

In order to evaluate the potential resolving power of this technique, a sample of Fe ML/DL on Ir(111) was also imaged using σ -STM. The sample was prepared as per Section 3.1.3, and the measurements were performed with $T_{\text{STM}} = 25.3 \text{ K}$ using a bulk Cr tip. The results of the imaging are shown in Figure 5.5. With the current experimental setup, it was not possible to heat the tip and keep the STM temperature below the minimum needed to maintain the skyrmion lattice. However, as our previous results have shown, predictions for S can still be made based on V_{rect} or bias spectroscopy, and this has been used to convert the V_{comp} data into predicted values of S .

The topographic channel of the STM data is shown in the figure, as the Fe ML lattice contrast was most apparent with this imaging. The square nanoskyrmion lattice (indicated) on the Fe ML can be distinguished, with localized disruptions due to impurities. Near to the step edge to the DL, an intermediate region where the lattice is distorted is also visible.

On the Fe DL, we can see a one-to-one correspondence between the topographic and V_{comp} images. However, an additional contrast pattern is present,

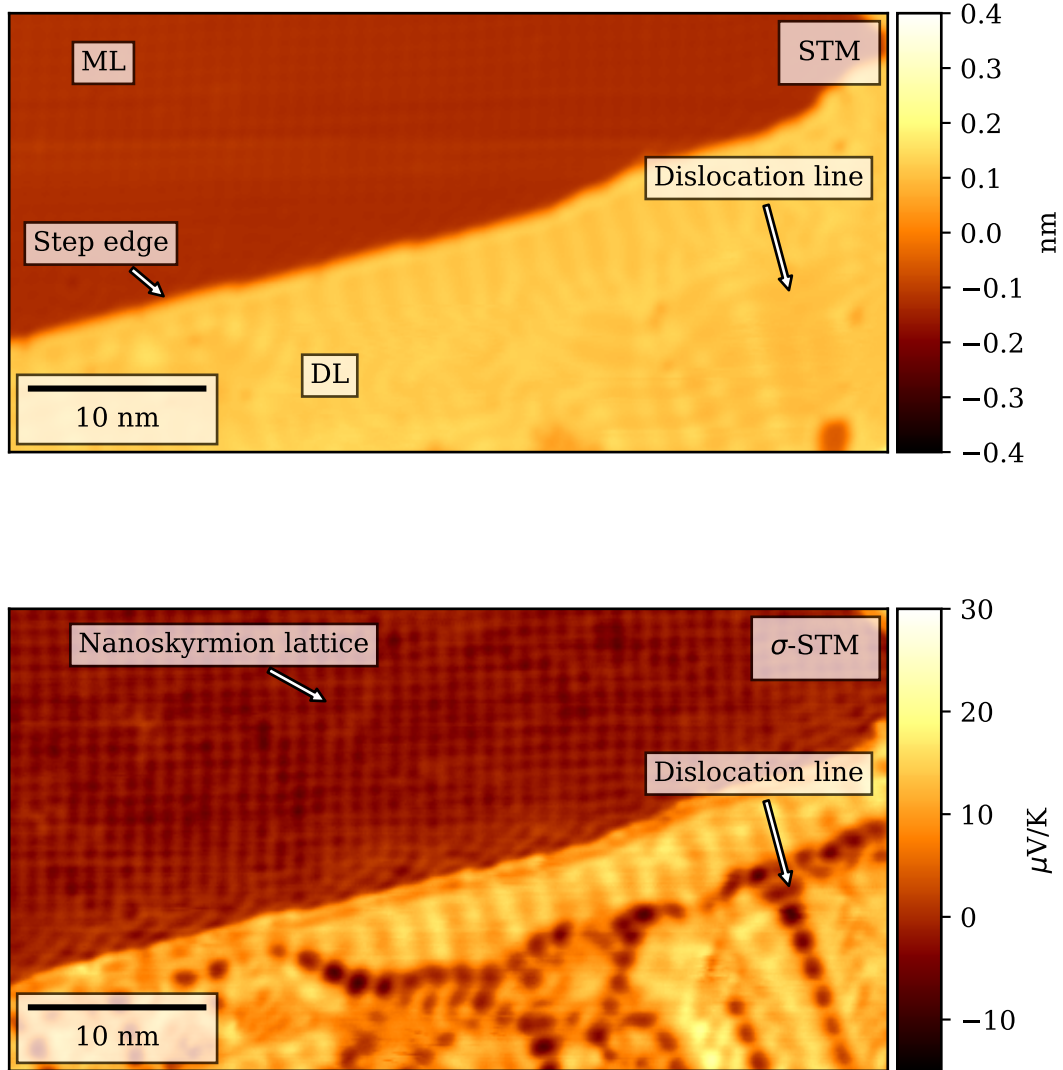


Figure 5.5: (Top) Topographic STM image of the Fe ML and DL on Ir(111), obtained using a Cr tip, with $V = 250$ mV, $I_{\text{set}} = 1$ nA, and $T_{\text{STM}} = 25.37$ K. (Bottom) Same area, imaged using σ -STM, with $V_{\text{AC}} = 10.8$ mV Pk-Pk. Measured values have been converted to predicted Seebeck values using these experimental parameters.

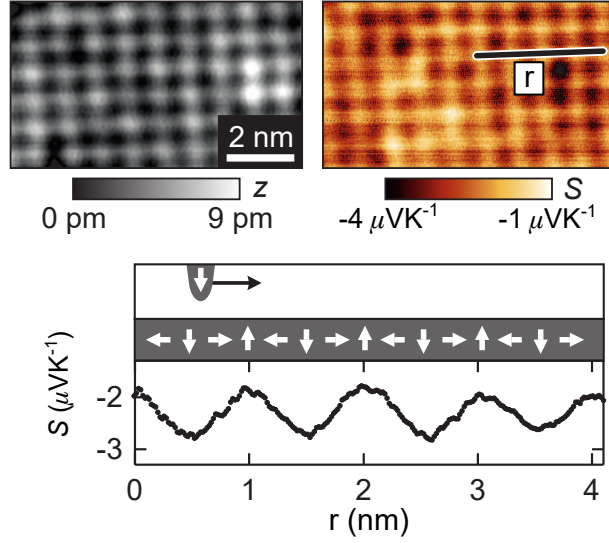


Figure 5.6: (Top) Cropped section of the Fe ML from Figure 5.5, showing the topographic STM data (left) and converted V_{comp} (right) on the same area. (Bottom) Indicated line profile over the Fe ML nanoskyrmion lattice on the S data is plotted, showing a predicted Seebeck modulation of $\approx \pm 0.3 \mu\text{V K}^{-1}$.

with dark nodes appearing along the dislocation lines. Although this could be due to magnetic contrast, a more likely explanation for this dark nodal pattern is a structural disruption shifting the electronic states. This was already observed for the Fe DL on W(110) in previous sections.

In order to highlight the lateral resolution of the σ -STM imaging, Figure 5.6 shows a subsection of the data on the Fe ML. The square lattice is immediately visible in both the topographic and V_{comp} images. A representative line profile for the ML, plotted below, shows that the nanoskyrmion lattice, with a periodicity of 1 nm, is clearly resolved by the imaging. From this, we can predict a peak-to-peak variation of around $0.6 \mu\text{V K}^{-1}$ across the lattice. This demonstrates that σ -STM with a magnetic tip is a viable imaging technique even for sub-nanometer scale magnetic structures.

5.5 Seebeck sensor for spintronics

The nanometer scale resolution of magneto-Seebeck tunneling presented in this chapter has implications for future device applications. As an example, magnetic hard drives now use bit sizes on the scale of a 12 nm by 50 nm [99]. While small, the difference between these elements and the 1 nm periodicity imaged here is a reduction in surface area by two orders of magnitude. This

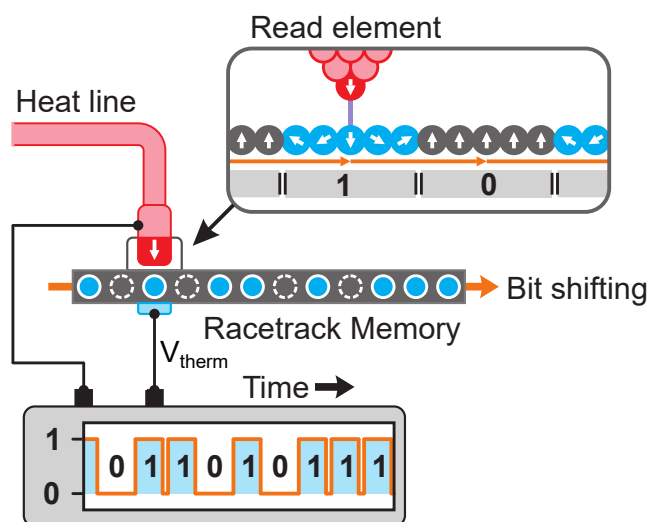


Figure 5.7: Illustration of the proposed use of magneto-Seebeck tunneling as the sensing process for a racetrack memory device. Waste heat from the surrounding device is used to create the necessary temperature differential between the sensor and the racetrack, and the change in V_{comp} as the magnetic elements are moved under the sensor is mapped to binary bits.

implies that next-generation storage technology could use tunneling sensors to manipulate single nanometer scale magnetic structures for reading and writing data.

As an example of this, the concept of a racetrack memory has been proposed [100]. The central idea is that single magnetic elements (bits), e.g. domain walls or skyrmions, are pushed along a track, where the track is narrow enough that the bits form a single line. A stationary sensing/write head then reads/writes the bits as they pass by. This concept is advantageous if the speed at which the bits can be moved and positioned exceeds the mechanical limits of scanning speed for the magnetic sensor.

A key component of this device is the sensor element. We propose that the magneto-Seebeck tunneling effect could be used as a sensor, with the necessary temperature differential between sensor and racetrack being generated using waste heat from the surrounding electronics. This is illustrated in Figure 5.7.

The primary advantage of this approach is that sensing the magnetic state of the junction using Seebeck tunneling avoids any heating of the magnetic bits, e.g. via Joule heating. This becomes increasingly important with decreasing bit sizes, as small magnetic elements are subject to the well-known Néel-Brown law for magnetic particles [58]. This law essentially states that

there exists a temperature above which a previously ferromagnetic particle will begin to flip between parallel and anti-parallel states, relative to its easy axis. This temperature depends on the geometry of the particle, with smaller particles having smaller activation temperatures. Thus, for small magnetic bits, avoiding unnecessary heating becomes critical for the reliability of data storage.

5.6 Summary

In this Chapter measurements of magneto-Seebeck tunneling using an STM were presented. First, the results of scanning the Fe DL on W(110), with its alternating magnetic domains, using a bulk Cr tip and σ -STM were discussed. This clearly demonstrated that magnetic contrast is present using σ -STM, with a direct correspondence to the magnetic structures imaged using conventional spin-polarized STM.

Following this, the result of tip-heating on the Fe DL domains was presented. This resulted in a clearly distinguishable difference between the bright and dark domains, linearly dependent on the temperature difference between the tip and sample. This clear evidence of magneto-Seebeck tunneling is the primary result of this thesis.

This result was then extended down to the single nanometer scale with the observation of resolvable variations in V_{comp} on the nanoskymion lattice of Fe on Ir(111) with a periodicity of approximately 1 nanometer. This resolution was then used as a basis for proposing the use of magneto-Seebeck tunneling as a sensor element for a racetrack memory device, for potential use in next-generation data storage technologies.

Thus, with the presented technique, Seebeck tunneling can be studied in a more quantitative way than previous work, with a lateral resolution equivalent to other STM techniques.

Chapter 6

Conclusion and outlook

In this thesis, we have presented the results of our investigations into the effect of magneto-Seebeck tunneling across a vacuum barrier.

In Chapter 2, the theoretical underpinnings of the work were described, first in the context of a generic planar tunneling junction. This included descriptions of spin-averaged and spin-dependent Seebeck tunneling. The equivalence between the planar derivations and the magnetic tunnel junction created in spin-polarized scanning tunneling microscopy (SP-STM) was detailed.

In Chapter 3, we set out our approach to the measurement of magneto-Seebeck tunneling using an SP-STM apparatus. First the apparatus itself was described, and the examples of the sample systems used later in the work were presented, measured using standard STM techniques. Following this, the necessary modifications and tools needed for the later measurements were discussed. This included measuring the tip-sample potential using the method of scanning tunneling potentiometry, $\sigma - \text{STM}$, and generating a temperature differential across the tunnel junction by heating the STM tip with an external laser. We developed a model of linear thermal expansion in order to extract the temperature change of the tip from the time-resolved tip expansion data, gathered by remaining in tunneling contact while changing the tip heating. Finally, the additional effect of AC rectification was described, and its relevance to the goal of measuring Seebeck tunneling was clarified.

Following these preparatory chapters the results of our investigations were presented, starting in Chapter 4 with spin-averaged data, measured on the Fe double layer (DL) on W(110), using a W tip. This was done in order to precisely quantify the behaviour of the measurement approach, before the added complication of magnetic sensitivity. To start, $\sigma - \text{STM}$ scanning was compared to regular STM scanning, exhibiting a one-to-one correspondence

of topographical and electrical features. With this established, spectroscopic results were used to verify that the significant contrast in potential observed even without tip heating arises from the AC rectification effect. These spectra were also used to predict the Seebeck coefficients for the system. These modeled values were then compared to actual tip heating data, and found to be in good agreement. This supports the approximations necessary for our proposed linear tip expansion heating model, and our derived connection between the magnitude of the AC rectification and the eventual values for S .

Having established the baseline behaviour of the technique, we then moved on to spin-dependent data. This was again measured on the Fe DL on W(110), but using a bulk Cr tip for magnetic sensitivity. The analysis followed that of the spin-averaged data. First the magnetic sensitivity of σ - STM was compared to SP-STM, and again a direct correspondence between magnetic features measured using either approach was found. We then presented direct evidence of a change in tip-sample potential due to a temperature differential across the tunnel junction, that was dependent on the magnetic state of the junction, i.e. magneto-Seebeck tunneling. This observation is the central result of this thesis. We followed this with observations of the nanoskyrmion lattice on Fe on Ir(111) with σ - STM, to show the potential of our approach for investigating S at even smaller scales, which was then used to propose the use of magneto-Seebeck tunneling for sensory applications in a racetrack memory device.

Outlook

The work presented here opens many options for future research. A few promising avenues of inquiry include:

- Different sample systems, with the goal of maximizing the switching contrast.
- Improvements to the measurement technique, including microscopic temperature measurements directly at the tunnel junction.
- Time dependent studies, with the goal of observing thermal spin-transfer torque induced changes to magnetization dynamics.

Taken together, the work described in this thesis lays the groundwork for future investigations into the broader topic of thermal effects in magnetic tunnel junctions.

Bibliography

- [1] T. J. Seebeck. „Magnetische Polarisation Der Metalle Und Erze Durck Temperatur-Differenz, Abh. K“. In: *Akad. Wiss. Berlin* 265 (1823), p. 1823.
- [2] J. C. A. Peltier. „New Experiments on the Heat Effects of Electric Currents“. In: *Ann. Chim. Phys* 56 (1834), pp. 371–386.
- [3] W. Thomson. „Application of Thermodynamics to Dynamic Systems“. In: *Proc. R. Soc. Edinburgh*. 1854, pp. 225–240.
- [4] Sondheimer E. H. and Wilson Alan Herries. „The Kelvin Relations in Thermo-Electricity“. In: *Proceedings of the Royal Society of London. Series A. Mathematical and Physical Sciences* 234.1198 (Feb. 21, 1956), pp. 391–398. DOI: [10/bz78js](https://doi.org/10.1098/rspa.1956.0043). URL: <https://royalsocietypublishing.org/doi/abs/10.1098/rspa.1956.0043> (visited on 07/18/2019).
- [5] Neil W. Ashcroft and N. David Mermin. *Solid State Physics*. Repr. South Melbourne [u.a.]: Brooks/Cole Thomson Learning, 2012. XXI, 826 S. ISBN: 978-0-03-083993-1.
- [6] Robert C. Weast, Melvin J. Astle, and William H. Beyer. *CRC Handbook of Chemistry and Physics*. Vol. 69. CRC press Boca Raton, FL, 1988.
- [7] Frank Pobell. *Matter and Methods at Low Temperatures*. Berlin, Heidelberg: Springer Berlin Heidelberg, 2007. ISBN: 978-3-540-46356-6 978-3-540-46360-3. DOI: [10.1007/978-3-540-46360-3](https://doi.org/10.1007/978-3-540-46360-3). URL: <http://link.springer.com/10.1007/978-3-540-46360-3> (visited on 09/20/2018).
- [8] John C. Slonczewski. „Currents, Torques, and Polarization Factors in Magnetic Tunnel Junctions“. In: *Physical Review B* 71.2 (2005). ISSN: 1098-0121. DOI: [10.1103/PhysRevB.71.024411](https://doi.org/10.1103/PhysRevB.71.024411). URL: <http://journals.aps.org/prb/pdf/10.1103/PhysRevB.71.024411>.

- [9] K. Uchida et al. „Observation of the Spin Seebeck Effect“. In: *Nature* 455.7214 (2008), pp. 778–781. ISSN: 0028-0836. DOI: [10.1038/nature07321](https://doi.org/10.1038/nature07321).
- [10] S.D. Bader and S.S.P. Parkin. „Spintronics“. In: *Annual Review of Condensed Matter Physics* 1.1 (2010), pp. 71–88. DOI: [10/bwn73n](https://doi.org/10.1146/annurev-conmatphys-070909-104123). URL: <https://doi.org/10.1146/annurev-conmatphys-070909-104123> (visited on 07/18/2019).
- [11] Gerrit E. W. Bauer, Eiji Saitoh, and Bart Jan van Wees. „Spin Caloritronics“. In: *Nature Materials* 11.5 (2012), pp. 391–399. ISSN: 1476-1122. DOI: [10.1038/nmat3301](https://doi.org/10.1038/nmat3301).
- [12] J. E. E. Baglin. „Ion Beam Nanoscale Fabrication and Lithography—A Review“. In: *Applied Surface Science*. International Conference on Ion-Beam Induced Nanopatterning of Materials (IINM-2011) 258.9 (Feb. 15, 2012), pp. 4103–4111. ISSN: 0169-4332. DOI: [10/dhxmxc](https://doi.org/10/dhxmxc). URL: <http://www.sciencedirect.com/science/article/pii/S0169433211018320> (visited on 07/19/2019).
- [13] Roland Wiesendanger and Wiesendanger Roland. *Scanning Probe Microscopy and Spectroscopy: Methods and Applications*. Cambridge university press, 1994.
- [14] G. Scheunert et al. „A Review of High Magnetic Moment Thin Films for Microscale and Nanotechnology Applications“. In: *Applied Physics Reviews* 3.1 (Feb. 17, 2016), p. 011301. DOI: [10/gf4778](https://doi.org/10.1063/1.4941311). URL: <https://aip.scitation.org/doi/abs/10.1063/1.4941311> (visited on 07/19/2019).
- [15] Vinod Kumar Joshi. „Spintronics: A Contemporary Review of Emerging Electronics Devices“. In: *Engineering Science and Technology, an International Journal* 19.3 (Sept. 1, 2016), pp. 1503–1513. ISSN: 2215-0986. DOI: [10/gf4394](https://doi.org/10/gf4394). URL: <http://www.sciencedirect.com/science/article/pii/S2215098615300501> (visited on 07/18/2019).
- [16] Jun Hayakawa et al. „Dependence of Giant Tunnel Magnetoresistance of Sputtered CoFeB/MgO/CoFeB Magnetic Tunnel Junctions on MgO Barrier Thickness and Annealing Temperature“. In: *Japanese Journal of Applied Physics* 44 (4L Apr. 22, 2005), p. L587. ISSN: 1347-4065. DOI: [10/fxd4h5](https://doi.org/10/fxd4h5). URL: <https://iopscience.iop.org/article/10.1143/JJAP.44.L587/meta> (visited on 07/19/2019).

- [17] Alexander Boehnke et al. „Time-Resolved Measurement of the Tunnel Magneto-Seebeck Effect in a Single Magnetic Tunnel Junction“. In: *Review of Scientific Instruments* 84.6 (2013), p. 063905. ISSN: 00346748. DOI: [10.1063/1.4811130](https://doi.org/10.1063/1.4811130).
- [18] N. Liebing et al. „Tunneling Magnetothermopower in Magnetic Tunnel Junction Nanopillars“. In: *Physical Review Letters* 107.17 (2011), p. 177201. DOI: [10.1103/PhysRevLett.107.177201](https://doi.org/10.1103/PhysRevLett.107.177201).
- [19] Petro Maksymovych, Simon J. Kelly, and Jorge I. Cerdá. „Surface-State Enhancement of Tunneling Thermopower on the Ag(111) Surface“. In: *ACS Nano* 8.12 (2014), pp. 12110–12119. ISSN: 1936-0851. DOI: [10.1021/nn506123g](https://doi.org/10.1021/nn506123g).
- [20] Jörg Seifritz. „Thermospannung in Der Rastertunnelmikroskopie: Untersuchungen an Homogenen Und Heterogenen Metall- Und Halbleit-eroberflächen“. Doctoral. Essen: Universität GH Essen, 2000.
- [21] C. C. Williams and H. K. Wickramasinghe. „Microscopy of Chemical-Potential Variations on an Atomic Scale“. In: *Nature* 344.6264 (1990), pp. 317–319. ISSN: 0028-0836. DOI: [10.1038/344317a0](https://doi.org/10.1038/344317a0).
- [22] Marvin Walter et al. „Seebeck Effect in Magnetic Tunnel Junctions“. In: *Nature Materials* 10.10 (Oct. 2011), pp. 742–746. ISSN: 1476-1122, 1476-4660. DOI: [10/dpw8q5](https://doi.org/10/dpw8q5). URL: <http://www.nature.com/articles/nmat3076> (visited on 08/15/2018).
- [23] John C. Slonczewski. „Conductance and Exchange Coupling of Two Ferromagnets Separated by a Tunneling Barrier“. In: *Physical Review B* 39.10 (1989), pp. 6995–7002. ISSN: 1098-0121. DOI: [10.1103/PhysRevB.39.6995](https://doi.org/10.1103/PhysRevB.39.6995).
- [24] Alexander Boehnke et al. „On/off Switching of Bit Readout in Bias-Enhanced Tunnel Magneto-Seebeck Effect“. In: *Scientific reports* 5 (2015), p. 8945. ISSN: 2045-2322. DOI: [10.1038/srep08945](https://doi.org/10.1038/srep08945).
- [25] F. L. Bakker et al. „Interplay of Peltier and Seebeck Effects in Nanoscale Nonlocal Spin Valves“. In: *Physical Review Letters* 105.13 (Sept. 24, 2010), p. 136601. DOI: [10/cxbd9w](https://doi.org/10/cxbd9w). URL: <https://link.aps.org/doi/10.1103/PhysRevLett.105.136601> (visited on 07/18/2019).
- [26] Laszlo B. Kish. „Thermal Noise Driven Computing“. In: *Applied Physics Letters* 89.14 (Oct. 2, 2006), p. 144104. ISSN: 0003-6951. DOI: [10/dr39sv](https://doi.org/10/dr39sv). URL: <https://aip.scitation.org/doi/abs/10.1063/1.2359293> (visited on 07/18/2019).

- [27] Abdullah Nazma Nowroz, Ryan Cochran, and Sherief Reda. „Thermal Monitoring of Real Processors: Techniques for Sensor Allocation and Full Characterization“. In: *Proceedings of the 47th Design Automation Conference*. ACM, 2010, pp. 56–61. DOI: [10/d9vfv2](https://doi.org/10/d9vfv2).
- [28] S. Lee et al. „Thermoelectric-Based Sustainable Self-Cooling for Fine-Grained Processor Hot Spots“. In: *2016 15th IEEE Intersociety Conference on Thermal and Thermomechanical Phenomena in Electronic Systems (ITherm)*. 2016 15th IEEE Intersociety Conference on Thermal and Thermomechanical Phenomena in Electronic Systems (ITherm). May 2016, pp. 847–856. DOI: [10/gf4397](https://doi.org/10/gf4397).
- [29] Marvin Walter. „The Tunnel Magneto-Seebeck Effect in Magnetic Tunnel Junctions“. Doctoral. Göttingen: Universität Göttingen, 2013.
- [30] Torsten Huebner et al. „Comparison of Laser-Induced and Intrinsic Tunnel Magneto-Seebeck Effect in CoFeB/MgAl₂O₄ and CoFeB/MgO Magnetic Tunnel Junctions“. In: *Physical Review B* 93.22 (2016). ISSN: 1098-0121. DOI: [10.1103/PhysRevB.93.224433](https://doi.org/10.1103/PhysRevB.93.224433).
- [31] C. C. Williams and H. K. Wickramasinghe. „Scanning Thermal Profiler“. In: *Applied Physics Letters* 49.23 (1986), p. 1587. ISSN: 00036951. DOI: [10.1063/1.97288](https://doi.org/10.1063/1.97288).
- [32] D. Hoffmann et al. „Thermovoltage in Scanning Tunneling Microscopy“. In: *Journal of Electron Spectroscopy and Related Phenomena* 109.1-2 (2000), pp. 117–125. ISSN: 03682048. DOI: [10.1016/S0368-2048\(00\)00111-0](https://doi.org/10.1016/S0368-2048(00)00111-0).
- [33] D. Hoffmann et al. „Thermovoltages in Vacuum Tunneling Investigated by Scanning Tunneling Microscopy“. In: *Thin Solid Films* 264.2 (1995), pp. 223–225. ISSN: 00406090. DOI: [10.1016/0040-6090\(95\)05844-3](https://doi.org/10.1016/0040-6090(95)05844-3).
- [34] D. Hoffmann et al. „Thermovoltage across a Vacuum Barrier Investigated by Scanning Tunneling Microscopy: Imaging of Standing Electron Waves“. In: *Physical Review B* 52.19 (1995).
- [35] R. Wiesendanger et al. „Observation of Vacuum Tunneling of Spin-Polarized Electrons with the Scanning Tunneling Microscope“. In: *Physical Review Letters* 65.2 (July 9, 1990), pp. 247–250. DOI: [10/c728km](https://doi.org/10/c728km). URL: <https://link.aps.org/doi/10.1103/PhysRevLett.65.247> (visited on 07/19/2019).
- [36] P. Murali and D. W. Pohl. „Scanning Tunneling Potentiometry“. In: *Applied Physics Letters* 48.8 (1986), p. 514. ISSN: 00036951. DOI: [10.1063/1.96491](https://doi.org/10.1063/1.96491).

- [37] S. Krause et al. „Current-Induced Magnetization Switching with a Spin-Polarized Scanning Tunneling Microscope“. In: *Science* 317.5844 (Sept. 14, 2007), pp. 1537–1540. ISSN: 0036-8075, 1095-9203. DOI: [10/b7bxkv](https://doi.org/10.1126/science.1145336). URL: <http://www.sciencemag.org/cgi/doi/10.1126/science.1145336> (visited on 09/19/2018).
- [38] J. Bardeen. „Tunnelling from a Many-Particle Point of View“. In: *Physical Review Letters* 6.2 (Jan. 15, 1961), pp. 57–59. ISSN: 0031-9007. DOI: [10/dc49w5](https://doi.org/10.1103/PhysRevLett.6.57). URL: <https://link.aps.org/doi/10.1103/PhysRevLett.6.57> (visited on 08/14/2018).
- [39] C. Julian Chen. *Introduction to Scanning Tunneling Microscopy*. Oxford University Press, 1993. 469 pp. ISBN: 978-0-19-507150-4.
- [40] J. A. Stroscio and P. Lipavský. „Thermopower in Scanning-Tunneling-Microscope Experiments“. In: *Physical Review B* 42.14 (Nov. 15, 1990), pp. 9214–9216. ISSN: 0163-1829, 1095-3795. DOI: [10/dvh7hh](https://doi.org/10.1103/PhysRevB.42.9214). URL: <https://link.aps.org/doi/10.1103/PhysRevB.42.9214> (visited on 08/25/2018).
- [41] M. Julliere. „Tunneling between Ferromagnetic Films“. In: *Physics Letters A* 54.3 (Sept. 8, 1975), pp. 225–226. ISSN: 0375-9601. DOI: [10/crznw9](https://doi.org/10.1016/0375-9601(75)90174-7). URL: <http://www.sciencedirect.com/science/article/pii/0375960175901747> (visited on 08/25/2018).
- [42] H. J. Reittu. „Fermi’s Golden Rule and Bardeen’s Tunneling Theory“. In: *American Journal of Physics* 63.10 (Oct. 1, 1995), pp. 940–944. ISSN: 0002-9505. DOI: [10/dcxdfx](https://doi.org/10.1119/1.18037). URL: <https://aapt.scitation.org/doi/10.1119/1.18037> (visited on 08/14/2018).
- [43] Roland Wiesendanger. *Scanning Probe Microscopy and Spectroscopy: Methods and Applications*. Cambridge University Press, Sept. 29, 1994. 664 pp. ISBN: 978-0-521-42847-7.
- [44] Stefan Krause et al. „Magnetization Reversal of Nanoscale Islands“. In: *Physical Review Letters* 103.12 (2009). ISSN: 0031-9007. DOI: [10.1103/PhysRevLett.103.127202](https://doi.org/10.1103/PhysRevLett.103.127202).
- [45] André Kubetzka. „Spinpolarisierte Rastertunnelmikroskopie an Magnetischen Nanostrukturen: Fe/W (110)“. 2002.
- [46] M. Bode et al. „Spin-Polarized Scanning Tunneling Spectroscopy of Dislocation Lines in Fe Films on W(110)“. In: *Journal of Magnetism and Magnetic Materials* 304.1 (2006), pp. 1–5. ISSN: 03048853. DOI: [10.1016/j.jmmm.2006.02.098](https://doi.org/10.1016/j.jmmm.2006.02.098).
- [47] Anika Schlenhoff. „Imaging and Switching Individual Nanomagnets with SP-SFEM“. Doctoral. Hamburg: University of Hamburg, 2013.

- [48] Torben Hänke. „A New Variable-Temperature Scanning Tunneling Microscope and Temperature-Dependent Spin-Polarized Scanning Tunneling Spectroscopy on the Cr(001) Surface“. Doctoral. Hamburg: Universität Hamburg, 2005. URL: <http://ediss.sub.uni-hamburg.de/volltexte/2006/2885/>.
- [49] *MACOR Machinable Glass Ceramic | High Temperature Machinable Glass Ceramic | Corning*. URL: <https://www.corning.com/worldwide/en/products/advanced-optics/product-materials/specialty-glass-and-glass-ceramics/glass-ceramics/macor.html> (visited on 09/05/2018).
- [50] C. Benjamin Nakhosteen and Karl Jousten. *Handbook of Vacuum Technology*. John Wiley & Sons, 2016.
- [51] David J. Griffiths. *Introduction to Electrodynamics*. AAPT, 2005.
- [52] Henry A. Sodano and Jae-Sung Bae. „Eddy Current Damping in Structures“. In: *Shock and Vibration Digest* 36.6 (2004), p. 469. DOI: [10/fbbgfk](https://doi.org/10/fbbgfk).
- [53] *Nanonis Products - Nanonis SPM Controller - Control Omicron-, JEOL-, RHK- and Many Other Microscopes*. URL: <http://www.specs-zurich.com/en/SPM-Control-System-Base-Package.html> (visited on 09/05/2018).
- [54] *Current Amplifiers: Variable Gain up to 500 kHz - DLPCA - Femto*. URL: <https://www.femto.de/en/products/current-amplifiers/variable-gain-up-to-500-khz-dlpc.html> (visited on 09/05/2018).
- [55] Inger Ekvall et al. „Preparation and Characterization of Electrochemically Etched W Tips for STM“. In: *Measurement Science and Technology* 10.1 (Jan. 1, 1999), pp. 11–18. ISSN: 0957-0233, 1361-6501. DOI: [10.1088/0957-0233/10/1/006](https://doi.org/10.1088/0957-0233/10/1/006).
- [56] A. M. Horgan and D. A. King. „Oxygen Adsorption, Reconstruction, and Thin Oxide Film Formation on Clean Metal Surfaces: Ni, Fe, W and Mo“. In: *Surface Science* 23.2 (Nov. 1, 1970), pp. 259–282. ISSN: 0039-6028. DOI: [10/cvdq99](https://doi.org/10/cvdq99). URL: <http://www.sciencedirect.com/science/article/pii/0039602870901524> (visited on 08/06/2019).
- [57] M. Bode et al. „On the Preparation and Electronic Properties of Clean W(110) Surfaces“. In: *Surface Science* 601.16 (2007), pp. 3308–3314. ISSN: 00396028. DOI: [10.1016/j.susc.2007.06.017](https://doi.org/10.1016/j.susc.2007.06.017).

- [58] William Fuller Brown. „Thermal Fluctuations of a Single-Domain Particle“. In: *Physical Review* 130.5 (June 1, 1963), pp. 1677–1686. ISSN: 0031-899X. DOI: [10/dq6w7z](https://doi.org/10.1103/PhysRev.130.1677). URL: <https://link.aps.org/doi/10.1103/PhysRev.130.1677> (visited on 09/19/2018).
- [59] A. Schlenhoff et al. „Bulk Cr Tips with Full Spatial Magnetic Sensitivity for Spin-Polarized Scanning Tunneling Microscopy“. In: *Applied Physics Letters* 97.8 (Aug. 23, 2010), p. 083104. ISSN: 0003-6951. DOI: [10/b4gfwj](https://doi.org/10.1063/1.3474659). URL: <https://aip.scitation.org/doi/abs/10.1063/1.3474659> (visited on 09/17/2018).
- [60] F. Donati et al. „Electronic and Magnetic Properties of Bulk Cr Tips for Scanning Tunneling Spectroscopy“. In: *Physical Review B* 87.23 (2013). ISSN: 1098-0121. DOI: [10.1103/PhysRevB.87.235431](https://doi.org/10.1103/PhysRevB.87.235431).
- [61] Marco Corbetta et al. „Magnetic Response and Spin Polarization of Bulk Cr Tips for In-Field Spin-Polarized Scanning Tunneling Microscopy“. In: *Japanese Journal of Applied Physics* 51 (2012), p. 030208. ISSN: 0021-4922. DOI: [10.1143/JJAP.51.030208](https://doi.org/10.1143/JJAP.51.030208).
- [62] A. Li Bassi et al. „Bulk Cr Tips for Scanning Tunneling Microscopy and Spin-Polarized Scanning Tunneling Microscopy“. In: *Applied Physics Letters* 91.17 (Oct. 22, 2007), p. 173120. ISSN: 0003-6951. DOI: [10/c46qhb](https://doi.org/10.1063/1.2800810). URL: <https://aip.scitation.org/doi/abs/10.1063/1.2800810> (visited on 08/06/2019).
- [63] A. Kubetzka et al. „Spin-Polarized Scanning Tunneling Microscopy Study of 360° Walls in an External Magnetic Field“. In: *Physical Review B* 67.2 (2003). ISSN: 1098-0121. DOI: [10.1103/PhysRevB.67.020401](https://doi.org/10.1103/PhysRevB.67.020401).
- [64] P. L. Walker Jr, R. L. Taylor, and J. M. Ranish. „An Update on the Carbon-Oxygen Reaction“. In: *Carbon* 29.3 (1991), pp. 411–421. DOI: [10/b6g29h](https://doi.org/10.1016/0008-6223(91)90299-3).
- [65] H. Bethge et al. „Misfit-Related Effects in the Epitaxial Growth of Iron on W(110)“. In: *Surface Science* 331-333 (1995), pp. 878–884. ISSN: 00396028. DOI: [10.1016/0039-6028\(95\)00166-2](https://doi.org/10.1016/0039-6028(95)00166-2).
- [66] U. Gradmann and G. Waller. „Periodic Lattice Distortions in Epitaxial Films of Fe(110) on W(110)“. In: *Surface Science* 116.3 (1982), pp. 539–548. ISSN: 00396028. DOI: [10.1016/0039-6028\(82\)90363-6](https://doi.org/10.1016/0039-6028(82)90363-6).
- [67] K. von Bergmann et al. „Tunneling Anisotropic Magnetoresistance on the Atomic Scale“. In: *Physical Review B* 86.13 (Oct. 24, 2012). ISSN: 1098-0121, 1550-235X. DOI: [10/gd4tfs](https://doi.org/10.1103/PhysRevB.86.134422). URL: <https://link.aps.org/doi/10.1103/PhysRevB.86.134422> (visited on 09/04/2018).

- [68] M. Heide, G. Bihlmayer, and S. Blügel. „Dzyaloshinskii-Moriya Interaction Accounting for the Orientation of Magnetic Domains in Ultrathin Films: Fe/W(110)“. In: *Physical Review B* 78.14 (Oct. 15, 2008), p. 140403. DOI: [10/fc6nhn](https://doi.org/10.1103/PhysRevB.78.140403). URL: <https://link.aps.org/doi/10.1103/PhysRevB.78.140403> (visited on 08/27/2019).
- [69] LN Bulaevskii and VL Ginzburg. „Temperature Dependence of the Shape of the Domain Wall in Ferromagnetics and Ferroelectrics“. In: *Soviet Physics JETP* 18.530 (1964), p. 5.
- [70] W. Weber et al. „Enhancement of the Curie Temperature of Epitaxial Fe Films on W(110) Caused by Adsorption of Submonolayers of Fe, Pd, Ag, and O“. In: *Physical Review Letters* 65.16 (Oct. 15, 1990), pp. 2058–2061. ISSN: 0031-9007. DOI: [10/c8tgq8](https://doi.org/10.1103/PhysRevLett.65.2058). URL: <https://link.aps.org/doi/10.1103/PhysRevLett.65.2058> (visited on 09/17/2018).
- [71] Kirsten von Bergmann et al. „Complex Magnetism of the Fe Monolayer on Ir(111)“. In: *New Journal of Physics* 9.10 (Oct. 2007), pp. 396–396. ISSN: 1367-2630. DOI: [10.1088/1367-2630/9/10/396](https://doi.org/10.1088/1367-2630/9/10/396). URL: <https://doi.org/10.1088/1367-2630/9/10/396> (visited on 08/05/2019).
- [72] Pin-Jui Hsu et al. „Guiding Spin Spirals by Local Uniaxial Strain Relief“. In: *Physical Review Letters* 116.1 (Jan. 5, 2016), p. 017201. DOI: [10/gf5sjk](https://doi.org/10.1103/PhysRevLett.116.017201). URL: <https://link.aps.org/doi/10.1103/PhysRevLett.116.017201> (visited on 08/05/2019).
- [73] Pin-Jui Hsu et al. „Inducing Skyrmions in Ultrathin Fe Films by Hydrogen Exposure“. In: *Nature Communications* 9.1 (Dec. 2018). ISSN: 2041-1723. DOI: [10/gdh39b](https://doi.org/10.1038/s41467-018-04015-z). URL: <http://www.nature.com/articles/s41467-018-04015-z> (visited on 08/05/2019).
- [74] Daniel V. Schroeder. *An Introduction to Thermal Physics*. AAPT, 1999.
- [75] Michael F. Modest. *Radiative Heat Transfer*. Academic Press, Feb. 20, 2013. 905 pp. ISBN: 978-0-12-386990-6.
- [76] William M. Haynes. *CRC Handbook of Chemistry and Physics, 92nd Edition*. CRC Press, June 6, 2011. 2624 pp. ISBN: 978-1-4398-5512-6.
- [77] Edward A. Estalote and K. G. Ramanathan. „Low-Temperature Emissivities of Copper and Aluminum“. In: *JOSA* 67.1 (Jan. 1, 1977), pp. 39–44. DOI: [10/bmrpqr](https://doi.org/10.1063/josa.1977.67.1.39). URL: <https://www.osapublishing.org/josa/abstract.cfm?uri=josa-67-1-39> (visited on 10/10/2018).

- [78] Aaron Meurer et al. „SymPy: Symbolic Computing in Python“. In: *PeerJ Computer Science* 3 (Jan. 2, 2017), e103. ISSN: 2376-5992. DOI: [10/gfb682](https://doi.org/10/gfb682). URL: <https://peerj.com/articles/cs-103> (visited on 10/10/2018).
- [79] Travis E. Oliphant. „Python for Scientific Computing“. In: *Computing in Science & Engineering* 9.3 (May 1, 2007), pp. 10–20. ISSN: 1521-9615. DOI: [10/fjzzc8](https://doi.org/10/fjzzc8). URL: <https://aip.scitation.org/doi/abs/10.1109/MCSE.2007.58> (visited on 10/10/2018).
- [80] Stefan Grafström. „Photoassisted Scanning Tunneling Microscopy“. In: *Journal of Applied Physics* 91.4 (2002), p. 1717. ISSN: 00218979. DOI: [10.1063/1.1432113](https://doi.org/10.1063/1.1432113).
- [81] K. Sotthewes, M. H. Siekman, and H. J. W. Zandvliet. „A Method to Measure the Thermovoltage with a High Spatial Resolution“. In: *Applied Physics Letters* 108.14 (2016), p. 141601. ISSN: 00036951. DOI: [10.1063/1.4945665](https://doi.org/10.1063/1.4945665).
- [82] Cody Friesen et al. „Scanning Seebeck Tunneling Microscopy“. In: *Journal of Physics D: Applied Physics* 51.32 (2018), p. 324001. ISSN: 0022-3727. DOI: [10.1088/1361-6463/aacfab](https://doi.org/10.1088/1361-6463/aacfab).
- [83] Hermann Osterhage. „Calorimetric Experiments on Fe/W(110) Using Scanning Tunneling Microscopy“. Master. Hamburg: University of Hamburg, Nov. 2016. 85 pp.
- [84] Y. S. Touloukian and D. P. DeWitt. *Thermophysical Properties of Matter - The TPRC Data Series. Volume 7. Thermal Radiative Properties - Metallic Elements and Alloys*. Thermophysical and Electronic Properties Information Analysis Center Lafayette, Jan. 1970. URL: <http://www.dtic.mil/docs/citations/ADA951941> (visited on 09/29/2018).
- [85] G. K. White, R. B. Roberts, and E. Fawcett. „Thermal Expansion of Cr and CrV Alloys. I. Experiment“. In: *Journal of Physics F: Metal Physics* 16.4 (1986), pp. 449–459. ISSN: 0305-4608. DOI: [10.1088/0305-4608/16/4/009](https://doi.org/10.1088/0305-4608/16/4/009).
- [86] E Marquardt, J Le, and Ray Radebaugh. „11th International Cryocooler Conference June 20–22, 2000 Keystone, Co“. In: *Cryogenic Material Properties Database, National Institute of Standards and Technology Boulder, CO 80303* ().
- [87] Sookyung H. Park et al. „Laser-Induced Thermoelectric Effects in an STM Junction“. In: *Surface Science* 266.1-3 (1992), pp. 265–273. ISSN: 00396028. DOI: [10.1016/0039-6028\(92\)91031-6](https://doi.org/10.1016/0039-6028(92)91031-6).

- [88] Petro Maksymovych. „Distance Dependence of Tunneling Thermovoltage on Metal Surfaces“. In: *Journal of Vacuum Science & Technology B: Microelectronics and Nanometer Structures* 31.3 (2013), p. 031804. ISSN: 21662746. DOI: [10.1116/1.4803156](https://doi.org/10.1116/1.4803156).
- [89] N. Liebing et al. „Determination of Spin-Dependent Seebeck Coefficients of CoFeB/MgO/CoFeB Magnetic Tunnel Junction Nanopillars“. In: *Journal of Applied Physics* 111.7 (2012), p. 07C520. ISSN: 00218979. DOI: [10.1063/1.3679769](https://doi.org/10.1063/1.3679769).
- [90] A. Bannani, C. A. Bobisch, and R. Möller. „Local Potentiometry Using a Multiprobe Scanning Tunneling Microscope“. In: *Review of Scientific Instruments* 79.8 (Aug. 1, 2008), p. 083704. ISSN: 0034-6748. DOI: [10/fttr256](https://doi.org/10.1063/1.2968111). URL: <https://aip.scitation.org/doi/abs/10.1063/1.2968111> (visited on 08/06/2019).
- [91] Roland Wiesendanger. *Scanning Probe Microscopy and Spectroscopy*. Cambridge University Press, 1994.
- [92] R J Hamers. „Atomic-Resolution Surface Spectroscopy with the Scanning Tunneling Microscope“. In: *Annual Review of Physical Chemistry* 40.1 (Oct. 1989), pp. 531–559. ISSN: 0066-426X, 1545-1593. DOI: [10/ftthqk](https://doi.org/10.1146/annurev.pc.40.100189.002531). URL: <http://www.annualreviews.org/doi/10.1146/annurev.pc.40.100189.002531> (visited on 10/13/2018).
- [93] H. Q. Nguyen et al. „Mechanisms of Current Rectification in an STM Tunnel Junction and the Measurement of an Operational Tunneling Time“. In: *IEEE Transactions on Electron Devices* 36.11 (1989), pp. 2671–2678. ISSN: 00189383. DOI: [10.1109/16.43771](https://doi.org/10.1109/16.43771).
- [94] U. Kemiktarak et al. „Radio-Frequency Scanning Tunnelling Microscopy“. In: *Nature* 450.7166 (Nov. 2007), pp. 85–88. ISSN: 1476-4687. DOI: [10/bvns58](https://doi.org/10.1038/nature06238). URL: <https://www.nature.com/articles/nature06238> (visited on 08/06/2019).
- [95] W. F. Brinkman. „Tunneling Conductance of Asymmetrical Barriers“. In: *Journal of Applied Physics* 41.5 (1970), p. 1915. ISSN: 00218979. DOI: [10.1063/1.1659141](https://doi.org/10.1063/1.1659141).
- [96] H. J. Elmers et al. „Magnetic Frustration in Ultrathin Fe Films“. In: *Physical Review Letters* 75.10 (Sept. 4, 1995), pp. 2031–2034. DOI: [10/fkj8nd](https://doi.org/10.1103/PhysRevLett.75.2031). URL: <https://link.aps.org/doi/10.1103/PhysRevLett.75.2031> (visited on 05/13/2019).

-
- [97] A.A. Minakov and I.V. Shvets. „On the Possibility of Resolving Quantization Axes of Surface Spins by Means of a Scanning Tunneling Microscope with a Magnetic Tip“. In: *Surface Science* 236.3 (Oct. 1990), pp. L377–L381. ISSN: 00396028. DOI: [10/bgbkcb](https://doi.org/10/bgbkcb). URL: <https://linkinghub.elsevier.com/retrieve/pii/003960289090468N> (visited on 05/13/2019).
- [98] Christian Heiliger, Christian Franz, and Michael Czerner. „Ab Initio Studies of the Tunneling Magneto-Seebeck Effect“. In: *Physical Review B* 87.22 (2013). ISSN: 1098-0121. DOI: [10.1103/PhysRevB.87.224412](https://doi.org/10.1103/PhysRevB.87.224412).
- [99] Clint Ludeman. *How Helium Powers Our New Generation of 14TB HDDs*. Dec. 12, 2018. URL: <https://blog.westerndigital.com/new-generation-14tb-hard-drives/> (visited on 08/12/2019).
- [100] Stuart S. P. Parkin, Masamitsu Hayashi, and Luc Thomas. „Magnetic Domain-Wall Racetrack Memory“. In: *Science* 320.5873 (Apr. 11, 2008), pp. 190–194. ISSN: 0036-8075, 1095-9203. DOI: [10/bpzg6k](https://doi.org/10/bpzg6k). pmid: [18403702](https://pubmed.ncbi.nlm.nih.gov/18403702/). URL: <https://science.sciencemag.org/content/320/5873/190> (visited on 08/12/2019).

Appendix A

Equilibrium temperature modeling

This section contains supporting information for the modeling of equilibrium temperatures, considering a system of thermal elements coupled via direct heat conduction and thermal radiation. The sample temperature was considered as fixed to that of the STM body, and the STM body temperature is directly measured during the experiment. Thus the only temperatures that are free to vary are that of the tip and of the heat shield. It will thus be sufficient to calculate the thermal connections only for these two elements.

A.1 Heat shield

As stated in Chapter 3, the heat shield will be assumed to be a homogeneous thermal element. Although large thermal gradients may exist in the shield, especially in the region of the connection between the shield and heat exchanger braid, this assumption is sufficient for the purpose of the modeling, which is to establish an approximate temperature range for the thermal elements.

A.1.1 Heat shield - UHV chamber

For $\dot{Q}_{\text{rad(HS-UHV)}}$, we assume a geometry of nested cylinders of equal length, but different radii. The view factor for this situation is symmetric for the two cylinders, and has the form [75]

$$F_{A-B} = \frac{1}{R} \left[1 - \frac{H^2 + R^2 - 1}{4H} - \frac{1}{\pi} \left(\cos^{-1} \frac{H^2 - R^2 + 1}{H^2 + R^2 - 1} - \frac{\sqrt{(H^2 + R^2 + 1)^2 - 4R^2}}{2H} \cos^{-1} \frac{H^2 - R^2 + 1}{R(H^2 + R^2 - 1)} - \frac{H^2 - R^2 + 1}{2H} \sin^{-1} \frac{1}{R} \right) \right], \quad (\text{A.1})$$

where $R = \frac{r_A}{r_B}$ and $H = \frac{h}{r_B}$. With $r_{\text{UHV}} = 10.5$ cm, $r_{\text{HS}} = 3$ cm, and $h = 10$ cm, we have $F_{\text{UHV-HS}} = 0.05$ and $F_{\text{HS-UHV}} = 0.5$.

A.1.2 Heat shield - Heat exchanger

The connection between the heat shield and the heat exchanger is via a copper braid, and assumed to be purely diffusive. We will approximate the braid as having the same temperature as that of the heat exchanger. The braid consists of 800 copper cables with a combined cross-section of 1.57 mm^2 , and a cable length of 20 cm. Assuming a thermal conductivity for copper of $\kappa_{\text{Cu}} = 30 \text{ W/m}^2\text{K}$, for a heat exchanger temperature of $T_{\text{Hex}} = 35 \text{ K}$, the thermal conductance between heat shield and the heat exchanger will be $k_{\text{HS-Hex}} = 3.1 \text{ mW K}^{-1}$ [76].

A.1.3 Heat shield - STM body

For the radiative heat transfer, we have again applied a nested cylinder geometry as per Equation (A.1). Although there are some intervening elements, namely the steel supporting rods, they are of a thickness such that the majority of the STM body is still exposed to the heat shield.

Applying this approach, with $r_{\text{HS}} = 3$ cm, $h_{\text{HS}} = 10$ cm, $r_{\text{STM}} = 1.6$ cm, and height $h_{\text{STM}} = 5$ cm, we have $F_{\text{HS-STM}} = 0.27$ and $F_{\text{STM-HS}} = 1$. This is assuming negligible radiative transfer between the STM body and the sample and tip.

The mechanical contact between the heat shield and the STM is via a series of steel rods and plates, as well as three ruby balls. Assuming material temperatures of 50 K, we have used $k_{\text{rods}} = 0.93 \text{ mW K}^{-1}$, $k_{\text{plate}} = 0.3 \text{ mW K}^{-1}$, and $k_{\text{ruby}} = 188 \text{ mW K}^{-1}$.

A.1.4 Heat shield - Tip

The tip can be approximated as a small plane, with an area of 10 mm^2 . This plane will see a reduced area of the inner heat shield surface, via the front opening of the STM. We will approximate this viewable region as circular. From the known geometry of the STM, the approximate area of the heat shield seen by the tip will be 7.5 cm^2 . The view factor relation for an area element normally situated along the central axis of a circular element is [75]

$$F_{\text{area-circle}} = \frac{A}{\left(\frac{h}{r}\right)^2 + 1}, \quad (\text{A.2})$$

where A is the area of the planar element, h is the separation between the planar element and the circular element, and r is the radius of the circular element. With the stated dimensions here and in Figure 3.13, we have $F_{\text{HS-Tip}} = 0.002$ and $F_{\text{Tip-HS}} = 0.16$.

A.2 Tip

As the radiative connection between the tip and the heat shield has already been described, there remains only the connection between the tip and the STM body to describe.

A.2.1 Tip - STM body

For the radiative coupling, as the view factor between the tip and the heat shield has been described, and the convex shape of the tip prevents any self-heating, we can simply assume that $F_{\text{Tip-STM}} = 1 - F_{\text{Tip-HS}} = 0.84$.

Mechanically, we can add up the contributions to the thermal conductance in series. The contact conductance at each interface was assumed to be much greater than that of any of the elements, and so was neglected. For material constants, we use the values in Table A.1.

Material	κ (W/mmK)
Macor	0.00146 [76]
Sapphire	9 [75]
W (150 K)	4 [75]

Table A.1: Thermal conductivities of materials used for modeling the thermal conductance between the tip and the STM body. The temperature is assumed to be 50 K.

The series of connecting elements was as follows: the tip holder, the top macor bushing, the piezo-scanning tube, the bottom macor bushing, the sapphire prism, and the six coarse-drive piezo stacks. Taken together, the total thermal conductance between the tip and the STM body was taken to be $k_{\text{Tip-STM}} = 848 \mu\text{W K}^{-1}$.

Appendix B

Uncompensated tunneling current

An additional correction has been applied to the measured values of V_{comp} , to correct for the settling time of the bias feedback loop. Here we define settling time as the time required for the feedback loop to find the new correct compensation voltage, if the tip-sample potential is changed. In general this will depend on the specific implementation of the feedback controller, as well as the change in potential.

Until the correct compensation value is found however, there will be a net tunneling current across the junction. If the tip is being scanned too fast, such that the bias has insufficient time to settle, then the recorded value for V_{comp} will be incorrect. To quantify this, assuming small biases, we can define an error signal, ΔV , as

$$\Delta V = V_{\text{ideal}} - V_{\text{comp}} , \quad (\text{B.1})$$

where the ideal compensation voltage V_{ideal} is defined such that

$$\sigma V_{\text{ideal}} = I = 0 . \quad (\text{B.2})$$

This error signal will lead to the previously mentioned undesired tunneling current:

$$I_{\text{error}} = \sigma \Delta V , \quad (\text{B.3})$$

with I_{error} being the difference between the actual tunneling current and the setpoint for the feedback loop (here $I_{\text{set}} = 0$):

$$I_{\text{error}} = I - I_{\text{set}} . \quad (\text{B.4})$$

To see how to recover the ideal tip-sample potential then, we can substitute Equation (B.3) into Equation (B.1), giving

$$V_{\text{ideal}} = \frac{I_{\text{error}}}{\sigma} + V_{\text{comp}} . \quad (\text{B.5})$$

Experimentally, this requires simultaneously recording the tunneling current and conductance, while performing the σ – STM measurements. We can then recover the information by point-wise combining the I , $\frac{dI}{dV}$, and V_{comp} images according to Equation (B.5). This is illustrated in Figure B.1.

We can see that $|I_{\text{error}}|$ is largest where the value of V_{comp} varies rapidly (e.g. single impurities and step edges), which matches our expectation for a finite settling time. In the limit of much slower scanning, we would expect these deviations decreasing to zero.

In the correction image ΔV we can see that variations on the scale of $100 \mu\text{V}$ are present, specifically at the location of impurities. We see that the average value for ΔV is approximately zero, and indeed the change in mean value between V_{comp} and ΔV is less than $1 \mu\text{V}$. However, the correction is useful if information about small structures with faster scanning speeds is required.

It should be noted that this correction can also be applied if no bias compensation was used, i.e. $V_{\text{comp}} = 0$. In this way, only the I_{error} and $\frac{dI}{dV}$ images are needed to measured V_{ideal} . This is useful if, for example, the requisite software or hardware for implementing the bias feedback is not available for a particular microscope. However, this is subject to errors in two measurements, making it less accurate than directly applying V_{comp} .

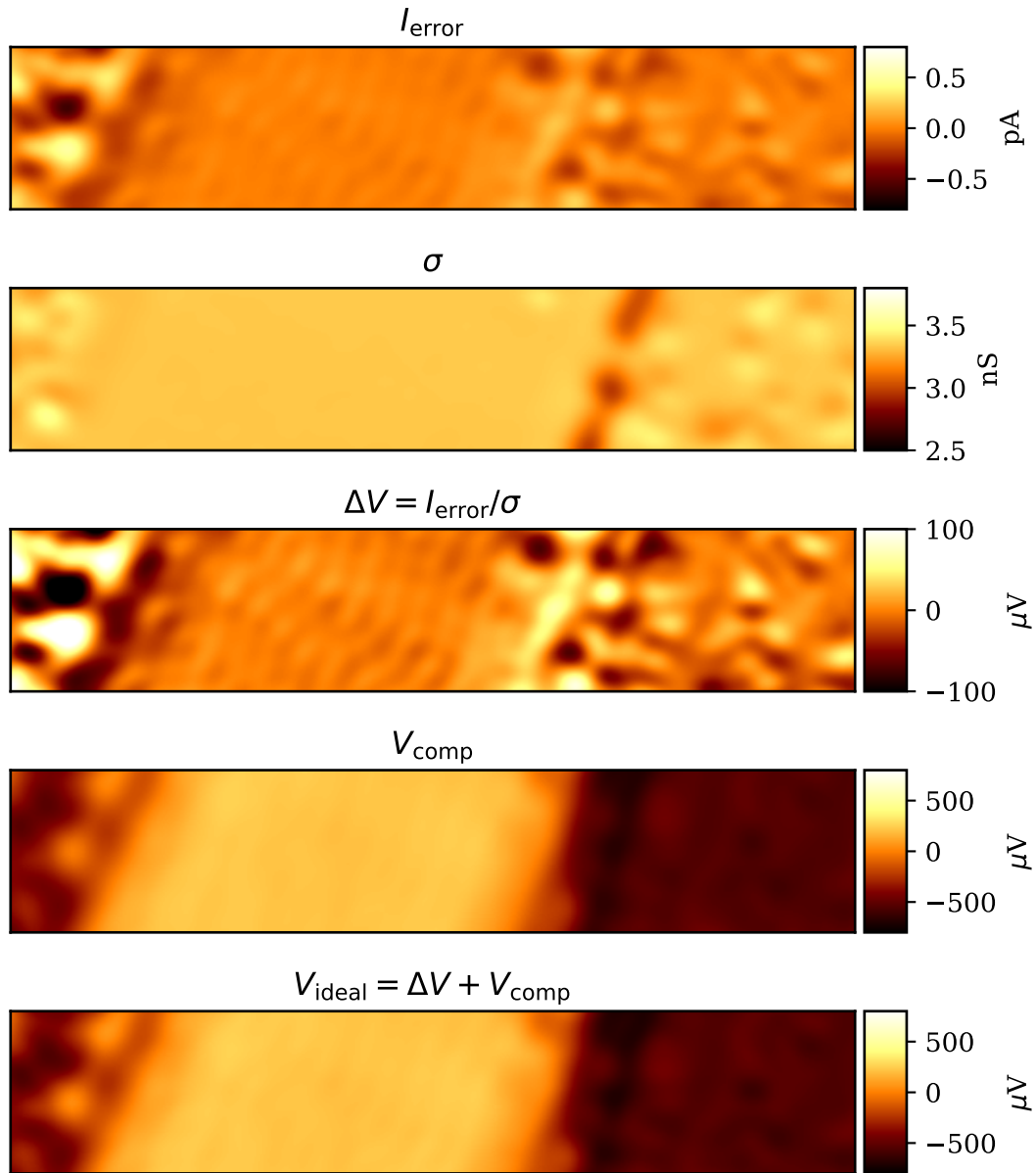


Figure B.1: Demonstration of correction for uncompensated current. Proceeding from the top, the I_{error} image is divided pointwise by the σ image, resulting in the ΔV image. This is added to the V_{comp} image, giving the final result of V_{ideal} .

Appendix C

Dependence of compensated bias on tip-sample separation

The dependence of the thermopower on the tip-sample separation has been predicted in literature [40], and with the assumption of s-states for both tip and sample has a linear character:

$$V_{\text{therm}} \propto \frac{\pi^2 k_{\text{b}}^2}{6e} T_{\text{A}} \Delta T \left(\frac{2m}{\hbar^2 \phi} \right)^{\frac{1}{2}} z, \quad (\text{C.1})$$

where ϕ is the average work function of the tunnel junction, and z is the tip-sample separation. This relationship has also been experimentally verified [88], where a sample of Ag at 330 K and a room-temperature tip (material not reported) resulted in a linear distance dependence of -1.6 mV nm^{-1} .

If an average work function of 3.3 eV is assumed, along with our average experimental values of $T_{\text{A}} = 50 \text{ K}$ and $\Delta T = 16 \text{ K}$, then the prefactor has a value of

$$\frac{\pi^2 k_{\text{b}}^2}{6e} T_{\text{A}} \Delta T \left(\frac{2m}{\hbar^2 \phi} \right)^{\frac{1}{2}} = 1.722 \times 10^{-2} \text{ mV nm}^{-1}, \quad (\text{C.2})$$

This calculated factor is much lower than the previously reported value, but this is expected, as the equilibrium temperature here (50 K versus 300 K) and ΔT are both lower. A change in tip-sample separation between the domains of 15.7 pm should then lead to a change in V_{comp} of 0.27 μV . This is a small change relative to our average signals, and so should have a negligible effect on our measured S .

To check this relationship, measurements of $\frac{\partial V_{\text{comp}}}{\partial z}$ were undertaken, for both the Fe DL and Fe ML in W(110) at $T_{\text{STM}} = 50 \text{ K}$, as reported in the Master Thesis of Hermann Osterhage [83]. This involved lateral lines of

tip-sample distance spectroscopy, with and without bias compensation, and corrections for thermal drift during the measurement.

It was found that the linear prediction for $\frac{\partial V_{\text{comp}}}{\partial z}$ did hold in general. However, much higher values for $\frac{\partial V_{\text{comp}}}{\partial z}$ than expected were found, e.g. for the DL in the range of $\approx 1 \text{ mV nm}^{-1} - 2 \text{ mV nm}^{-1}$. These would be reasonable for room temperature experiments, but not for the $T_{\text{STM}} = 50 \text{ K}$ used for the measurements.

In addition, these values were found to be highly dependent on the measured surface. Although this is to be expected due to the surface dependence of the work function, when $\phi(\vec{r})$ was measured, Equation (C.1) did not account for the change in $\frac{\partial V_{\text{comp}}}{\partial z}$. In addition, ϕ was found to depend on ΔT , with an estimated $\Delta T = 38.2 \text{ K}$ raising the work function for the Fe DL (with W tip) from 2.8 eV to 3.3 eV.

Publications

- Peter, M., Werra, J. F., Friesen, C., Achnitz, D., Busch, K., & Linden, S. (2018). *Fluorescence enhancement by a dark plasmon mode*. Applied Physics B, **124**, 1–6. <https://doi.org/10/gfxbcn>
- Friesen, C., Osterhage, H., Friedlein, J., Schlenhoff, A., Wiesendanger, R., & Krause, S. (2018). *Scanning Seebeck tunneling microscopy*. Journal of Physics D: Applied Physics, **51** (32), 324001. <https://doi.org/10.1088/1361-6463/aacfab>
- Friesen, C., Osterhage, H., Friedlein, J., Schlenhoff, A., Wiesendanger, R., & Krause, S. (2019). *Magneto-Seebeck tunneling on the atomic scale*. Science, **363** (6431), 1065–1067. <https://doi.org/10/gfxbcj>

Conferences

Invited talks

- 2019-11-07 *Magneto-Seebeck Tunneling on the Atomic Scale*
Magnetism and Magnetic Materials 2019, Las Vegas, USA.
Cody Friesen

Contributed talks

- 2016-04-06 *Magneto-Seebeck Tunneling Across a Vacuum Barrier*
SFB 668 PhD Workshop, Damp, Germany.
Cody Friesen
- 2017-03-23 *Magneto-Seebeck Tunneling Across a Vacuum Barrier*
DPG Spring Meeting, Dresden, Germany.
Cody Friesen, Hermann Osterhage, Stefan Krause
- 2018-03-13 *Magneto-Seebeck Tunneling Across a Vacuum Barrier*
DPG Spring Meeting, Berlin, Germany.
Cody Friesen, Stefan Krause
- 2018-07-18 *Magneto-Seebeck Tunneling Across a Vacuum Barrier*
International Conference on Magnetism 2018, San Francisco, USA.
Cody Friesen
- 2018-07-25 *Magneto-Seebeck Tunneling Across a Vacuum Barrier*
International Conference on Nanoscience and Technology, Brno, Czech Republic.
Cody Friesen
- 2019-06-20 *Magneto-Seebeck tunneling on the atomic scale*
Scanning Probe Spectroscopy 19, Hamburg, Germany.
Cody Friesen

Posters

- 2015-02-02 *Magneto-Seebeck Tunneling Across a Vacuum Barrier*
Spin-Caloric Transport (SPP 1538) Status Meeting, Bad Honnef, Germany.
Cody Friesen, Stefan Krause

- 2016-03-03 *Magneto-Seebeck Tunneling Across a Vacuum Barrier*
Spin-Caloric Transport (SPP 1538) Status Meeting, Bad Honnef, Germany.
Cody Friesen, Stefan Krause
- 2016-08-18 *Magneto-Seebeck Tunneling Across a Vacuum Barrier*
Spin-Caloric Transport (SPP 1538) PhD Workshop, Mainz, Germany.
Cody Friesen, Stefan Krause
- 2017-02-21 *Magneto-Seebeck Tunneling Across a Vacuum Barrier*
Spin Mechanics 4, Lake Louise, Canada.
Cody Friesen, Stefan Krause
- 2017-06-15 *Magneto-Seebeck Tunneling Across a Vacuum Barrier*
Spin Caloritronics 8, Regensburg, Germany.
Cody Friesen, Stefan Krause

Acknowledgements

I would like to take this opportunity to thank at least some of the people and organizations who made this work possible, successful, and enjoyable.

First, thank you to Stefan Krause, who proposed and led this project. The friendly and encouraging atmosphere and freedom to pursue the project goals with varied approaches made this work exciting and enjoyable, and his talent for refining and polishing scientific presentations and arguments to their essential core was invaluable for the successful publication and presentation of this work at so many conferences and venues.

Next, this project rest on the great foundation of the Scanning Probe Methods group of Prof. Dr. Roland Wiesendanger. The combination of equipment, colleagues, and commitment to science in this group is truly world-class, and I am very grateful to have had the opportunity to work here.

I would also like to acknowledge the financial support of the Deutsche Forschungsgemeinschaft, via the Schwerpunktprogramm on Spin Caloritronics, SPP 1538. Additional support came from the Sonderforschungsbereich 668: Magnetismus vom Einzelatom zur Nanostruktur.

Hermann Osterhage, who completed his Master Thesis as part of this project, was an enthusiastic and talented coworker, and was always ready to attack the next problem. This attitude was carried through many long days in the lab, and was very much appreciated.

During this project, I had the privilege to work closely with some great colleagues in Lab 018. Working with Anika Schlenhoff has led to many interesting discussions, and provided a great introduction to the world of STM. Johannes Friedlein was a tremendous help and I really enjoyed our discussions, both on experimental methodology and otherwise. Working with Ludwig Hendl for his Bachelor Thesis was a great learning experience, I think for the both of us.

The friendly and supportive atmosphere of Group R was apparent at all times, and very much appreciated. It is hard to imagine this project being successful without the many suggestions and tips from other group members, who were always willing to have a discussion when I came by. There are many names, so I will just say thank you all!

I would of course like to thank my family, who have been unfailingly supportive and encouraging through every degree and position that led to this point. Wherever I have roamed, I always knew they were cheering for me.

And finally, my wife Neele, who has always expected nothing but my best. It has been a long road to get here. Thank you.